



**HAL**  
open science

# Multi-Mode 3D Kirchhoff Migration of Receiver Functions at Continental Scale

Florian Millet

► **To cite this version:**

Florian Millet. Multi-Mode 3D Kirchhoff Migration of Receiver Functions at Continental Scale. Earth Sciences. Université de Lyon, 2019. English. NNT : 2019LYSE1201 . tel-02460732

**HAL Id: tel-02460732**

**<https://theses.hal.science/tel-02460732v1>**

Submitted on 30 Jan 2020

**HAL** is a multi-disciplinary open access archive for the deposit and dissemination of scientific research documents, whether they are published or not. The documents may come from teaching and research institutions in France or abroad, or from public or private research centers.

L'archive ouverte pluridisciplinaire **HAL**, est destinée au dépôt et à la diffusion de documents scientifiques de niveau recherche, publiés ou non, émanant des établissements d'enseignement et de recherche français ou étrangers, des laboratoires publics ou privés.



N° d'ordre NNT : 2019LYSE1201

## THÈSE DE DOCTORAT DE L'UNIVERSITÉ DE LYON

opérée au sein de  
l'Université Claude Bernard Lyon 1

École Doctorale ED52  
Physique et Astrophysique (PHAST)

Spécialité de doctorat : Sciences de la Terre  
Discipline : Sismologie

Soutenue publiquement le 21/10/2019, par :  
**Florian Millet**

---

# Migration multimode 3D de type Kirchhoff de fonctions récepteurs à l'échelle continentale

---

Devant le jury composé de :

Andréani Muriel, Maître de Conférences, Université Lyon 1

Présidente

Laigle Mireille, Chargée de Recherche CNRS, Université Nice Sophia Antipolis

Rapporteuse

Virieux Jean, Professeur Émérite, Université Grenoble-Alpes

Rapporteur

Farra Véronique, Physicien adjoint, Institut de Physique du Globe de Paris

Examinatrice

Vergne Jérôme, Physicien adjoint, Université de Strasbourg

Examineur

Bodin Thomas, Chargé de Recherche CNRS, Université de Lyon

Directeur de thèse

Rondenay Stéphane, Professeur, Université de Bergen

Co-directeur de thèse



# Acknowledgements

First and foremost, I want to thank my supervisors Stéphane Rondenay and Thomas Bodin for offering the opportunity to work with them. I met Stéphane in Les Houches in 2015 during a two-week pre-doctoral training course in geophysics, as an invited speaker in Thomas' seismology class. I was immediately absorbed by his explanations on migration, deconvolution and lithospheric structure. I had been working with Thomas on stochastic inversion of surface waves travel time measurements as part of my Master, and I have to thank him for being able to travel to California, where I could meet Cheng Cheng, who had been working on the 3D Kirchhoff migration for his PhD before me, solidifying my wish to continue on this path. Thank you for being so available, uplifting, and such (positive) critics to my work.

The PhD position was funded through a Contrat Doctoral Spécifique Normalien (CDSN) from the ENS de Lyon and Université Lyon 1. The participation to international conferences and other expenses were covered by grant 716542 from the European Union's Horizon 2020 research and innovation program (Thomas Bodin). The publication of my first paper was covered by project 231354 from the Research Council of Norway (Stéphane Rondenay). I also have to thank the DEEP Research School for the invitations to their annual General Assemblies.

I want to thank the seismology groups in Lyon and in Bergen for the interesting discussions that kept coming up at the group meetings, the interest in my own work and the field work opportunities that you offered. Special thanks have to go to the people without whom all this back and forth between Lyon and Bergen would not have been possible. Thank you Eric Benech and Claire Duchet in Lyon, Anders Kulseng and Caroline Christie in Bergen. I also want to thank both geology departments, and especially other PhD students in both Universities for the coffee breaks, outdoor trips, parties and other random events that made these three years an unforgettable experience.

I want to thank the wonderful officemates I had during my PhD, Rémi Menaut for

---

more than a year in Lyon, Felix Halpaap and Natacha Fabregas for the other half of my PhD in Bergen. I want to thank Sylvie Su for constant challenging scientific question and answer sessions per text message, and even more for the motivational messages during these past few months.

I also want to thank Ronan Duchesne for being such a lovely flatmate, as well as Rémi Menaut, Thomas Gérard and Jason Reneuve for hosting me for days and weeks on end for my shorter stays in Lyon. Thank you to all the people who kept dragging me out of the workplace into the wild city and nature. In Lyon, I especially want to thank Adrien Morison, Victor Lherm and Quentin Amet for being such amazing stress relievers. In Bergen, I want to thank Jhon Muñoz-Barrera, Felix Halpaap and Björn Nyberg, among many others, for randomly stopping at my office when it was clearly too late to continue working...

I want to thank my friends who came to visit in Norway and were always there to welcome me when I came back in France. Thank you Thomas Depoilly, Jonathan “Geo” Duchat and Guillaume Dubernard, as well as Alain Ramanamandimby, even if you could not find the time to fly that far north, for being such awesome friends, always jumping on any opportunity to gather and meet up.

Finally, I want to thank my family, my mother, father and brother, for being so supportive during this period. I has not always been easy, but coming home after long months away and seeing these three smiles is worth all the troubles in the world. And last but not least, I want to thank my grandfather Roland “Papito” Millet, for being so interested in everything I do until the last moment. I would not have been here today without you.

# Résumé

La géologie, et plus particulièrement la géophysique, repose sur l'observation, directe et indirecte, de phénomènes se produisant en surface et dans les profondeurs de la Terre. Ces observations nous permettent d'étudier et définir la structure et les dynamiques globales de la Terre. L'étude des ondes sismiques générées par les tremblements de terre les plus puissants permet, par exemple, d'entrevoir la structure des hétérogénéités dans les premières centaines de kilomètres de la Terre. En calculant précisément la façon dont les ondes incidentes se propagent dans la Terre, et en observant le temps qu'elles mettent à parvenir aux sismomètres en surface, on peut estimer la vitesse moyenne à laquelle elles se propagent en utilisant des méthodes d'inversion tomographiques. Autrement dit, ces informations nous donnent accès à la structure à grande échelle de l'intérieur de la Terre.

Dans cette thèse, nous nous intéressons au champ d'onde diffracté, qui est composé des arrivées tardives qui suivent les ondes incidentes. Par définition, les ondes diffractées contiennent de l'information liée aux hétérogénéités diffractantes, autrement dit les structures à petite échelle de la Terre, qu'elles rencontrent le long de leur trajet. De ce fait, il est possible d'étudier les variations rapides de vitesses sismiques grâce au champ d'onde diffracté, alors que ces informations seraient perdues dans les méthodes tomographiques à cause des facteurs de régularisation. Afin d'exploiter le champ d'onde diffracté, on a recours aux fonctions récepteurs (« receiver function » en anglais, RF) et à la migration sismique en profondeur de pré-empilage.

Les RF correspondent à un enregistrement du champ d'onde diffracté normalisé duquel on a retiré la signature de la source sismique. Ces RF sont obtenues par déconvolution des enregistrements sismiques bruités par l'estimation de la forme de la source sismique (« source time function » en anglais, STF, propre à chaque tremblement de terre), ce qui permet d'obtenir une estimation de la réponse impulsionnelle de la Terre (fonction de Green, qui dépend des contrastes d'impédance sismique dans le sous-sol).

L'information géologique ainsi acquise est utilisée pour produire une image de la Terre

---

en projetant l'information en profondeur dans la Terre, i.e. en migrant les RF. La migration consiste à retrouver les structures diffractantes à l'intérieur de la Terre en corrélant les pics d'énergie sur les RF le long d'isochrones, dites isochrones de migration, liées au temps de trajet des ondes diffractées. Les procédures standard de migration sismiques sont de deux types principaux. Le premier type de procédures, dont l'exemple type est la migration en point de conversion communs (« common conversion point » en anglais, CCP) est rapide mais repose sur l'hypothèse fondamentale que les discontinuités que l'on cherche à imager sont horizontales. Le second type de procédures, pour lesquelles on peut citer la « reverse time migration » (RTM), ou la « generalized radon transform » (GRT), ne font pas d'hypothèse sur la structure du sous-sol, mais demandent une forte intensité des calculs et sont de fait souvent limités à des géométries bidimensionnelles.

Au cours de ce manuscrit, nous développons une migration sismique de type Kirchhoff qui se base sur des calculs de temps de trajet sismique rapides en trois dimensions et quasiment aucune hypothèse sur la structure du milieu sous-jacent. Cet algorithme efficace nous permet de nous affranchir des traditionnelles limitations à des études 1D ou 2D. Notre principe d'imagerie prend en compte les ondes diffractées transmises et réfléchies, et se place dans la suite des travaux de Cheng et al. (2016).

Nous adaptons la migration de type Kirchhoff élastique aux géométries de diffraction inhérentes à la sismologie passive et prenons en compte les multiples de surface. Les temps de trajet de toutes les ondes diffractées sont calculées grâce à la « fast marching method » (FMM). Les amplitudes et la polarité des signaux des RF sont corrigées à l'aide du calcul de figures de diffraction 3D. Pour extraire l'information des conversions transmises et réfléchies de façon cohérente, les résultats pour chaque mode de diffraction sont sommés de plusieurs façons (linéaire, à filtre de phase, et à filtre d'amplitude non linéaire).

Afin de démontrer l'efficacité et la précision de notre méthode de migration, nous procédons à des tests synthétiques, aussi bien dans des situations réalistes qu'artificiellement compliquées, en nous servant du logiciel Raysum. Les résultats de ces tests prouvent que cette méthode de migration permet d'obtenir une image fidèle du milieu imagé quasiment sans artefacts. En intégrant les trois composantes des RF dans la migration, cette méthode de migration est capable d'exploiter l'information d'ondes arrivant avec n'importe quel angle d'incidence et n'importe quel azimut. Finalement, cette méthode de migration multi-mode 3D est appliquée à deux jeux de données de terrain issus de réseaux sismiques déployés au dessus de zones de subduction, en Grèce et en Alaska.

Notre première zone d'étude, la zone de subduction ouest hellénique, s'étend de l'extré-

---

mité ouest du Péloponnèse jusqu'en Crète. La pointe nord de la plaque Africaine y plonge sous la plaque Eurasienne à une vitesse moyenne de 4 mm par an. Il s'agit de la lithosphère océanique la plus vieille au monde à être en subduction actuellement (230 Ma). Les données utilisées pour la migration proviennent du « Multidisciplinary Experiments for Dynamic Understanding of Subduction under the Aegean Sea » (MEDUSA), et ont précédemment fait l'objet d'une migration 2D de type GRT. Les images obtenues avec notre méthode 3D de type Kirchhoff sont similaires à celles produites par la migration GRT. Le Moho continental, l'interface de subduction et le Moho subduit sont visibles aux mêmes profondeurs dans les deux images, et l'épaisseur de la couche à faible vitesse au sommet du panneau plongeant est cohérente avec les résultats publiés précédemment.

La seconde zone étudiée, le sud de l'Alaska, est située à la convergence des plaques Pacifique et Nord Américaine. La subduction de la plaque Pacifique le long de la chaîne des Aléoutiennes génère une intense activité volcanique, qui s'arrête abruptement au niveau du Denali volcanic gap (DVG), qui lie la subduction à l'ouest au complexe d'accrétion qui domine le régime tectonique à l'est. Cette absence de volcanisme a été reliée à la subduction en profondeur sous le continent Américain du plateau du Yakutat. Cependant, les conditions dans lesquelles le panneau plongeant transitionne de la plaque Pacifique vers le plateau du Yakutat n'ont pas encore été complètement éclaircies. Afin d'étudier cette transition, les données d'un réseau sismique composite qui regroupe trois déploiements temporaires entre 2000 et 2018 sont utilisées pour imager la région (codes réseau XE, YV et ZE). Le panneau plongeant est imagé par deux méthodes complémentaires, une migration GRT 2D et une migration Kirchhoff 3D. Les résultats de cette étude indiquent que la transition entre les deux lithosphères est marquée par un changement d'épaisseur crustale à une profondeur de 60 à 80 km. En outre, elle aurait lieu plus au Nord que ce qui avait été admis précédemment. La plaque Pacifique est observée jusqu'à une profondeur de 170 km sous le golfe de Cook. L'image issue de la migration Kirchhoff montre aussi une différence de pente entre l'enveloppe de sismicité et les interfaces de subduction, effet qui est lié à l'éclogitisation progressive de la croûte. Ce phénomène n'est pas observé sous le DVG, où le Yakutat plonge sous l'Alaska.

La thèse est construite de la manière suivante. Le chapitre 1 s'ouvre sur une approche historique de l'imagerie de la Terre et présente rapidement les principaux développements méthodologiques et découvertes scientifiques des chapitres suivants. Le chapitre 2 est constitué d'un papier publié dans le *Journal of Geophysical Research* qui présente les développements méthodologiques sur la migration Kirchhoff en détail ainsi que l'appli-



---

cation de la méthode de migration à la zone de subduction ouest hellénique. Le chapitre 3 présente le traitement des données sismiques utilisées pour la migration en détail ainsi que l'application de la méthode de migration à la zone de subduction en Alaska. Le chapitre 4 résume le travail accompli pendant la thèse et offre quelques pistes de recherche pour le développement futur de cette méthode de migration.

# Abstract

In geology, and in particular in geophysics, direct and indirect observations of processes occurring both at the surface of the Earth and at depth are used to understand the structure and dynamics of the Earth. For instance, seismic waves generated by large earthquakes can be used to study the structure of heterogeneities in the first few hundred kilometers inside the Earth. By computing the propagation path of the incident seismic waves and observing their travel times, one can estimate the waves' mean propagation velocities along their paths with tomographic methods, i.e. the large scale seismic structure of the Earth.

In this work, we use the scattered wavefield, which corresponds to energy arriving after the incident wavefield, to image the Earth. By nature, the scattered waves are linked to the scattering heterogeneities encountered along their propagation path, i.e. the fine scale structure of the Earth. Hence, the scattered wavefield has the ability to highlight structures where rapid velocity variations would otherwise be smoothed out by tomographic regularization, such as the structure of subducting slabs. To extract the information from the scattered wavefield, we resort to receiver function (RF) analysis and pre-stack depth migration.

The RF is a normalized record of the scattered wavefield from which the source signature has been eliminated. The RF is obtained through deconvolution of the estimated source time function (STF, characteristic of naturally occurring earthquake) from the noisy recorded wavefield to get an estimation of the impulsive response of the Earth (Green function, characteristic of the seismic contrasts at interfaces and heterogeneities in the Earth).

This information in the seismic signal is exploited to image the Earth by back-projecting it at depth, i.e. by migrating the RF. Migration takes the data recorded at the surface and uses it to find the scattering structures in the subsurface by correlating energy peaks on the RF along migration isochrons. Standard migration procedures either

---

rely on the assumption that underlying discontinuities are horizontal, such as in Common Conversion Point stacking (CCP), or are computationally expensive and usually limited to 2D geometries, such as in Reverse Time Migration (RTM) or Generalized Radon Transform (GRT).

Here, we develop a Kirchhoff-type teleseismic imaging method that uses fast 3D travel-time calculations with minimal assumptions about the underlying structure. This provides high computational efficiency without limiting the problem to 1D or 2D geometries. In our method, we apply elastic Kirchhoff migration to transmitted and reflected teleseismic waves (i.e., RF). The approach expands on the work of Cheng et al. (2016).

The 3D elastic Kirchhoff migration is adapted to the passive seismology scattering geometry and to account for free surface multiples. We use an Eikonal solver based on the fast marching method (FMM) to compute travel times for all scattered phases. 3D scattering patterns are computed to correct the amplitudes and polarities of the three component input signals. We consider three different stacking methods (linear, phase weighted and 2<sup>nd</sup> root) to enhance the structures that are most coherent across scattering modes.

To showcase the efficiency and accuracy of our migration procedure, we test it by conducting a series of synthetic tests in both artificially challenging and realistic scenarios. Results from synthetic tests show that our imaging principle can recover scattering structures accurately with minimal artifacts. We show that integrating the three components of the RF into the imaging principle allows to coherently retrieve the scattering potential for arbitrarily dipping discontinuities from all back-azimuths, and are able to retrieve a typical 2.5D subduction zone structure. We apply this novel 3D multi-mode Kirchhoff migration method to two different subduction zones, in Western Greece and Southern Alaska.

The first study area, the Western Hellenic subduction zone, surrounds mainland Greece and the Peloponnese region from the west before transitioning into the Southern Hellenic subduction zone offshore Crete. The oceanic tip of the African plate subducts under the Eurasian plate at an average rate of 4mm/yr and is the oldest oceanic lithosphere still subducting today (230 Ma). The data used come from the Multidisciplinary Experiments for Dynamic Understanding of Subduction under the Aegean Sea (MEDUSA) experiment in the Hellenic subduction zone, and have been used previously for 2D GRT imaging. Our images are similar to those obtained by 2D GRT migration. The overriding Moho, the slab top and the subducted Moho are visible at the same depth as the GRT images

---

and the thickness of the subducted low-velocity layer is in agreement with previous results.

The second study area, Southern Alaska, is located at the northern interface between the Pacific plate and the North American continent. The subduction of the Pacific plate generates arc volcanoes along the whole Aleutian trench, but volcanic activity suddenly stops at the Denali Volcanic Gap, which links the subduction in the west to the collision and accretionary system to the east. The volcanic gap has been linked to the underthrusting of the Yakutat terrane. However, the transition from the Pacific slab to the Yakutat at depth is not fully understood. To investigate this issue, we use a new composite seismic dataset, combining the data from three temporary arrays deployed in the region from 2000 to 2018 (network codes XE, YV and ZE). We apply two complementary teleseismic migration methods, 2D GRT and 3D Kirchhoff migration, to obtain 3D scattering images of the region. Our results show that the transition from the Pacific crust to the Yakutat terrane, which is marked by an abrupt change in crustal thickness at depths of 60 to 80 km in both methods, happens further north than previously thought. The subducted Pacific plate is observed down to 170 km to the northwest of Cook inlet. The Kirchhoff migration also images a departure at depth between the imaged subducting interfaces and the seismicity envelope in this region, which is linked to the progressive eclogitization of the crust. There is no clear evidence for this phenomenon under the Denali Volcanic Gap where the Yakutat terrane subducts under Alaska.

The thesis is organized as follows. Chapter 1 gives an historical overview of the study of the Earth using geophysical evidence and briefly summarizes the findings described in the following chapters. Chapter 2 is a paper published in *Journal of Geophysical Research* that presents the method in greater detail as well as the application to the hellenic subduction zone. Chapter 3 presents the data processing in greater detail as well as the application to the southern Alaska subduction zone. Chapter 4 summarizes the work undertaken during this thesis and offers some outlook for further development of the migration method.



# Contents

<b>1</b>	<b>Introduction</b>	<b>17</b>
1	The Earth: What are we looking at? . . . . .	17
1.1	Structure of the Earth . . . . .	17
1.1.1	First scientific rationales about the interior of the Earth . . . . .	18
1.1.2	Probing the Earth with physical measurements . . . . .	18
1.1.3	The seismic structure of the Earth . . . . .	19
1.2	The surface of the Earth: the tectonic plates and their boundaries . . . . .	22
1.2.1	From the fixist Earth to plate tectonics . . . . .	22
1.2.2	Interactions at the plate boundaries . . . . .	24
1.3	Subduction zones . . . . .	26
2	Which tools do we have to image the Earth? . . . . .	28
2.1	Geophysical exploration . . . . .	28
2.2	Seismic imaging . . . . .	29
2.3	The incident wavefield . . . . .	32
2.4	The scattered wavefield . . . . .	34
2.4.1	Active seismic experiments . . . . .	35
2.4.2	Passive seismology . . . . .	36
3	What methods are we using to image the Earth? . . . . .	39
3.1	Receiver Functions . . . . .	39
3.2	Classical migration in passive seismology . . . . .	44
3.2.1	1D stacking methods . . . . .	44
3.2.2	2D and 3D migration techniques . . . . .	46
3.3	Towards efficient fully 3D migration . . . . .	49
4	What did we find out about the Earth? . . . . .	52
4.1	Methodological developments . . . . .	52
4.1.1	Data processing . . . . .	52
4.1.2	Migration and imaging . . . . .	56

4.2	Application of the migration method to the Western Hellenic subduction zone . . . . .	58
4.3	Application of the migration method to the Southern Alaska subduction zone . . . . .	60
<b>Bibliography</b>		<b>63</b>
<b>2</b>	<b>Multi-Mode 3D Kirchhoff Migration of Receiver Functions at Continental Scale</b>	<b>75</b>
1	Introduction . . . . .	76
2	Methodology . . . . .	80
2.1	Three component Receiver Functions . . . . .	80
2.2	Kirchhoff prestack depth migration . . . . .	82
2.3	Accounting for scattering theory . . . . .	83
2.4	Three-dimensional scattering patterns . . . . .	84
2.5	Forward scattered waves and free surface back-scattered multiples .	87
2.6	Integration of free surface multiples . . . . .	88
2.7	Image Stacking Techniques . . . . .	92
2.7.1	Linear stacking . . . . .	92
2.7.2	Phase-Weighted stacking . . . . .	92
2.7.3	2 <sup>nd</sup> root stacking . . . . .	93
3	Synthetic tests . . . . .	95
3.1	Model and setup . . . . .	95
3.1.1	Synthetic models . . . . .	95
3.1.2	Synthetic setup . . . . .	97
3.1.3	Synthetic waveforms . . . . .	97
3.1.4	Overall computational cost . . . . .	98
3.2	Scattering patterns and three-component migration . . . . .	98
3.3	Multi-mode migration . . . . .	102
3.4	Stacking methods . . . . .	104
3.5	2.5D subduction zone . . . . .	105
4	Application to field data and implications . . . . .	108
4.1	Hellenic field data . . . . .	108
4.2	Resolution test . . . . .	111
4.3	Field data migrated sections . . . . .	112
5	Discussion: Advantages and drawbacks of the method . . . . .	114

5.1	Scattering potential vs elastic perturbations . . . . .	114
5.2	3D seismic imaging . . . . .	115
5.3	Scattering patterns . . . . .	116
5.4	Multi-mode and stacking schemes . . . . .	117
5.5	Towards fully 3D settings . . . . .	118
6	Conclusions . . . . .	119
<b>Bibliography</b>		<b>127</b>
<b>3 A new look at the Southern Alaska Subduction Zone using 2D and 3D Migration of Receiver Function</b>		<b>133</b>
1	Introduction . . . . .	134
1.1	Geological setting . . . . .	135
1.2	Seismic imaging in the region . . . . .	137
2	Data and processing . . . . .	138
2.1	Composite array for 2D and 3D imaging . . . . .	140
2.2	Pre-processing of the data . . . . .	141
2.3	Deconvolution and receiver functions . . . . .	142
2.4	Visual inspection of the data . . . . .	144
3	Methods . . . . .	145
3.1	2D GRT migration . . . . .	145
3.2	3D Kirchhoff migration . . . . .	146
3.3	Multi-mode stacking . . . . .	148
3.4	Additional data and velocity models . . . . .	148
4	Results . . . . .	149
4.1	GRT images . . . . .	149
4.2	Kirchhoff images . . . . .	151
5	Discussion . . . . .	152
5.1	Resolution, penetration and observation limits . . . . .	152
5.2	Western limit of the Yakutat Terrane . . . . .	153
5.3	Intra-slab seismicity . . . . .	154
6	Conclusion . . . . .	155
<b>Bibliography</b>		<b>161</b>
<b>4 Concluding remarks and scientific outlook</b>		<b>165</b>
1	Conclusions . . . . .	165



## CONTENTS

---

1.1	Writing the migration algorithm . . . . .	165
1.2	Processing the seismic data . . . . .	165
1.3	First geological applications . . . . .	166
1.4	Side projects . . . . .	166
1.5	Conferences, abstracts and publications . . . . .	167
2	Scientific outlooks . . . . .	167
2.1	New geological objectives . . . . .	167
2.2	Optimizing the numerical algorithm . . . . .	168
2.3	Adapting the code for new data types . . . . .	168

<b>Bibliography</b>	<b>171</b>
---------------------	------------

# Introduction

## 1 The Earth: What are we looking at?

### 1.1 Structure of the Earth

The Earth is round and it orbits the Sun. Although its rough shape and size have been known since at least the ancient Greeks, those findings were later dismissed in the western world before being rediscovered during the past few centuries (Plato, nd). Our planet displays many landscapes that we like to look at, hike through and protect. In its early days, geology started as the field of science that is trying to understand how these landscapes form, evolve and interact. But the Earth also has regions that are subject to various hazards such as earthquakes, volcanoes and tsunamis, and soon geology became a composite science addressing a diverse range of questions such as how the Earth formed and evolved, how these phenomena are generated, and how rocks, oceans and the atmosphere interact among many others.

In geosciences, and in particular in geophysics, direct and indirect observations of processes occurring both at the surface of the Earth and at depth are used to understand its structure and dynamics. A specificity of the geosciences is that they study structures and processes at a wide range of scales both in time and space. If geology started as a very descriptive science, modern geosciences are by essence multidisciplinary, as geoscientists study the Earth with all possible approaches, from field rock sampling to computational geodynamics and isotopic geochemistry.

In this work in particular, we use seismic waves generated by large earthquakes to study the structure of heterogeneities in the first few hundred kilometers inside the Earth (Bostock, 2015). In this first section we will start by diving into the Earth to see what it is made of at the global scale. Then we will explore the surface of the Earth and explain

how we intend to link what we learned from the deeper parts of the Earth to what we see at the surface.

### 1.1.1 First scientific rationales about the interior of the Earth

Today we know that the Earth is an oblate spheroid and that it describes an ellipsoidal trajectory in space with the Sun as one of the foci, but it has not always been this way (Kepler, 1609; Newton, 1687). First, until about 3000 years ago in Europe, people thought that the Earth was flat, similar to the ground that we walk on, and probably extended infinitely, as no one ever saw the end of it. Later, during the 6<sup>th</sup> century BC, the idea of an infinite Earth started bothering the ancient Greeks, and they tried to explain how the oceans and cosmos was wrapped around a finite flat Earth (Aetius, nd). In the 4<sup>th</sup> century BC, Plato proved that the Earth was round, or more precisely spherical. This made the early geologists wonder what was inside our planet (Aristotle, nd).

Early ideas about the internal composition of the Earth revolve around empty cavities that are linked together and the wind blowing through these cavities was generating the earthquakes and volcanoes. During 2000 years, this hypothesis and other “empty” Earth models, such as the one from Athanasius Kircher, continue to be the predominant view of the interior of the Earth (Kircher, 1664). In the 18<sup>th</sup> century, Georges-Louis Leclerc, otherwise known as Comte de Buffon, realized that there could not be empty space inside the Earth. The material that this “full” Earth was made of was probably hot, therefore mostly made of molten material, similar to what we would see erupt from time to time in volcanoes (Buffon, 1749). Finally, in the 18<sup>th</sup> and 19<sup>th</sup> centuries, geologists started to develop physical methods to test their hypotheses about the composition of the Earth.

### 1.1.2 Probing the Earth with physical measurements

Physical exploration of the inside of the Earth starts during this period with the formal measurements of the gravity field (figure 1). During his expedition near the Equator to precisely measure the length of a meridian, Bouguer noted that massive mountains should have an observable effect on the gravity field of the Earth given their large mass (Bouguer, 1749). However, the effect of the equatorian cordillera on the gravity field was smaller than expected given its size. He did not have a conclusive explanation for that phenomenon, arguing that experiments on other large mountains were required. One century later, two main models were competing to explain these observations.

First, George Biddell Airy said that the gravitational disturbance is mostly compensated at depth by a crustal root with similar density (Heiskanen, 1924). Second, John

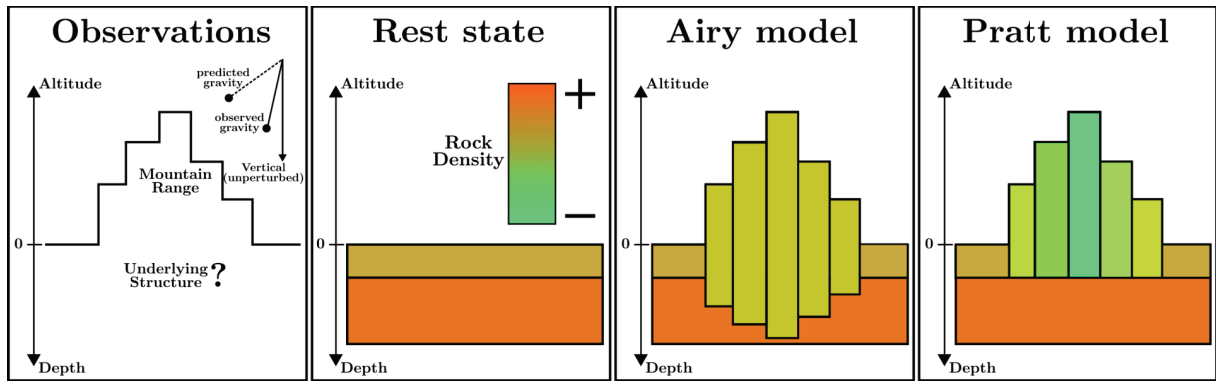


**Figure 1** – Isostatic models. First panel presents the observations described in the text. Second panel presents the rest state, i.e. without mountain and an unperturbed gravity field. Third and fourth panel present the models developed by Airy (constant density) and Pratt (constant root depth) to explain the geodetic observations.

Henry Pratt said that the disturbance is compensated very shallowly because the mountains are made from less dense material than the rest of the Earth (Pratt, 1855). Today, we use the model described by Airy to explain the topography of mountain ranges, and the model described by Pratt to explain the depth of the ocean floor and its topography.

Then, scientists went deeper into the Earth using seismology. This new geophysical tool associates the physical principle of the wave equation, formalized by D’Alembert to the study of the Earth’s interior (D’Alembert, 1747). By using ground motion recordings at the surface of the Earth, we can record the arrival of compressional (P) and shear (S) waves from naturally occurring earthquakes and artificially generated signals such as quarry blasts, controlled vibrations or even nuclear detonations (Poisson, 1829).

Exploration of the Earth using naturally occurring earthquakes started in 1889 when observation from an earthquake in Tokyo at a station in Potsdam allowed to perform the first estimation of average P-wave velocity in the Earth at around 7km/s (von Rebeur-Paschwitz, 1889). Since then the instrumentation has been, and still is, increasing both in quality and quantity and we have been able to better infer spatial variations in seismic wave velocities inside the Earth. These global observations allowed to probe the Earth deeper and deeper and the first-order seismic structure of the Earth down to its center was established within 50 years of the first quantitative earthquake recording (von Rebeur-Paschwitz, 1889; Lehmann, 1936).

### 1.1.3 The seismic structure of the Earth

To first order, the Earth is comprised of several concentric layers (Dziewonski and Anderson, 1981). The first layer is the crust, and is separated into continental and oceanic

domains. Then comes the mantle. The limit between these two layers is called the Moho and has been discovered in 1909 by Andrija Mohorovičić ([Mohorovičić, 1909](#)). It lies at 5 to 10 km depth under the oceans and 30 to 70 km depth under the continents. The mantle is not entirely uniform. There is a region between 410 and 670 km containing three jumps in seismic velocities ([Anderson, 1967](#)). These fueled the debate as to whether the mantle was acting as one block or as two separate entities. Today we believe that the upper and lower mantle act mainly as one dynamic unit but that these transitions generate some smaller-scale separated dynamics.

At the center of the Earth is the core. The limit between the mantle and the core is called the core-mantle boundary (CMB) and has been proposed by Emil Wiechert in 1897 and formally discovered by Richard Oldham in 1906 ([Wiechert, 1897](#); [Oldham, 1906](#)). In 1912, Beno Gutenberg refines the depth of this boundary to its current estimate ([Gutenberg, 1912](#)). It lies at 2900 km depth, almost uniformly in all regions of the globe. Finally, within the core there is a liquid outer core and a solid inner core. The limit is called the inner core boundary (ICB) and was discovered in 1936 by Inge Lehmann, as the core exhibits an absence of shear wave propagation in the outer part, which is characteristic of a fluid layer ([Lehmann, 1936](#)). This limit lies at 5200 km depth, and the inner core extends all the way to the center of the Earth at 6370 km depth. The outer core is linked to the Earth's magnetic field ([Gilbert, 1600](#)). Even though the magnetic field has been used for millennia for navigation with compasses, the first theory about its origin dates back only to 1600, and a convincing explanation only emerged in the past century ([Gilbert, 1600](#); [Elsasser, 1956](#)). Its origin and behaviour are still debated today, but scientists believe that it is linked to coherent rotation of magnetic fluid, which confirms the seismological observations of a liquid core ([Jeffreys, 1926](#)).

Thanks to the information provided by seismic records, a number of 1D Earth reference models have been proposed (figure 2). One of the first global models obtained from both surface waves and body waves measurements was the preliminary reference Earth model, or PREM ([Dziewonski and Anderson, 1981](#)). It was computed using normal mode measurements, i.e. the measure of how the Earth vibrates as a whole when excited by very large earthquakes, as well as direct P and S waves travel time measurements. We now have several other 1D Earth models, each one built around different datasets (e.g., IASP91 ([Kennett and Engdahl, 1991](#)), AK135 ([Kennett et al., 1995](#))). They represent radial averages of physical properties for any depth inside the Earth. In the case of our seismological models, we can obtain the values of the P and S wave velocities, radial anisotropy, attenuation, as well as the density of the medium. These simple, concentric models serve as a reference for further 2D and 3D imaging methods such as the one

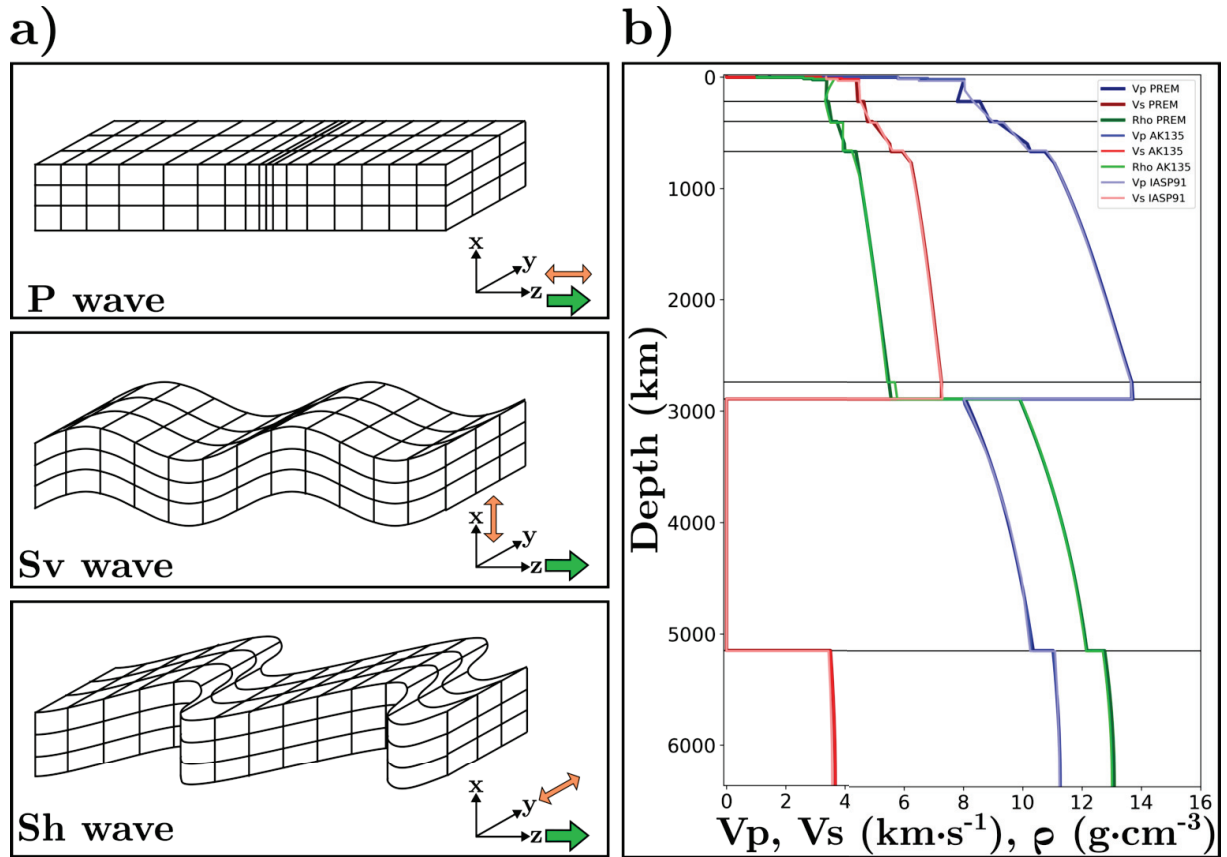


**Figure 2** – (a) Geometric representation of P and S waves. Green arrow represents direction of propagation (always Z) and orange double arrow represents direction of oscillation (Z for P wave, X for Sv wave, Y for Sh wave). (b) Reference 1D Earth models elastic parameters.

developed during this thesis (see section 3 and chapter 2).

In order to decipher the thermo-chemical structure of the Earth, seismic velocities computed for the Earth are compared with laboratory experiments to find which materials and temperatures are the most probable candidates. At first, pure elements and minerals were tested for density and seismic velocities under broad ranges of pressure and temperature conditions. This is how we found that the core is mainly made of iron and the mantle made of silicates (Anderson et al., 1971; Badro et al., 2007). To further discriminate between the candidate rocks, which represent different chemical compositions for the Earth, we need to be able to replicate the jumps in elastic properties from the seismological models. This is how we constrained the silicate composition of the mantle (Duffy and Anderson, 1989; Xu et al., 2008). Finally, we can add constraints from other fields such as gravimetry and cosmochemistry to refine our estimates. This field is still very active today as the sensitivity from the different methods increases and the estimates become more precise.

Following the birth and refinement of average 1D seismological and petrological mod-

els, scientists wanted to go further and understand the structure and evolution of a 3D dynamic Earth. Therefore, the next step is to describe the Earth using 3D models. In such models, the specific aspects of different regions of the Earth can be explored independently, or studied together to investigate the structure and evolution of our planet at the global scale. These 3D studies and models can be done on a global scale or a regional scale and target a large variety of different phenomena. This thesis deals mainly with structures in the upper few hundred kilometers of the Earth, at the interface between the mantle and the crust. We are interested in how the mantle and the crust interact with each other when two tectonic plates collide. The lateral extent of the regions that we are interested in is on the order of a few hundred kilometers, placing it at the intermediate “continental” scale.

## **1.2 The surface of the Earth: the tectonic plates and their boundaries**

### **1.2.1 From the fixist Earth to plate tectonics**

Going back briefly to the surface of the Earth, we will now look at how it moves, and more particularly at how tectonic plates interact with each other. The idea of a laterally evolving Earth surface made of moving elements, where the current proportions and distribution of  $\sim 70\%$  oceans split into 3 main bodies of water and  $\sim 30\%$  land split into seven main continents changes through geological ages, is quite recent in scientific history (Suess, 1885). First, people believed in the hypothesis of the fixist Earth, which states that the Earth has always existed in its current form. This fixist point of view is a broader mode of thinking than just geology, and also applied to the nature of animal species for example, as the dominant hypothesis for thousands of years.

When the Earth was proven to be round for the second time in western history (see section 1.1), the idea of the collapsing Earth took its place (Suess, 1885). This theory links the thermal state of the Earth, which at that time is believed to be made of extremely hot and dilated material, to that of a cooling solid body. By virtue of cooling the Earth, therefore reducing its volume while keeping the same surface area, the cooling Earth theory explains the creation of the mountains by way of preferential collapsing in some parts of the globe. This theory also aimed at explaining other geophysical phenomena, such as earthquakes, but failed at capturing the nature of their distribution on the globe (Bonnier, 1900).

In the 1920’s, the continental drift theory described by Alfred Wegener challenges

these views (Wegener, 1929). Wegener uses geometrical and paleontological clues, most famously the intricate puzzle pieces that some continental shelves form, common glacial clues on several southern continents as well as shared fossil record across oceans, to prove that the continents must have been in a different configuration in the past. However, his theory was not complete as he lacked a proper driving force to explain those movements.

In the 1950's and 60's, Harry Hess and others found new observations and a driving force that confirm the lateral motion of the ocean floor (Hess, 1962). After the discovery of the high topography and seismic activity of the central part of the seafloor, the mid-oceanic ridge, they observed magnetic bands on the ocean floor. Those magnetic bands are symmetric in polarity and age on either side of the ridge, with younger ages closer to the ridge, which indicates the ocean floor is moving away from the ridge. Hess explains that this lateral motion is supported by global convection in the Earth's mantle. Based on these observations, Jason Morgan, Xavier Le Pichon, and Dan McKenzie independently proposed quantitative surface motion models that separate the Earth in 6 to 12 major plates between 1967 and 1968 (McKenzie and Parker, 1967; Morgan, 1968; Le Pichon, 1968). This was the birth of the plate tectonics theory.

The structural definition of a plate has emerged in the 1960's with the birth of the plate tectonic theory and precise seismological observations (McKenzie and Parker, 1967). This theory states that there are a few rigid bodies that travel across the surface of the Earth and that are in contact with one another at moving boundaries where matter is extracted from or injected into the mantle. These boundaries accumulate and relieve most of the stresses due to the tectonic activity of the Earth, and are strongly underlined by the distribution of earthquake hypocenters, as can be seen on figure 3.

Seismological observations show that the plates themselves are dynamically decoupled at depth from the unperturbed upper mantle by a low velocity zone (LVZ) that usually lies at up to a few tens of kilometers depth under the oceans and up to a few hundred kilometers depth under the continents (Chapman and Pollack, 1977). The tectonic plate is seismologically defined as everything that is above this discontinuity, even if this seismological signal is not clear in every region of the Earth. It is comprised of a piece of crust, continental or oceanic, and lithospheric mantle. The tectonic plates, especially the continental ones, usually have a complex and rich history. Some pieces of continental crust have been dated at up to 4 billion years, which is barely 500 millions years after the formation of the Earth (Bowring et al., 1989).



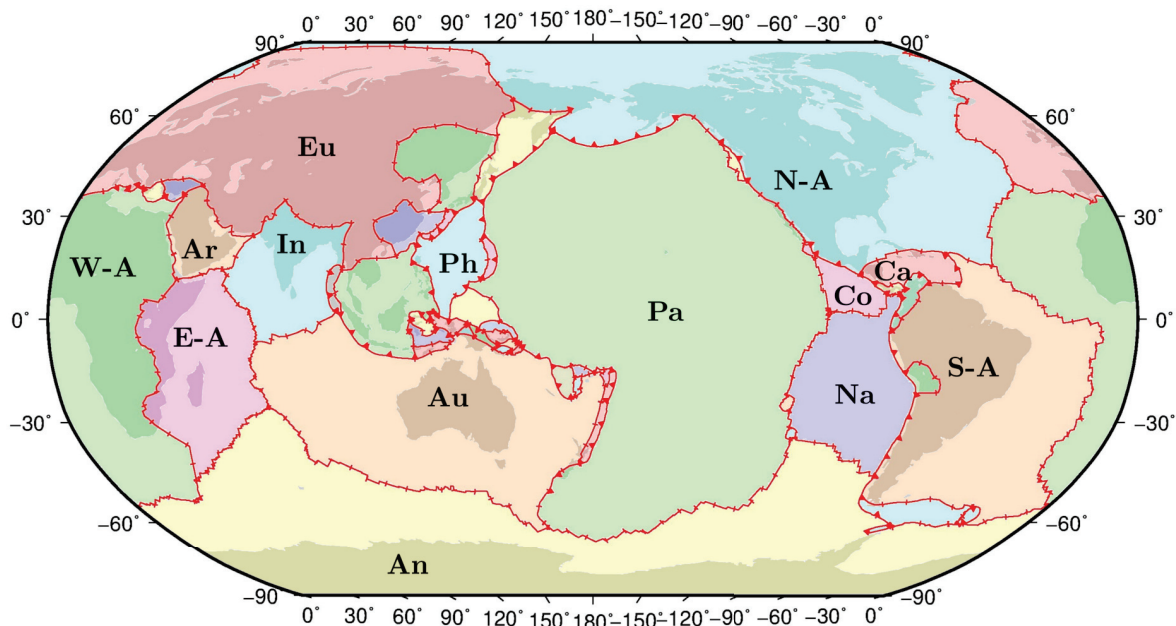


**Figure 3** – Map of tectonic plates today. Triangles represent convergent limits, dashes represent divergent limits. W-A=west Africa, E-A=east Africa, N-A=North America, S-A=South America, An=Antarctica, Ar=Arabia, Au=Australia, Ca=Carribbean, Co=Cocos, Eu=Eurasia, In=India, Na=Nazca, Pa=Pacific, Ph=Philipine. Image reproduced from [tectonicwaters.wordpress.com](https://tectonicwaters.wordpress.com) using data from Peter Bird (Sornette and Pisarenko, 2003).

### 1.2.2 Interactions at the plate boundaries

The different tectonic plates interact with each other at their common boundaries. These boundaries can be divergent, i.e. the plates move away from another, convergent, i.e. the plates move closer to another, or strike-slip, i.e. the plates glide by another. These structures highlight the limits between different regions of the Earth's surface, that have different structural properties, and present some of the largest natural risks. The most prominent and direct risk is earthquakes. They happen when stress, that is slowly accumulated for long periods of time due to friction between plates that move relative to each other, is suddenly released between them and they slip along their interface (Savage and Prescott, 1978). This releases seismic energy that can damage buildings in the near field and propagate strong waves in the far field. We will talk about them in abundance later.

Another risk associated with plate boundaries is the generation of tsunamis. Tsunamis are large oceanic waves that are not generated by tidal motion, usually of very long wavelength, that propagate across the oceans and hit the land where they can reach high amplitudes due to the shallow sea level (Satake, 2015). They can happen after strong offshore megathrust earthquakes that shake the ocean floor vertically, thus generating large waves above their hypocenter.

Finally, plate boundaries are associated with volcanoes. The best example is the ring of fire in the Pacific ocean, but one can also cite the Krakatoa volcano in Indonesia, mount Vesuvio or Etna Italy and Tristan da Cunha or the Canary islands in the middle of the Atlantic ocean (Marsh, 2015).

Plate boundaries mainly take the shape of line segments when viewed from the top. Some of those segments have a certain continuity along strike, such as the plate boundaries around the Pacific ocean. As it is difficult to represent complex structures in 3D, we usually study their structure by looking at transects oriented orthogonally to their strike (Rondenay, 2009). These 2D transects reveal a limited number typical 2D structures that can be observed across many different regions. We will describe them in the next paragraph. When continuity is less obvious in map view, such as in the Himalayan mountain ranges for example, this usually translates into more complex 3D structures underneath (Priestley et al., 2008).

There are three main types of 2D structures at plate boundaries (figure 4). They represent steady-state behaviours of plate boundaries. The first ones are the mid-oceanic ridges that we described earlier (Dunn, 2015). Those are regions, hidden under the oceans, where extension between two plates makes mantle material rise and partially melt to create new oceanic crust. The second ones are transform faults (Wessel and Müller, 2015). Those are regions where two plates are in contact with each other but no crustal material is created from nor injected into the mantle. Most of them are also on the ocean floor, and connect segments of the spreading ridge. The third ones are subduction zones (Wada and King, 2015). Those are regions where a slightly denser plate, usually of oceanic nature, is forced to enter the Earth under a slightly more buoyant plate, usually of continental nature. Hence in this case crustal material is injected into the mantle. We will describe this in greater detail later. These structures are mostly 2D and have symmetries along the direction of movement between the plates.

In addition to these mainly 2D structures, there a few fully 3D structures (figure 4). They correspond to very particular environments and/or initiation and termination of the processes cited above. The two most prominent examples are rifting zones, where mid-oceanic ridges are born, and suture zones, where subduction terminates (Searle, 2015; Buck, 2015). A third type of 3D structure occurs in regions where the tectonic setting goes from one type of boundary to another. For example when a plate boundary goes from a subduction dynamic to a stage of suture/collision, or from frontal subduction to strike-slip motion (Pearce et al., 2012). This is what we will study in chapter 2. Finally, introducing a large scale heterogeneity in what is mostly a 2D setting, such as a subduction zone, can generate strong 3D behaviour. This is what we will study in chapter 3.

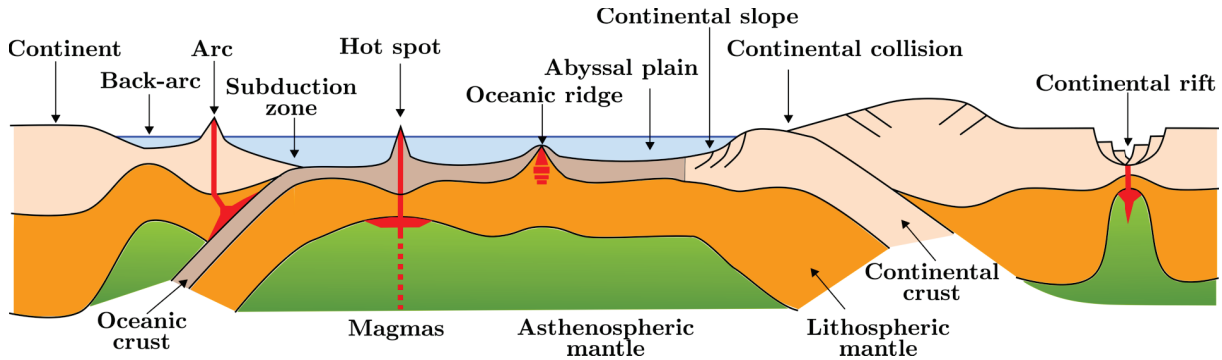


**Figure 4** – Simplified 2D view through typical plate boundary structures, not to scale. Transform faults are not shown here as they are mostly parallel to this kind of slice, visible only in map view.

### 1.3 Subduction zones

A subduction zone is a complex open system. It is linked to the recycling of crustal material in the upper and lower parts of the mantle and to the cycle of a large number of elements and molecules, including  $\text{CO}_2$  and water (Dasgupta and Hirschmann, 2010). Subduction happens when a plate is pushed under another one into the mantle, potentially all the way down to the core mantle boundary. Its dynamics are linked to differences in mineralogy and temperature between the plates, which in turn create large density variations (Jamtveit et al., 1990). These density variations determine which plate sinks and which stays afloat.

In the most general sense, subduction can happen between any two plates but almost always implies at least one oceanic plate. The chemical composition of oceanic plates is slightly different from continental plates (Mooney, 2015). Oceanic plates contain less silica overall, which makes them denser and less rigid. This means that when a continental and an oceanic plate collide, the continental one has a higher buoyancy and tends to override the oceanic one rather than deform to accommodate the stress. This pushes the oceanic plate into the mantle, increasing the lithostatic pressure that it is subject to (figure 5).

Oceanic plates are normally more buoyant than the mantle, which should prevent them to sink even if they are trapped under a continent (Wada and King, 2015). However, the increase in pressure, as well as temperature to a smaller extent, triggers a series of mineralogic reactions in the oceanic crust (Doin and Henry, 2001). These reactions, culminating with eclogitization, increase the density of the oceanic plate to above that of the mantle, therefore making the oceanic plate sink into the mantle.

The fate of the plate that subducts is further mineralogic transformation, bending, and exchange of material with the surrounding mantle (Fukao and Obayashi, 2015). During the subduction process, the minerals react with each other to create new ones in the solid

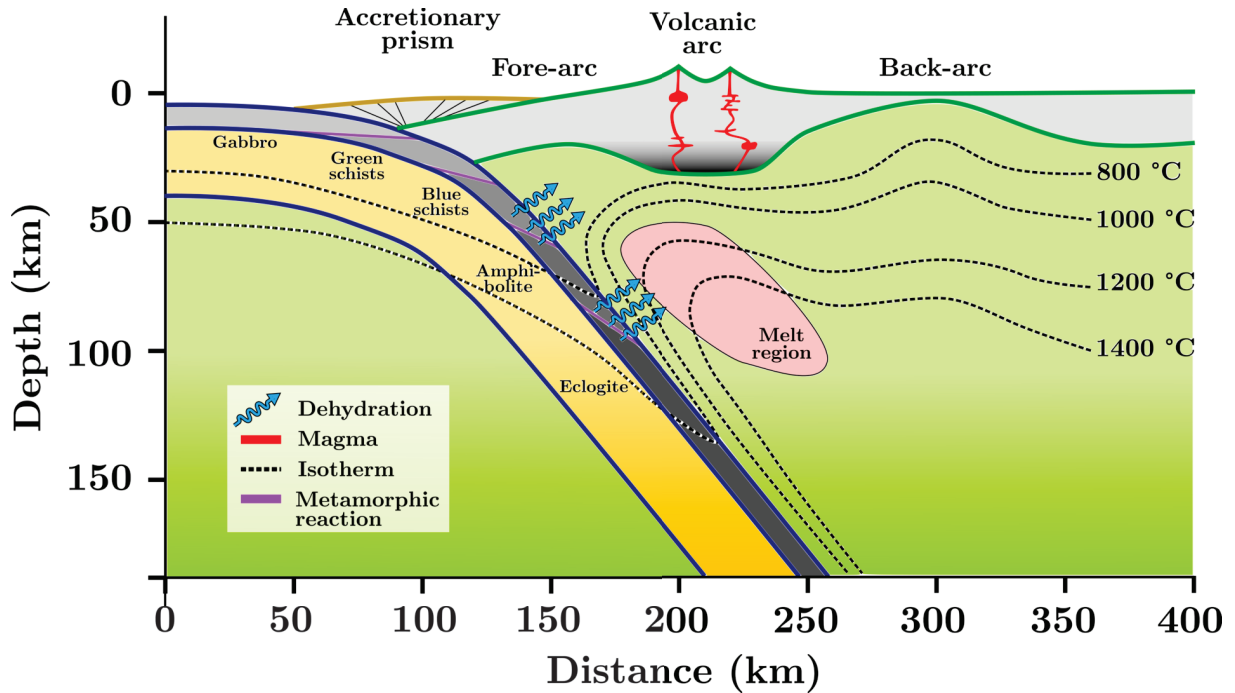


**Figure 5** – Simplified 2D view of a subduction zone. Metamorphic facies are given for the oceanic crust (gray). Yellow is oceanic lithospheric mantle. Blue arrows represent main dehydration locations along progressive phase transformations in the subducting crust

state. This is called metamorphism, and specific mineralogic compositions corresponding to specific pressure and temperature conditions are called facies. The first facies that a subducting oceanic crust goes through are the unperturbed basalts and gabbros. Those rocks then go through the greenschist facies, followed by the blueschist facies, amphibolite facies and finally the eclogite facies. This last reaction is what we defined as eclogitization earlier.

Every transition is characterized by a change in density as well as in volatile elements content (Kerrick and Connolly, 2001). Eclogitization in particular releases large amounts of water from the crustal minerals. The movement of water in and out of the oceanic crust and potentially mantle is helped by the bending, and subsequent unbending, of the sinking plate entering the subduction zone (Buffett and Becker, 2012). These rotational motions create preferential pathways for the fluids to migrate, as bending at the surface as the plate starts to dip towards the mantle creates faults where the water can infiltrate the crust and hydrate crustal minerals, therefore entering the subduction system. When the plate reaches a stable dip at about 20 to 50 km depth, it bends in the other direction to become flat again, which we call unbending (Singh et al., 2012). This creates new fractures that favour fluid exchanges in the system. Upon escaping the crust at the eclogitization state, the water hydrates the surrounding mantle, and thus facilitates the formation of

magma (Van Keken et al., 2002). This results in volcanic activity in the overriding crust. This activity depends on the hydration and thermal state of the subducting plate and therefore vary largely from region to region.

The subduction system is even more complex as it interacts with sedimentology rates and climate (Lamb and Davis, 2003). The first mostly has an effect on the hydration of the crust and the frictional behaviour of the interface, while the latter is influenced by the surface expression of the subduction in the form of the cordilleras, volcanic arcs and medium-to-large-scale intra-plate basins that can form in the back-arc. In turn, a strongly erosive climate such as the monsoon system can increase the sedimentation rate in the oceans, therefore affecting the friction of the subduction interface.

Previously, we classified subduction as a mostly 2D phenomenon, although there are always along-trench variations. The 2D properties of the subduction system, which are overall similar for subduction zones around the globe, help us get a good first order idea of the dynamics of the system. However, the fine 3D structure of every subduction zone is different. In our study, we will look at 2 regions in particular and analyze their 3D structure. The first one is western Greece. It is the place where the oldest oceanic lithosphere is still subducting today (Speranza et al., 2012). It sees the subduction of 230 million years old oceanic plate in the Mediterranean under the european continental plate. Being very close to termination on a geological time scale, it presents strong 3D patterns such as a pronounced bend from the north west in the Balkans to the south east and then east in Turkey. This makes 2D imaging challenging.

The second one is southern Alaska. It is at the intersection between the Aleutian subduction, where regular oceanic plate subducts mostly perpendicularly to the trench, and the North American cordillera, which subducts in the opposite direction as it crosses the Pacific ridge (Martin-Short et al., 2018). This setting is complex and the variation in the properties of the subducting material, as well as the orientation of the subduction, make it a strongly 3D setting. We will look at those two subduction zones using teleseismic imaging, which we will explain in the next sections.

## 2 Which tools do we have to image the Earth?

### 2.1 Geophysical exploration

One of the first geophysical tools used to explore the Earth was gravimetry (Jekeli, 2015). As described previously, it was used to discover the crustal roots of mountain ranges (Bouguer, 1749). Nowadays, the gravity field and its anomalies can be measured very

accurately from space using satellites (Tapley et al., 2004). Gravimetric studies are still actively used today, to study the composition of crustal anomalies in mountain ranges, or the characteristics of large earthquakes that happen in subduction zones for example (Panet et al., 2007).

Another type of geophysical exploration is electromagnetic sensing. It probes the electric conductivity and magnetic potential in the Earth (Fitterman, 2015). Changes in the magnetic field can be linked to variations in the dynamic of the core, which in turn affect aspects like the secular cooling of the Earth or volatiles transport from the inner core to the CMB (Cardin and Olson, 2015). Changes in the dynamics of the Earth's core have also been hypothesised to be linked to the formation of hot mantle material, called plumes, that rise from the CMB to the surface and can lead to continental size volcanic eruptions and continental breakup, both of which have been associated with mass extinctions (Ballmer et al., 2015). Changes in the electrical conductivity inside the Earth can be used to track the presence of various conductive elements and minerals. It is for example very sensitive to the presence of fluids such as free water in rocks (Worzewski et al., 2011). This makes it an effective tool to look at the dehydration in subduction zones that we described earlier.

The geophysical tool that we are probing the Earth with in this work is seismological analysis (Dziewonski and Romanowicz, 2015). As described in section 1.1, it uses the properties of the waves that travel through the Earth after it has been excited by a seismic event. This allows us to characterize the Earth in terms of velocities of wave propagation and density. These parameters can then be turned into information about the lithologies and thermodynamic conditions by combining the seismic observations with results from laboratory experiments. The triggering event can be natural (in this case the field of study is called passive seismology) or man made (in this case the field of study is called active seismics).

## 2.2 Seismic imaging

As stated above, there are two main ways of probing the Earth with seismic waves (6). We will first focus on active seismics, which uses man made seismic waves. In this case, one artificially creates seismic waves at the surface of the Earth using explosive or vibrating sources, and records them on dense arrays of receivers (Levander et al., 2007). This can be done on land or offshore. There are copious amounts of techniques that are used to exploit these data.

The advantages of active sources are numerous (Levander et al., 2007). First, they

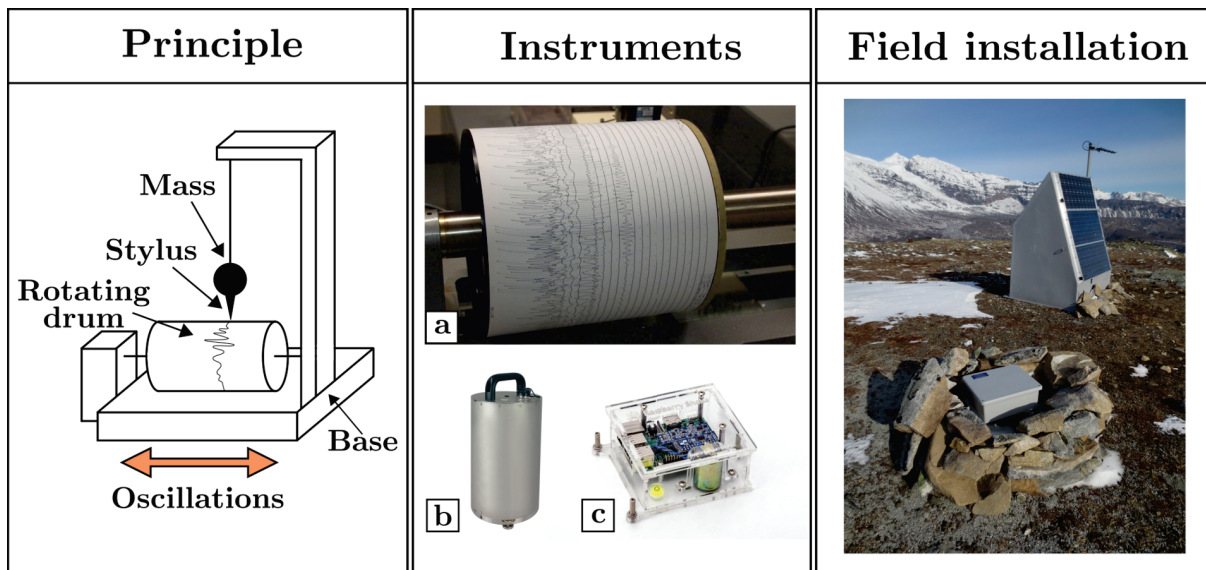


**Figure 6** – Seismic instrumentation. Principle of analog seismograph recording. The stylus and mass do not move with respect to the unperturbed Earth referential. The base and rotating drum are subject to the oscillations caused by the seismic waves, hence the information can be quantitatively recorded. Image from instrument (a) is taken from [wikipedia.org](https://en.wikipedia.org), instrument (b) from [guralp.com](https://guralp.com), instrument (c) from [raspberrypi.org](https://raspberrypi.org) and field installation from [earthscope.org](https://earthscope.org).

generate a well defined and known signal because we know the location and form of the source. This allows for easy data processing of the waveforms and clear identification of primary (incident P and S waves, see section 2.3) and secondary phases (scattered wavefield, see section 2.4) even without heavy treatment of the data. Second, the data can be recorded only when needed. There is only minimal data storage space wasted, and less processing to do after the recording of the waveforms. Third, the recording units, or seismic stations, can be chosen accordingly to the characteristics of the source. This means that the sensitivity, orientation and sampling rates of the instruments can be tuned to best suit the expected response based on their location relative to the source. Fourth, as a consequence of all previous advantages, the data coverage can be optimized for any study area or target. As an example, one can choose to use larger instruments on a larger area if the study sites are easily reachable, or smaller instruments in close vicinity if the locations are more difficult to access.

The drawbacks of active seismic experiments are that deploying many receivers can be time consuming and that most source generation methods are expensive to operate and maintain. Also, the waves generated with conventional techniques do not travel very far in most cases. This is because the energy they release is limited and their typical frequency range is above 1Hz, hence the waves are subject to high attenuation values.

This limits the volume that can be probed using a single study configuration.

The second way of determining seismic velocities and contrasts inside the Earth is passive seismology (Stein, 2015). In this case one uses the energy radiated from natural earthquakes occurring only hundreds of meters or up to thousands of kilometers away from the target area. This has several advantages over active seismics. First, naturally occurring earthquakes can illuminate the Earth from the interior, not only the surface. Intermediate depth and deep earthquakes provide not only information about the processes at play in their origin region, but also valuable information about the medium they propagate through on their way to local seismic receivers (Halpaap et al., 2019). Second, large earthquakes radiate seismic energy that travels across the entire Earth and can be recorded thousands of kilometers away. Because the forces at play in plate tectonics are several orders of magnitude higher than those of active seismics, sometimes dwarfing the largest nuclear detonations, the waves these earthquakes generate travel through all the layers in the Earth and provide unique information about the deep structure of our planet.

The main drawbacks of passive seismology are linked to the fact that these type of earthquakes cannot be controlled (Madariaga, 2015). First, they happen at random times, which means that we need to constantly monitor them to be able to record the information. Even though we can statistically estimate how many earthquakes of a given magnitude should happen in any given time period, we do not have the ability to predict individual earthquakes, be it in terms of timing or magnitude. Second, they are linked to tectonic processes and therefore only happen in specific regions around the world. This means that the data coverage cannot be perfectly optimized for specific studies. This can however be partly mitigated after large earthquakes that are followed closely by smaller earthquakes that release residual stresses, called aftershock sequences (Helmstetter and Sornette, 2003). Finally, unlike the artificial sources, they have complicated uncontrolled source signatures, or source time functions (STF). This can make it very hard to extract the desired signal needed for imaging within the complete recorded signal (Houston, 2001).

In addition to that, the amount of radiated energy is not azimuthally uniform. This is because natural earthquakes happen when tectonic faults abruptly move relative to another, and so the sources are characterized by two opposite motion vectors separated by a plane (Zhu and Helmberger, 1996). On either side of that plane, part of the material is compressed (the part that is at the tip of the vector), while the other part of the material is dilated. This creates four distinct regions, called quadrants, across which the source function varies. Finding the best way to extract the information from complicated waveforms is an active field of research that we will explore in section 4 of this chapter and in chapter 3.



Because they aim at exploring different parts of the globe and at different scales, active and passive seismic studies also face different challenges in terms of how they use the data to produce images of the Earth. In order to understand exactly how the methods developed for both fields differ, we need to describe the seismic wavefield in greater detail, starting with the difference between the direct, scattered, reflected and diffracted wavefields.

## 2.3 The incident wavefield

The wavefield can be separated into incident and scattered wavefields. The scattered wavefield can be further separated in reflected and diffracted wavefields. The incident wavefield corresponds to the solution of the wave equation in a layered, internally smooth, Earth model (Bostock, 2015). For teleseismic waves, it is composed of the primary compression body wave, called the P wave, the secondary shear body wave, called the S wave, the body waves that reflect at, or interact with, the major boundaries inside the Earth such as the CMB (e.g., PKP, SKS, SCS) or ICB (e.g., PKIKP) and the surface waves (see figure 7).

In the following, we will mainly be interested in the incident P and S body waves. As shown in figure 2, they oscillate in different directions, and have different velocities, with S waves being typically slower than P waves. They travel through the Earth following Huygens' principle (Huygens, 1690). Their velocities depend on the elastic parameters of the Earth, namely the Lamé parameters  $\lambda$  and  $\mu$  and the density  $\rho$  (Lamé, 1852). Those, in turn, are linked to the nature of the materials inside the Earth, and using our seismological tools we hope to resolve the composition and temperature of the Earth by mapping these parameters at depth.

One of the most used tools to estimate the elastic parameters of the Earth using the incident wavefield is called tomography. Similar to medical tomography, it uses the propagation path of the seismic waves inside the Earth and their travel times to estimate these parameters (Thurber and Ritsema, 2015). Knowing how long it takes for a wave to travel from the source to the receiver allows us to get access to its mean propagation velocity along its path. In order to compute the travel path of those incident waves, one usually has to resort to the infinite frequency approximation to provide the most direct path from a source to a receiver in a given Earth model (Buland and Chapman, 1983). Using inversion techniques and several sources and receivers, one can recover local wave velocities from these average results. This is the field of seismic travel-time tomography.

A short example of how it works for a 2D case is shown in figure 8. In this case, there are 2 sources and 2 receivers, hence 4 rays going through the imaging region. The

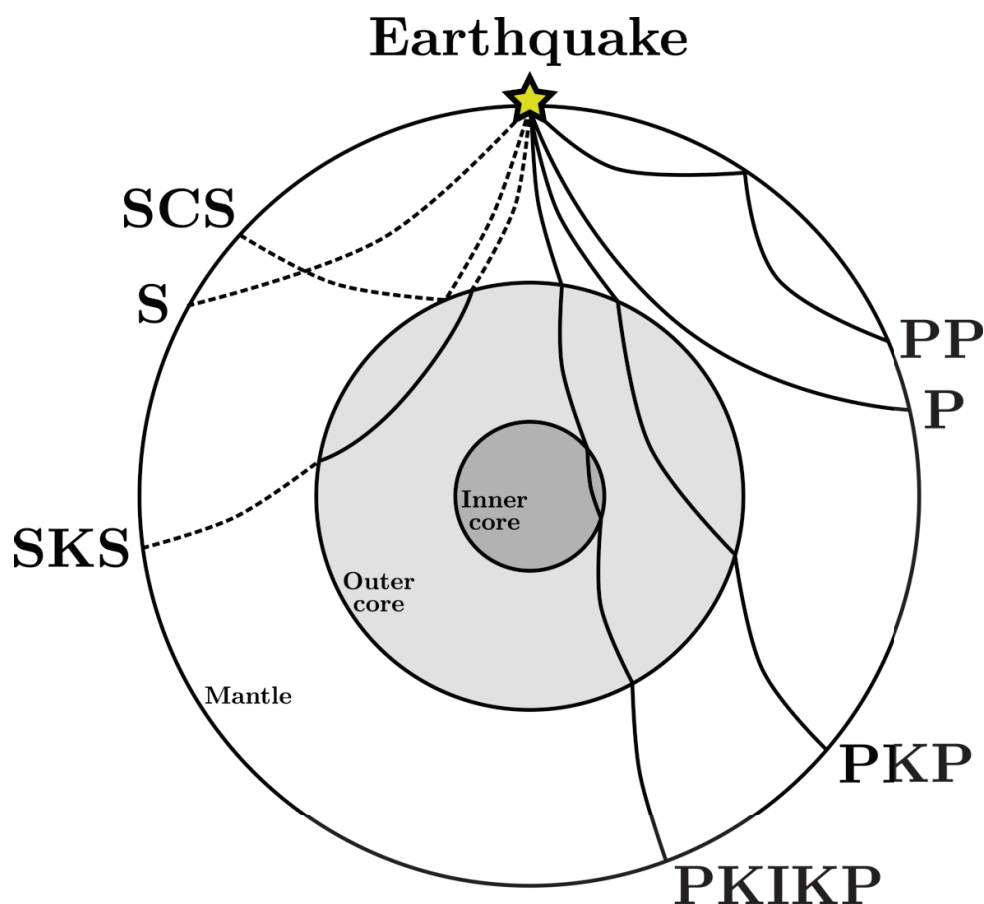


**Figure 7** – Main phases from the incident wavefield on a slice of the Earth. Star represent the hypocenter of the source earthquake. K is the name of a P wave inside the outer core, I inside the inner core, and C is a reflection at the CMB.

region has been separated in 9 areas to invert for seismic velocities. Squares A2 and B1 have one ray passing through, A1, A3, B2, C1 and C2 have two rays going through, and squares B3 and C3 have no rays traversing them. Also, there are only 4 rays for 9 velocities, which means that the system is ill-posed. Using this data and a simple linear tomography method, one could to obtain velocity values for the first 7 squares, albeit with large trade-offs, while values for the two orange squares are completely unconstrained.

Travel-time tomography is powerful but is limited by the data coverage and inversion parametrization, and rely on implicit or explicit regularization factors in order to provide an interpretable image of the Earth (Kissling et al., 2001). There are various ways to regularize the tomographic problem, but most methods rely on two main approaches (Charley et al., 2013). The first main type of regularization is damping, where one tries to stay as close as possible to a pre-established vision of the Earth while still being able to explain the observations. In the case of the previous example, choosing a pre-established value for the velocity in each square before the inversion would constrain the inverted

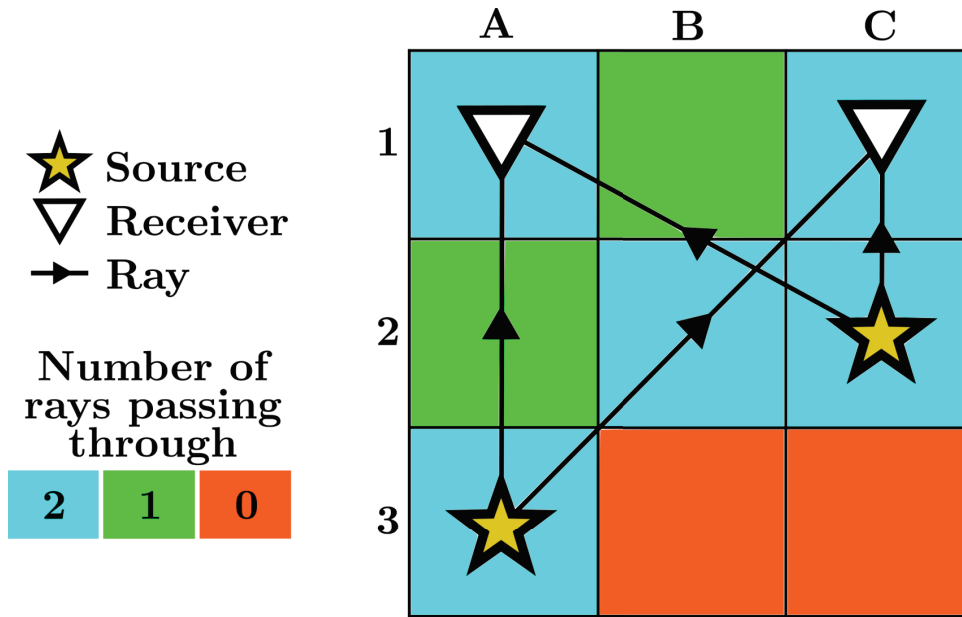


**Figure 8** – Simplistic arrival time tomography. Here 7 out of 9 squares have rays passing through them, sampling information along the way, and there is no ray, i.e. no information, going through squares B3 and C3.

velocity values for squares B3 and C3.

The second main type of regularization is smoothing, where values from a given parameter cell would affect the neighbouring cells to a certain extent while still explaining the observed arrival times. This usually allows to smooth out the small-scale variations that can arise when using noisy data. In the case of the previous example, a smoothed inversion would use the values from squares A3, B2 and C2 to constrain the inverted value and obtain a model with 9 velocity values. More advanced, iterative tomographic methods use adaptive parameterization in order to alleviate some of those drawbacks, or include data from the scattered wavefield to add more constraints on the inverted velocity models (Bodin et al., 2009).

## 2.4 The scattered wavefield

The scattered wavefield corresponds to the late arrivals recorded after the incident wavefield (Bostock, 2015). It represents the residual solution of the wave equation in a realistic, sharp Earth model after the incident wavefield has been removed. The scattered wavefield is comprised of all the reflections and diffractions that the incident wavefield generated when it interacts with the scattering structure of the Earth (figure 9). The scattered waves typically have a smaller amplitude than the incident wavefield and they can adopt a very complex shape with increasing number of interactions. By nature, they are linked to the

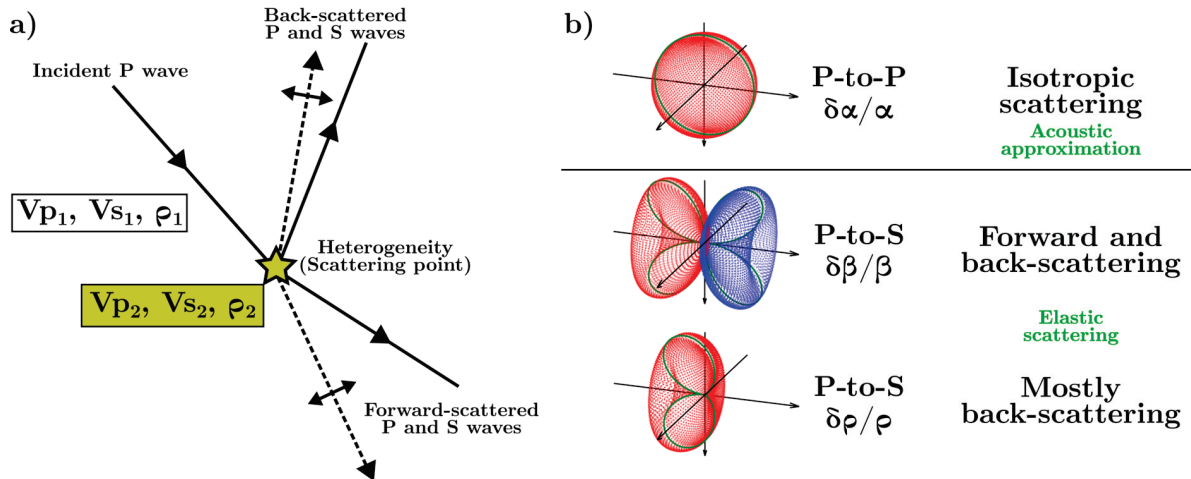


**Figure 9** – (a) Scattering geometry for a point scatterer. (b) Elastic scattering patterns represent the amplitude and polarity of the outgoing scattered wave depending on its orientation to the incoming wave. For example, P-to-S scattering with  $\delta\beta/\beta$  has very low, negative forward scattering amplitude following the direction of the incoming wave, but strong scattering amplitude at  $45^\circ$  forward (negative) and backward (positive).

scattering heterogeneities, and therefore hold information about the fine scale structure of the Earth. The scattered wavefield has been used extensively in the field of active seismics and is becoming a prominent tool to study the Earth through passive seismology (Rondenay, 2009).

#### 2.4.1 Active seismic experiments

The scattered seismic wavefield has been used in many ways over the past decades. One of its best known uses in active seismics is seismic reflection (Knapp and Steeples, 1986). In this method, one records the wavefield generated by artificial sources long after the incident wavefield to record the impulses of energy that travel down the Earth and are reflected at discontinuities inside the Earth (figure 10). It is used to characterize the location of interfaces inside the Earth. Reflection seismics follow the same basic ideas as travel time tomography, but this time instead of assuming a propagation path and looking for a velocity model, one assumes that the velocity of the wave through the medium is known and use the arrival times of the different scattered phases to infer the depth at which they were converted or reflected, i.e. their path. The velocity model can take the form a homogeneous velocity, a layered model or even a 3D model.

As in travel time tomography, the level of resolution can be enhanced by having multiple source-receiver configurations that illuminate the same depth points (Tarantola, 1984). However, opposite to travel time tomography, the improvement does not rely on the inversion, but rather on clever stacking of the signals to enhance the signal to noise ratio

(SNR) and obtain the image that shows the structures more clearly (Mayne, 1962). This means that there is no explicit regularization in this case, but that the velocity model that one assumes for the wave propagation becomes a critical factor for the imaging condition.

One method in particular, called Kirchhoff migration, will be of interest to us. It follows developments that started in the 1920's and was fully theoretized by 1954, as part of an array of methods aimed at 3D imaging of subsurface reflections (Hagedoorn, 1954). The basic principle can be explained as follows, and will be expanded upon later. In this imaging principle, the recorded wavefield is propagated back into the Earth from the receivers to the sources, i.e. backwards in time, at all potential scattering points. The migration method identifies the location of scattering points using the interference between the different waveforms, i.e. through constructive stacking.

The other main technique using the scattered seismic wavefield in active exploration is large offset seismic refraction (Lankston, 1990). In that case, one seeks to record not only the waves that reflect off interfaces but also the leading waves that travel exactly along these interfaces (figure 10). The properties of these waves allow the operator to retrieve seismic velocities in addition to the position of the interfaces (Yilmaz, 2001). Indeed, not only do these waves travel at the interface between two media, which is what we want to image, but they also travel at a velocity that corresponds to the fastest of the two media. By aligning the recordings and sorting them by distance, one can estimate the velocity in any given layer by looking for the value that gives the most coherent result for a given head wave (Zelt et al., 2003). This can then be repeated for every head wave at increasing depths, which will produce an updated velocity profile that is closer to the reality than the original one. These methods, which have been combined with reflection approaches in a coherent imaging theory over the past few decades, are very useful for oil and gas field discovery, but also seismic characterization of deep crustal structures (Rawlinson et al., 2001; Brocher et al., 1994).

### 2.4.2 Passive seismology

In passive seismology, there are many different scattered phases that can be used. They provide information about the scattering structure of different regions in the Earth. Figure 11 shows the three main regions around the path of the seismic waves where scattering takes place. During the rest of this chapter, we will only consider seismic phases that are scattered a single time. This is referred to as the Born approximation, and has proven to be effective at explaining most of the observed waveforms (Miles, 1960; Hudson and Heritage, 1981).

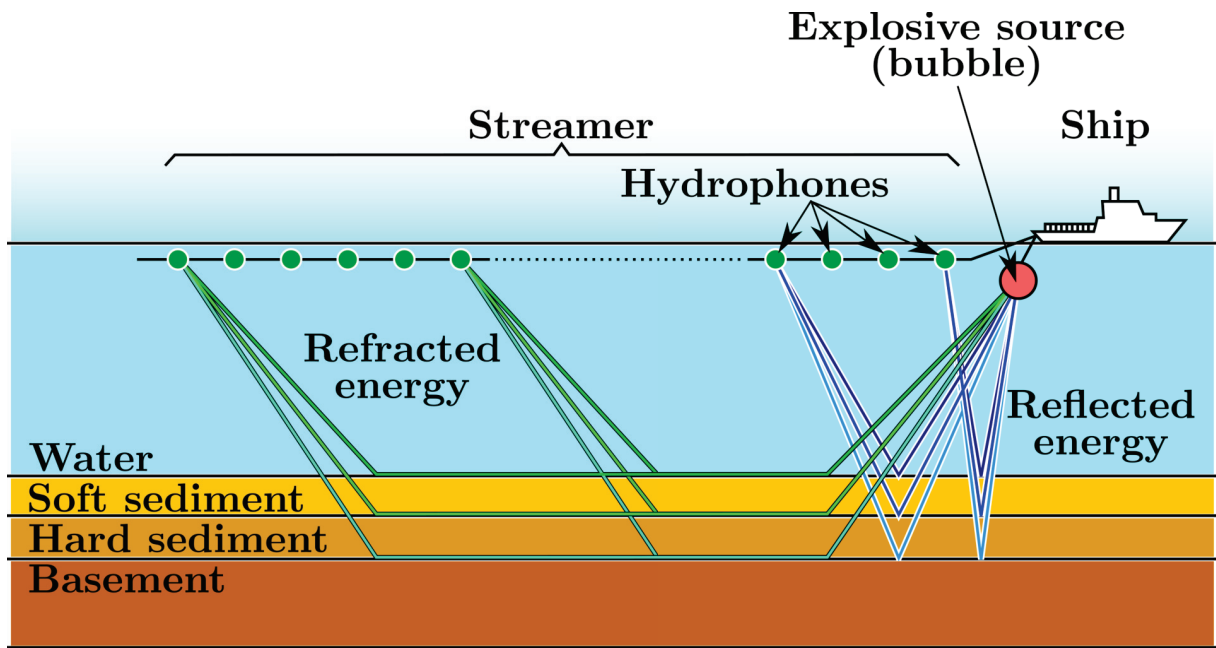


**Figure 10** – Geometry of offshore active seismic acquisition. Reflected energy gives direct information about the depth of the reflectors and the impedance contrast, whereas refracted head waves give information about the velocity of the medium.

The first region where scattering is an important factor is on the source-side. The most pronounced seismic phases coming from this region are the  $pP$  and  $sS$  phases, commonly referred to as depth phases (Wang and Zhao, 2005). They travel from the source directly to the surface (lowercase phase identification letter) and from there to the receiver (uppercase phase identification letter). In seismically active regions where there are strong, relatively flat layers with strong low velocity contrasts, the waves can be subject to critical reflections inside these layers. For example, in subduction zones, the low velocity layer in the top part of the subducted crust can act as a waveguide (Abers, 2005). These phases are usually considered as part of the non-random noise recorded at seismic stations, but can be used to our advantage and give us information about the precise location of the sources (Halpaap et al., 2019). For teleseismic receiver-side studies, these signals however only act as one more complexity in the source function.

Later along the path of steep waves, scattering can happen in the lower parts of the mantle. This is mainly observed on the incident  $PKP$  and  $SKS$  waves, which are phases that cross the CMB and travel through a part of the Earth's core (Vidale and Hedlin, 1998; Thomas et al., 1999). This type of scattering can generate  $PKP$  precursors for instance, which are linked to low velocity anomalies and partial melting at the CMB on either side of the travel path. These anomalies make certain branches, or ray paths, of the phase faster than the dominant  $PKP$  branch (called  $PKP_{df}$ ) and this delay gives us

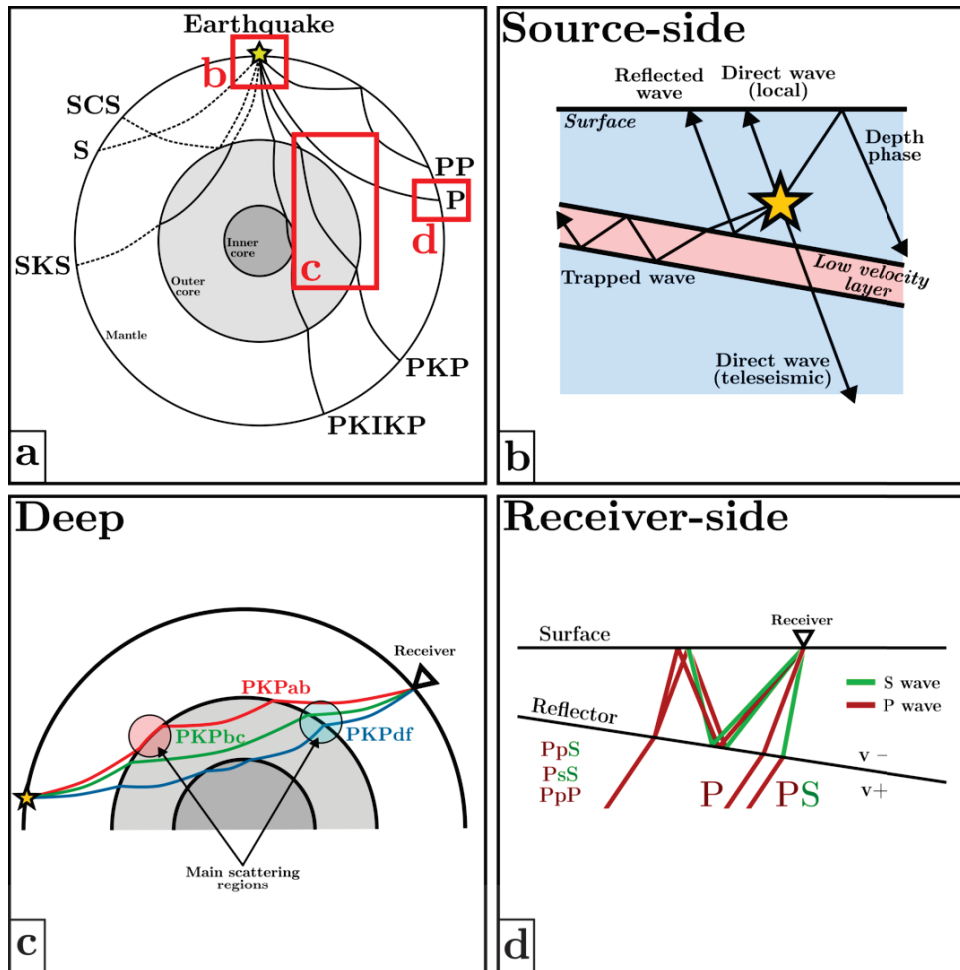


**Figure 11** – (a) Global scattering regions, with zoom-ins expanded in the rest of the figure. (b) Source-side reflections and trapped waves. (c) Deep scattering around the CMB for the core phases. SKS, PKS and SKP phases are also subject to scattering in the region. (d) Receiver-side transmitted and reflected first-order scattering geometries.

an idea about the strength of the very deep scattering in the mantle. These phases are visible only in the 110 to 170° of epicentral distance range due to the steepness of the waves that cross the CMB.

Finally, there are P-to-S and S-to-P conversions on the receiver side (figure 12). These are the ones that we will be interested in for the rest of this manuscript. The most prominent scattering happens when the primary waves are transmitted forward through the heterogeneous medium (Rondenay, 2009). The conversions of the incident P wave to S waves at the scattering structures generate signals in the coda of the main P arrival because the S waves are slower. Conversely, conversions of the incident S wave in P waves near the receiver create S precursors.

Another category of scattering happens when the waves approach the surface of the Earth. The incident wavefield can be reflected off the Earth’s surface and then be scattered

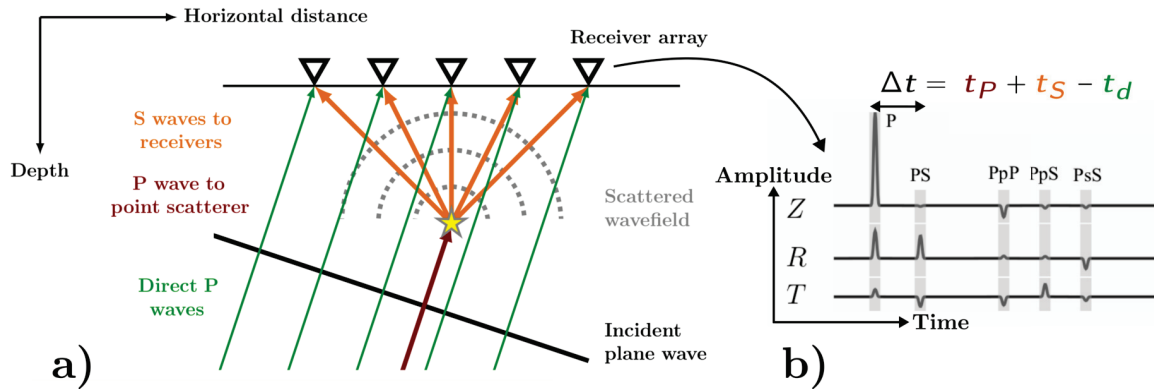


**Figure 12** – (a) Scattering and recording geometry of an incident plane P wave converted into an S wave by a point heterogeneity. (b) Noiseless three component coda of the P wave. The delay time  $dt$  between the primary P wave arrival  $t_D$  and the P-to-S scattered wave arrival  $t_p + t_s$  is linked to the individual travel times of each phase following  $dt = t_p + t_s - t_D$ . Following peaks correspond to the free surface multiples described in the text.

back towards the receivers by the same structures as the forward scattered waves (Tauzin et al., 2016). Those types of scattered phases are called free-surface multiples and are always in the coda of their respective incident phase. They are named after the nature of their interaction and propagation profile, with uppercase phase identification letters for upwards propagating waves and lowercase phase identification letters for downwards propagating waves. For example, if the incident P wave reflects down off the surface as a P wave and in scattered back up as an S wave, it will be called “PpS”. The four P wave scattered phases described in figure 11 (the forward PS, and the free surface reflected PpP, PpS and PsS) correspond to all the first order scattering interactions in the receiver-side region, and they are called scattering modes. These first-order scattering modes have been used in combination with the incident wavefield for full waveform tomography and in the form of receiver functions (RF) which will be described in detail in the next section (Bostock, 2015). These receiver side scattered signals are visible only in the  $\sim 30$  to  $95^\circ$  of epicentral distance range due to contamination by structures in the mantle transition zone (below  $30^\circ$  of epicentral distance) and the core phases such as PKP (above  $\sim 95^\circ$  of epicentral distance).

### 3 What methods are we using to image the Earth?

#### 3.1 Receiver Functions

As stated above, the signal recorded at a given seismic station depends both on the structure of the Earth, which we wish to constrain, and the signal from the source. The signal



from naturally occurring earthquakes can be complicated. It depends on the orientation of the faults at play and the origin, both in terms of location and tectonic regime, of the earthquake (Houston, 2001). Its duration depends on its magnitude and rupture characteristics (Bilek et al., 2004). Moreover, if the recording array is large, there is a risk that the source function is different on different parts of the array if they are in different quadrants of the source mechanism. Therefore it can be complicated to extract the signal from the scattered wavefield that corresponds to the Earth’s structure, as it can be overshadowed by the source signal of the incident wavefield.

In order to mitigate this issue, we resort to receiver functions (RF). The RF is a normalized record of the scattered wavefield from which the source signature has been eliminated. The RF aims at estimating the impulsive response, or Green function, from the Earth below the station, which depends on the seismic contrasts between the different layers, interfaces and heterogeneities in the Earth (Bostock, 2015). RF are based on precursory work by Phinney (1964) and were theoreticized seemingly independently by Vinnik (1977) and Langston (1979), the later of which coined the term receiver function.

The first applications used mainly P-to-S conversion (called P receiver functions, PRF) but the theory was quickly extended to S-to-P conversions (called S receiver functions, S-RF, Farra and Vinnik (2000)). The goal is to estimate the shape and duration of the source and to “remove” its effects from the recorded waveforms. What is important is not the absolute timing of the different phases but their relation to one another (Rondenay, 2009). Specifically, we look at the delay time between the incident arrival and the scattered phases, and this gives us information about both the seismic velocities in the Earth and the location of heterogeneities (see figure 12).

To demonstrate how to obtain and use these RFs, we have to understand how the seismic wave propagates through the Earth. In the case of the waves we are interested in, they are first generated, then scattered somewhere along their path from the source to the receiver, and finally recorded at the Earth’s surface. The recorded waveform is a time series that we will call  $w(t)$ , and follows this equation:

$$w(t) = s(t) * g(t) * r(t) \tag{1}$$

where  $*$  denotes the convolution operator,  $s(t)$  is the shape of the source (the source time function, STF),  $g(t)$  is the Green function, which represents is the response of the medium to an impulsive source, and  $r(t)$  is the response from the instrument to the shaking induced by the wave (Langston, 1979). This is illustrated in figure 13. Our goal is to retrieve  $g(t)$ , or an estimate of  $g(t)$ , because it contains all the information about

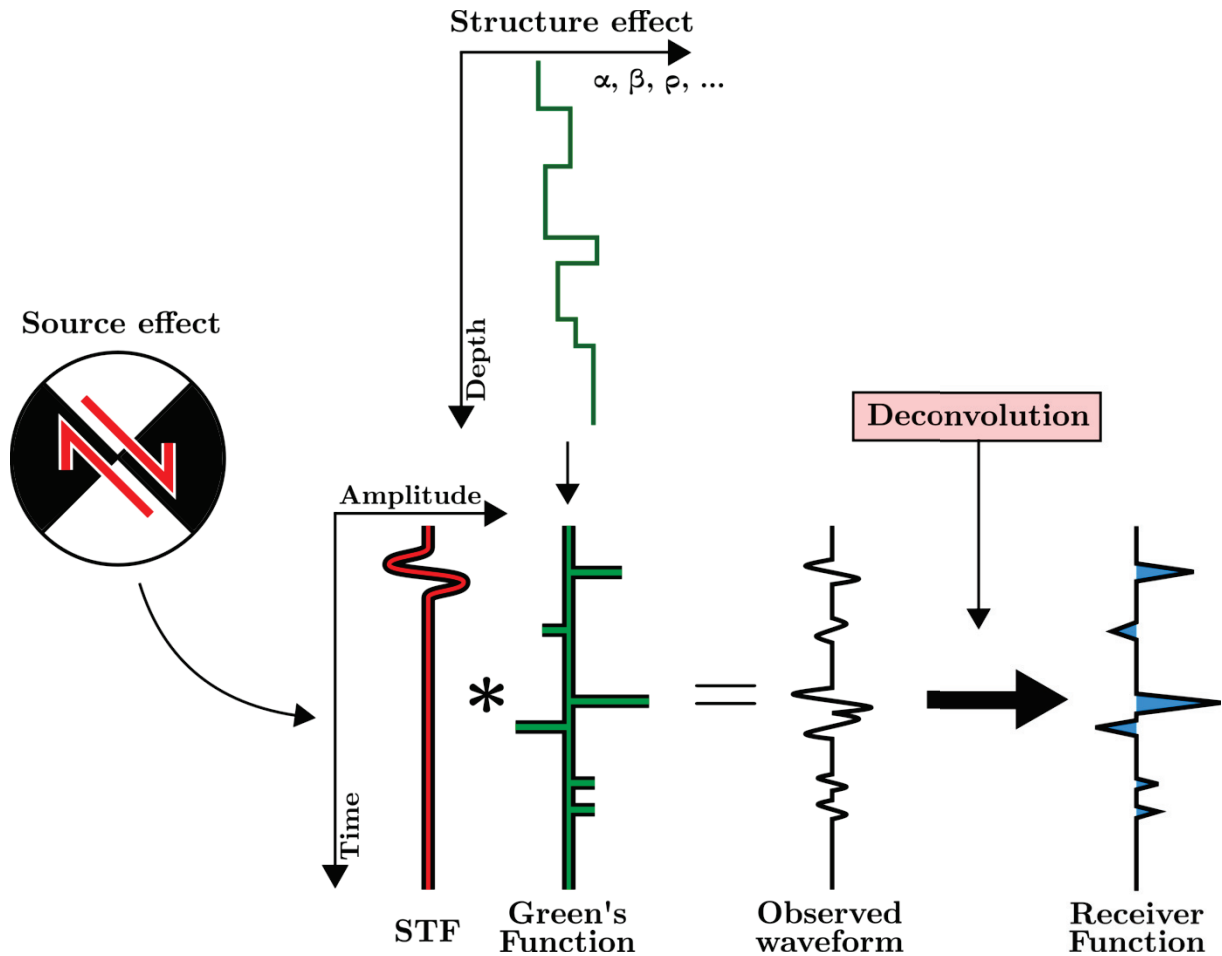


**Figure 13** – Graphic representation of the effect of the source and the structure on the recorded waveform with the convolution product. The deconvolution operation aims at estimating the Green's function of the Earth and produces the receiver function.

the structures that we are interested in (Bostock, 2015).

In order to obtain  $g(t)$ , we need to turn this equation around and isolate  $g(t)$ . The first thing that we do is to take care of  $r(t)$ . The instrument response  $r(t)$  is a well known function from the manufacturer of the seismometer, so it could be removed directly, but in general we combine  $r(t)$  with  $s(t)$ , assuming that  $r(t)$  is the same on all components (Owens et al., 1984). Ignoring  $r(t)$  for the sake of simplicity, we are left with  $s(t)$  and  $g(t)$  in the recorded wavefield. To obtain  $g(t)$ , we need to mathematically deconvolve  $s(t)$  from  $w(t)$  (Bostock, 2015). The convolution is a linear operator, hence the deconvolution is a linear inverse problem. The deconvolution is a critical step in obtaining the RF. If  $s(t)$  is known perfectly and the data  $w(t)$  is noise-free, then the deconvolution will yield an exact estimate of  $g(t)$ , i.e. the structure of the Earth along the considered raypath. However, in passive seismology the source is unknown, hence  $s(t)$  is only an estimate of the real source, and the data contains some noise.

In simple terms, practical deconvolution corresponds to removing the effect of an estimated source  $s(t)$  from the noisy recorded wavefield  $w(t)$  to get an estimation of the impulse response  $g(t)$ , which we call the RF. This can be done in the frequency domain, where a time deconvolution operator corresponds to a spectral division, or in the time domain, where it can be solved as a standard linear inverse problem. However, because of the noise and approximate source signature, this operation does not have a unique solution and is not stable. Therefore, the quality of the estimated  $g(t)$  will vary greatly depending on the way the deconvolution is performed (Spieker, 2017).

There are a few different ways to perform the deconvolution, and many more numerical implementations of the deconvolution operation (Ammon, 1991). The two key factors are the estimation of the source  $s(t)$  and the regularization of the inverse problem itself. We will go into further detail for both key factors in the methodological sections of chapters 2 and 3, and here we describe the main elements about the deconvolution process as a whole. First, as said previously, numerical deconvolution is not stable (Bostock, 2015). This means that we need to stabilize the problem, by way of regularization, in order for the noise to stay low, therefore potentially introducing artifacts into the waveforms. This also means that we will have to find ways to increase the signal to noise ratio if we want to obtain clear images, which we will describe later.

Second, the results can largely vary depending on the method used. To illustrate this point, we will compare two typical deconvolution methods: spectral deconvolution and iterative time deconvolution. We remind the reader that in the spectral domain, a time deconvolution operator corresponds to a spectral division operator. Hence, in the case of spectral deconvolution, problems arise when dividing with very small values in the spectrum.

A standard regularization that can be applied to the spectrum is called a “water-level” (Clayton and Wiggins, 1976). It sets a threshold under which the spectrum is boosted to a fixed value. This cancels the effect of small values in the division operator, removing the high frequency periodic noise that those would generate, but smoothes out the RF and can create large side-lobes if the threshold is too high as the number of sharp bends in the spectrum increases.

In the case of iterative time deconvolution, we iteratively add gaussian peaks to the RF and compare it to the original waveforms until a convergence criterion or a maximal number of peaks is reached (Ligorria and Ammon, 1999). The periodic noise issue does not appear nearly as much. However, in this case, we apply gaussian peaks with a fixed width to the RF, which can become problematic if the frequency content of the original waveform is significantly lower or higher than that of the gaussians we use. If we use

too narrow peaks, the deconvolution will tend to use many of them to create a broader peak. If the peaks are too large, then it becomes impossible to recover high frequency information.

Finally, an incorrect estimation of the source function will lead to a bad RF. Estimating the shape, amplitude and duration of the source function can be done in multiple ways. We can use single or multiple traces (Rondenay, 2009). Using multiple traces to estimate the source function helps to reduce the noise level in the final estimate, hence in the RFs, but relies on the assumption that it does not vary too much from trace to trace, which might be a problem for large arrays. We can use approximate or precise estimations of the incoming wave direction (Bostock, 2015). For example, in early RF works, the vertical component was often used as a good approximation for the source function as the incident P wave arrives nearly vertically under the receivers at these teleseismic distances.

Nowadays, with the advent of 2D and 3D methods, the source estimation has become more sophisticated, and we can rapidly compute precise polarization of the P wave with fast codes using back-azimuth and slowness, i.e. the geometric relation between the source and the receiver. We can use fixed or variable time durations for the source, with longer durations typically stabilizing the deconvolution (Spieker, 2017). Using a long fixed time duration can be helpful to automate the data processing and usually provides good results, but one might lack the ability to resolve P-to-P scattering in this case as it would be included in the source estimate as part of the incident P wave. Conversely, optimizing for the source duration helps alleviate this problem but is time consuming. All of these factors influence the quality of the deconvolution and of the final RFs.

Once these RF data have been computed, they can be used to image the Earth. So far, we remember that these signals are still time series, ideally composed of peaks with coherent relative amplitudes that correspond to scattering heterogeneities inside the Earth. In order to locate these heterogeneities in space, there are three main methods. The first family of methods aim at inverting large numbers receiver functions using fast 1D modelling with reflectivity methods (Shibutani et al., 1996). These methods are powerful in that they are very fast, easy to implement and provide a good first look at the structures.

The second family of methods is similar to travel time tomography detailed earlier, but takes the scattered wavefield into account, i.e. it inverts for the Earth's structure using the whole waveform as data instead of just the arrival times. It is called full waveform inversion (Ravaut et al., 2004). This method is powerful because it reconciles the large velocity variations that arrival times are sensitive to and the small heterogeneities that the scattered wavefield is sensitive to. However, it requires heavy synthetic waveform

computations for the inversion, which makes it computationally expensive (Virieux and Operto, 2009). The third family of methods associate every time step of the RF with a position in the Earth to locate the heterogeneities directly without using an explicit inversion. This is called the seismic migration, and we shall now describe it in more detail.

## 3.2 Classical migration in passive seismology

The basic premise of seismic migration is to go from one or many “amplitude vs. time” diagram to a “physical properties vs. position” image (Yilmaz, 2001). To do this we need to link (1) the amplitude of the waves to the scattering potential or velocity variations and (2) the travel times to the origin point of the scattering at depth. For the first link, we need a coherent scattering theory that can explain the amplitudes of the scattered waves correctly (Wu and Aki, 1985). For the second link, we need a velocity model in order to compute the arrival times for the scattered phases depending on their origin at depth. For extensive reviews on this topic, we point the reader to Rondenay (2009) and Bostock (2015).

### 3.2.1 1D stacking methods

The easiest way to obtain an image of the subsurface is by simply stacking the data obtained for individual stations from multiple earthquakes after simple geometrical corrections. We obtain a vertical profile of the amplitudes of the scattered phases under the station that can then be converted from time to depth in a second step. This is called a station stack (Lawrence and Shearer, 2006). In this method, stacking the data in the time domain allows to increase the signal to noise ratio as the peaks that correspond to signal should always be present and have the same polarity, whereas the noise should cancel out. However, one first needs to apply moveout corrections (Castle, 1994). This is necessary because slightly different rays cover different distances between the scattering heterogeneity and the receiver depending on their incidence angle, as can be seen in figure 14, therefore arriving at different delay times even if scattered by the same heterogeneity. The typical region that is affected is represented by a sensitivity region under the station that encompasses all the potential raypaths recorded at the station (Rondenay, 2009).

The data are stacked using a “normal moveout” curve, i.e. their timings are corrected to match the timing they would have had if they had arrived exactly vertically under the station. In a second step, one can convert the vertical axis from time to depth by

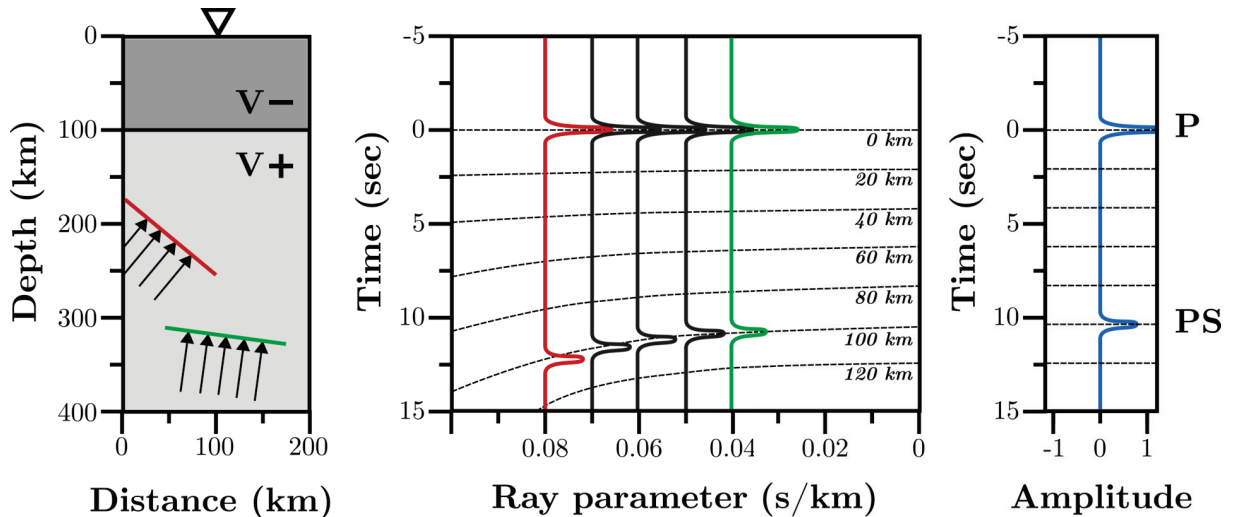


**Figure 14** – Moveout correction for the forward scattered P-to-S wave. Green waveform represents the steepest arrivals, from the most distant sources. Red waveform represents the sources closest to the receivers. Blue waveform is stacked data along the “moveout curves” in dashed lines.

computing the distance corresponding to the vertical ray path using a reference velocity model. This can be done simply by computing the travel times in each layer using the equation  $d = vt$  in every layer, where  $d$  is the depth, or thickness, that we are looking for,  $v$  the velocity of the wave in a given layer and  $t$  the time on the stacked RF. Finally, one can align the results for different stations in pseudo sections to showcase the shape and evolution of the scattering heterogeneities across larger areas (Tauzin et al., 2016).

The station stack method is very good to obtain a first order image of the fine structure of the Earth but it has a few critical caveats. In order for the stack to work correctly independently of the direction and distance of the source, two key assumptions about the medium are made. First, as said previously, the waveforms are corrected for moveout. Effectively, they are stretched and compressed to match the times it would have taken them to travel from the discontinuity to the surface if they were propagating vertically (Dunkin and Levin, 1973). Doing so means that we are assuming that the rays encounter the discontinuity at the same depth regardless of their angle of incidence, which is equivalent to assuming that the interface itself is horizontal. Second, the data are stacked the same way for all back-azimuths. Again, this assumes that the rays from all directions encounter the discontinuity at the same depth, which is only possible for a horizontal discontinuity. This method will struggle with interfaces that are not horizontal, which is a problem in subduction zones for example (Cheng et al., 2016). One way of dealing with this issue is to separate the data in back-azimuth and incidence angle bins and perform multiple analysis, but in this case the advantage regarding the improved signal to noise

ratio that we had when stacking as many waveforms as possible is lost.

An extension of this method is common conversion point (CCP) stacking (Dueker and Sheehan, 1997). It takes advantage of dense recording geometries in which the sensitivity region under the stations intersect, i.e. where rays coming from different incidences and back-azimuth angles cross at depth before being recorded at the surface. Those crossing points correspond to the aforementioned common conversion points. In this method, we migrate the corrected stacked RFs from several stations on vertical profiles at depths where their sensitivity regions intersect. Because the sensitivity region gets larger with depth, deeper points collect data from more stations (Rondenay, 2009). This allows to stack data from different stations at the same point in space, enhancing the signal to noise ratio of the images. This way of stacking the data also presents the advantage of taking some of the 2D and 3D scattering into account in the imaging and provides better lateral resolution. However, because the stacking still requires moveout corrections in order to work correctly, it fundamentally does not get rid of the horizontal interface assumption.

### 3.2.2 2D and 3D migration techniques

In order to tackle the horizontal interface issue, one needs to resort to more complex migration techniques. These are based on pre-stack migration, i.e. where the individual RFs are migrated in a discretized 2D or 3D model, or grid, using a reference velocity profile, before performing the stacking in the model space (Rondenay, 2009). Thus, instead of asking where the discontinuities are in a continuous 1D vertical profile, we interrogate every grid point in our model and determine whether it generates scattering or not. In this way, no explicit or implicit assumption is made about the shape and location of the scattering heterogeneities and interfaces (Bostock, 2015). On one hand, computing the arrival times in a 2D or 3D model allows to use the RFs individually with their respective incidence angle and back-azimuth without moveout correction, therefore removing the implicit horizontal interface condition. On the other hand, performing the migration for each RF makes these methods more computationally expensive, a potential issue we will explore further below.

We first explain how we migrate the recorded wavefield in pre-stack migration. As two faces of the same coin, we can consider the wavefield both in the data space as well as in the model space. First, let us consider the model space, which is the mathematical space in which we gradually build the Earth model that we aim to recover. In the model space, we propagate the energy observed at a given time in the recorded wavefield back to depth. We consider all the locations in the 2D or 3D model, i.e. all the grid

points, that could generate signal on the recorded waveforms at this given time (Yilmaz, 2001). This ensemble of points is called a migration isochron, and has the shape of an ellipse/ellipsoid in 2D/3D. Because we know that any scattered phase can only come from one heterogeneity (see section 2.4.2), we know that by stacking these migration isochrons, they will intersect where the scattering actually comes from, i.e. at the location of the heterogeneity, as shown on figure 15.

Second, we consider the data space, which is the mathematical space that contains the data as they are recorded before we use them in the migration. In the data space, this is equivalent to considering all the amplitude peaks that correspond to the same scattering point at depth on all waveforms. Because the waves travel more distance the further the station is to the heterogeneity, the delay between the incident wave and the scattered wave will increase. Therefore, if we align all the waveforms on the incident arrival, the signal associated with any heterogeneity will have the shape of a hyperbola, called the diffraction hyperbola. By correlating the correct peaks across the waveforms, we can recover the scattering hyperbolae and hence find the location of the scattering heterogeneities at depth, as shown on figure 15.

A scattering point propagates waves in all directions. However, the amplitude and polarity of those waves are not uniform, and vary spatially (Beylkin and Burrige, 1990). If the migration takes these variations into account, by treating the wavefields as vector fields, it is called elastic migration (figure 9). If it does not take them into account, by treating the wavefields as scalar fields, it is called acoustic migration. Acoustic migrations have the advantage of being easier to implement as they remove the complexity of the elastic scattering. Such methods have been implemented in the past. For example, the Kirchhoff migration that we briefly described earlier in section 2.4.1 has been adapted for acoustic migration by (Gray, 1986). Acoustic migration has been proven to be a good approximation if the scattering geometry is homogeneous in the study region or if one only considers limited incidence angle or back-azimuth ranges. However, it poses a problem when there are large lateral variations in velocity and steep reflectors (Cheng et al., 2016). In this case, one must resort to elastic migration to correctly interpret the waveforms.

One of such elastic migration methods is the generalized radon transform migration, or GRT (Bostock and Rondenay, 1999). It is based on the Kirchhoff imaging principle, and adds an inversion that uses the RF amplitudes to retrieve the velocity variations from the scattering potential. More precisely, it uses scattering patterns, which are a direct result from single scattering theory, and that predict the amplitude and polarity of the wave that is scattered depending on the scattering geometry and strength of the heterogeneity (see figure 9). Thus, the inverted expression of these scattering patterns allows to recover



## Scattering geometry

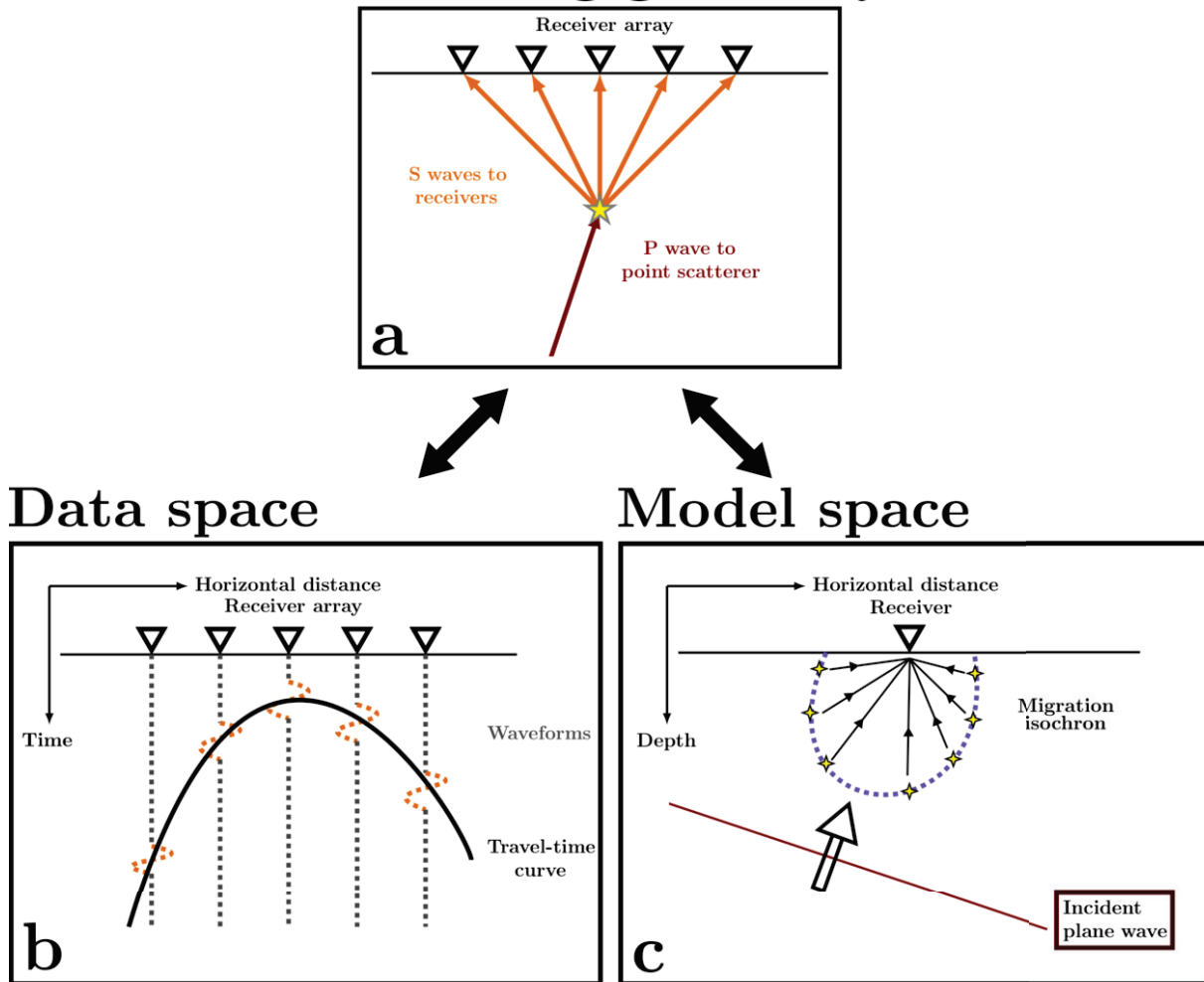


**Figure 15** – Shape of the wavefield. (a) Scattering geometry in the real subsurface. (b) Waveforms aligned on the primary P arrival. The travel-time curve corresponding to a given heterogeneity or interface takes the shape of a hyperbola. (c) Potential scattering points along the migration isochron. The constant delay-time curve takes the shape of an ellipsoid in 3D.

the variations in elastic parameters at the scattering point based on the amplitude of the RF (Bostock et al., 2001).

However, this method requires careful selection of the highest quality data to perform a stable inversion (Rondenay et al., 2001). Indeed, this inversion requires good coverage, or illumination, from all directions to produce a coherent result, and every grid point is only partially illuminated, due to bias in source distribution (see section 2.2). It can be done fully in 2D (Rondenay et al., 2005) or partially in 3D (Pavlis, 2011). The advantage of the 2D is that the inversion is performed only in the imaging plane, therefore reducing the illumination sphere to a circle, thus artificially increasing the illumination and stabilizing the inversion. This is even more valuable as we have seen earlier (section 1.2) that there

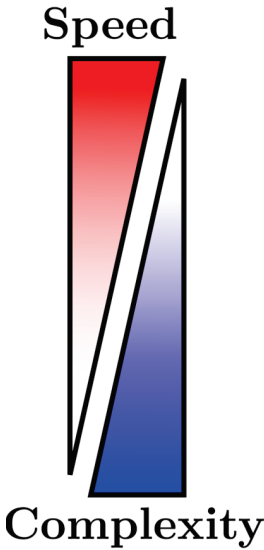
are many large scale geological structures that are mostly 2D, which makes this method very powerful for imaging of subduction zones for example. Attempts at developing a fully 3D GRT migration have been made, but so far, even if the migration is done in a 3D grid, the travel times are computed in a 1D velocity model (Pavlis, 2011). This is due to the fact that computing 3D travel times is computationally expensive.

Another fully 2D elastic method based directly on the wave equation, called reverse-time migration, or RTM, has been developed with the same goal (Shang et al., 2012). Unlike the Kirchhoff and GRT migrations, it uses the spatially discrete RF data to interpolate the scattered wavefield in the whole imaging region. It then propagates this continuous wavefield back in time using an elastic wave solver, and focusses the scattering potential at depth. Using an elastic solver allows to obtain elastic parameter variations directly from the recorded wavefield (Burdick et al., 2013). Similar to the GRT and Kirchhoff migration, this method makes no assumptions about the shape and location of the reflectors inside the Earth and interrogates every grid point for the presence of scattering. Similar to the GRT, this method is strongly influenced by the noise in the data, albeit not for the same reasons. In the case of RTM, there is no need for deconvolution, which removes one complexity step, but careful wavefield interpolation is required for the elastic wave solver to work correctly and provide a stable and meaningful answer (Shang et al., 2017). Similar to the GRT, partially 3D method computing travel times and paths in a 1D model, have also been developed, and fully 3D methods are still too heavy to apply to field data. Figure 16 summarized the different types of methods described in this section.

### 3.3 Towards efficient fully 3D migration

As stated in the previous section, attempts at 3D migration have been made, but none of the developed methods is fully 3D. Following the ideas of Cheng et al. (2016, 2017), our goal in this thesis is to not only perform the migration in 3D, but also to develop a new approach using fast running algorithms to compute the travel times in 3D, which is the main issue for the implementation of a fully 3D method. In order to obtain a fully 3D method, we base our method on the Kirchhoff migration principle (see sections 2.4.1 and 3.2.2) and use the fast marching method (FMM, de Kool et al. (2006)) to compute the necessary travel times in a smoothly varying 3D velocity model. This method is described in great detail in chapter 2. We will describe it here briefly, and illustrate it in figure 17.

Regarding the travel times, we first compute the travel time for the incident P wave from the source to the receivers (hereafter called  $t_D$ ). Then we compute the travel times for the different scattered phases. By combining these wavefields, we obtain the delay



Horizontal discontinuities	1D	<i>Reflectivity studies</i> <i>Station stacks</i>
	2D/3D	<i>CCP imaging</i>
Acoustic (2D/3D)	<i>Acoustic Kirchhoff</i>	
Elastic (2D/3D)	<i>GRT migration</i> <i>RTM</i> <i>Elastic Kirchhoff</i>	

**Figure 16** – Table summarizing the methods described in this section, with fast but geometrically limited methods at the top and slower, more complex and realistic methods at the bottom.

times for every grid point, which we will use in the migration later (Cheng et al., 2016). For the forward P-to-S scattering mode for example, we compute the travel time of the P wave from the source to every grid point (hereafter called  $t_p$ ) and the scattered S wave from every grid point to the receivers (hereafter called  $t_s$ ) in the 3D model. As shown in figure 12, they are linked by the equation:

$$dt = t_p + t_s - t_D \quad (2)$$

Where  $dt$  is the delay time that we compute for every grid point, and all points with the same  $dt$  are part of the migration isochron described in section 3.2.2. For the free-surface multiples (see section 2.4.2), we compute the travel time from the rays that reflect off the surface back at depth to every grid point as P or S waves, and the travel time for the P and S waves from every grid point to the receivers.

The interesting point in our implementation is that we can compute all these travel times very quickly and in only one step with the multistage algorithm that FMM provides (Rawlinson and Sambridge, 2004). FMM starts by computing the teleseismic P wavefield to every grid point including the surface, and keeps the surface timings in memory to compute the travel times from the free surface reflections to every grid point in the same step. The same time savings also apply to the travel times from the grid points to the receivers. This way of computing the travel time for all first-order scattering modes brings the computation times down to the same order of magnitude than the migration itself,

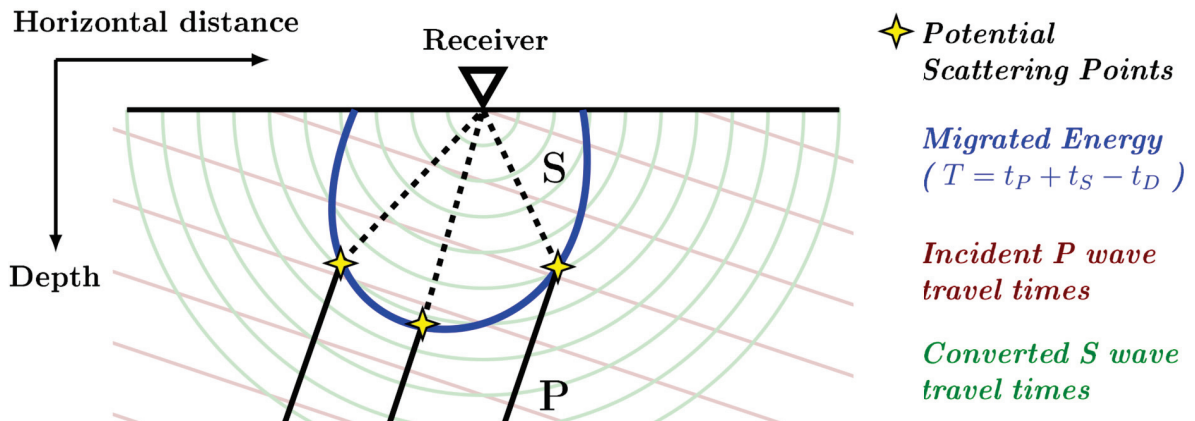


**Figure 17** – 2D representation of the 3D Kirchhoff migration. The incident P wave travel timefield for a given source is in red, the travel timefield for the scattered S wave for a given receiver in green, and the migration isochron in blue. The isochrone takes the shape of an ellipsoid in 3D. Stars represent examples of potential scattering points.

which is a significant improvement.

Regarding the migration, we project the amplitude of the multicomponent RFs, which represent the entire elastic wavefield, at depth in a 3D Earth model along the migration isochrons using the travel times we just computed (Millet et al., 2019). Unlike the GRT, we do not have an inversion and only recover scattering potential, which is one of the limitations of our method. However, unlike acoustic Kirchhoff, we take care of the amplitude and polarity of the scattered waves by applying corrections from scattering patterns based on elastic Born scattering theory (Beylkin and Burridge, 1990). As confirmed by synthetic tests in chapter 2, this allows to take all scattering geometries into account without having to compute the full wavefield. This also allows to discriminate, on a theoretical level, between the geometries that should contribute to the final waveforms from those where no scattering is expected. Finally, this allows to correct the polarities from the different scattering modes to obtain coherent images for all of them. Thus, we know that the relative amplitude in seismic velocities heterogeneities should translate into the same relative differences in scattering potential across the entire image.

The advantages of this proposed hybrid method are numerous. First, by separating the computations of the travel times and amplitudes, we drastically reduce the computation times. Second, we can take lateral heterogeneities into account as our reference velocities model are fully 3D. Third, we can obtain 3D images of the scattering potential to compare with 3D tomography and crust/slab models. Finally, there is less potential for artifacts to appear as the wavefield in our method resembles closely the way waves actually propagate through the Earth. The two main drawbacks are as follows. First, even if we use the fastest tools available, it is still time consuming. For our applications to field data in chapters 2

and 3, the computation times were around a few hours to a day, using a single core on a 2016 Dell XPS15 laptop with a i7-6700HQ processor, to obtain the final images. Second, performing a formal inversion based on the fully 3D Kirchhoff migration to obtain elastic parameter variations will be complicated, due to the same illumination issue as the GRT (see section 3.2.2). This means that we are limited to analyzing scattering based on the scattering potential, and have no explicit way of untangling the influence of  $\alpha$ ,  $\beta$  and  $\rho$  on the waveforms from each other.

## 4 What did we find out about the Earth?

In this section, we further discuss details on the method and present the scientific results obtained during the thesis. This includes implementation of the data downloading, processing and deconvolution, as well as the problems we encountered during the development of the imaging algorithm and the solutions we provided for the migration to perform smoothly. The second part of this section is devoted to summarizing the geological findings from chapters 2 and 3. These chapters correspond to a published article with an application of our method to the hellenic subduction zone (Millet et al., 2019), and a complete draft with an application to a composite dataset in southern Alaska to be submitted for publication respectively.

### 4.1 Methodological developments

#### 4.1.1 Data processing

As stated in section 3.1, we need efficient and robust data processing codes for the deconvolution and migration to work correctly. To that end, we adapted codes from the Global Lithospheric Imaging using Earthquake Recordings, or GLImER, database (Rondenay et al., 2016). These codes were developed for a massive worldwide RF database. Most of the data processing, quality control and event rejection and selection, is fully automated. After adjusting all the parameters for the particular needs of the Kirchhoff migration, we found that the data processing codes work best when we proceed as follows. We first create a list of events for the time periods that we are interested in, for events larger than Mw 5.5 and epicentral distances of 30° to 90°. Then we download the waveforms from the IRIS DMC database and start analysing them ([ds.iris.edu/ds/nodes/dmc](https://ds.iris.edu/ds/nodes/dmc)).

We perform signal to noise analysis on the vertical (primary P wave) and radial (scattered S wave) components to identify low, spurious or incoherent signals independently for every waveform (figure 18). We reject data with too low signal to noise ratio (SNR).

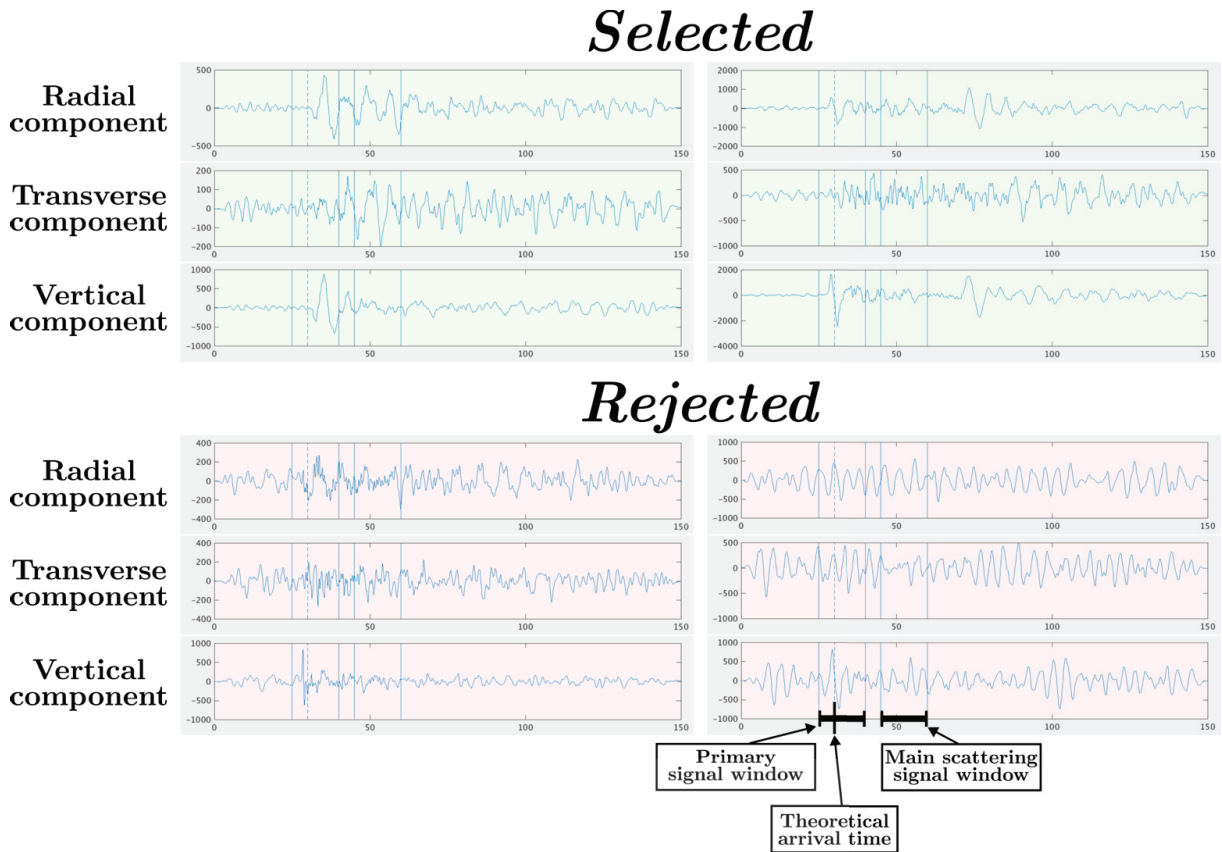


**Figure 18** – Automatic trace selection and rejection. The traces are aligned on the theoretical arrival and checked for SNR on radial and vertical components, as well as decay on the vertical component. The time windows for the computations are described in the text, and in chapter 3 in greater detail.

Here we define the SNR as the average energy of the first 15 seconds of the primary P wave signal compared to the 15 seconds before the onset of the primary P wave, and usually traces with SNR of less than 5.

We check for long STF by computing the decay rate on the vertical component. This value is computed by dividing the mean energy in the time range 15 to 30 seconds after the main arrival to the first 15 seconds after the main arrival. A long STF can create problems in the deconvolution so we reject those kinds of events, so we keep only waveforms that have a lower than 1 decay ratio. The decay ratio is defined as the average energy during the time period from 15 to 30 seconds after the onset of the primary P wave compared to the first 15 seconds of the primary P wave signal.

Finally, we check for completeness and coherence of the data across the array. Effectively, we only pre-select events that passed the previous criteria on at least half of the active stations at the time of the earthquake. This ensures optimal coverage across the array, is done automatically and has proven to give the best results in the migration.

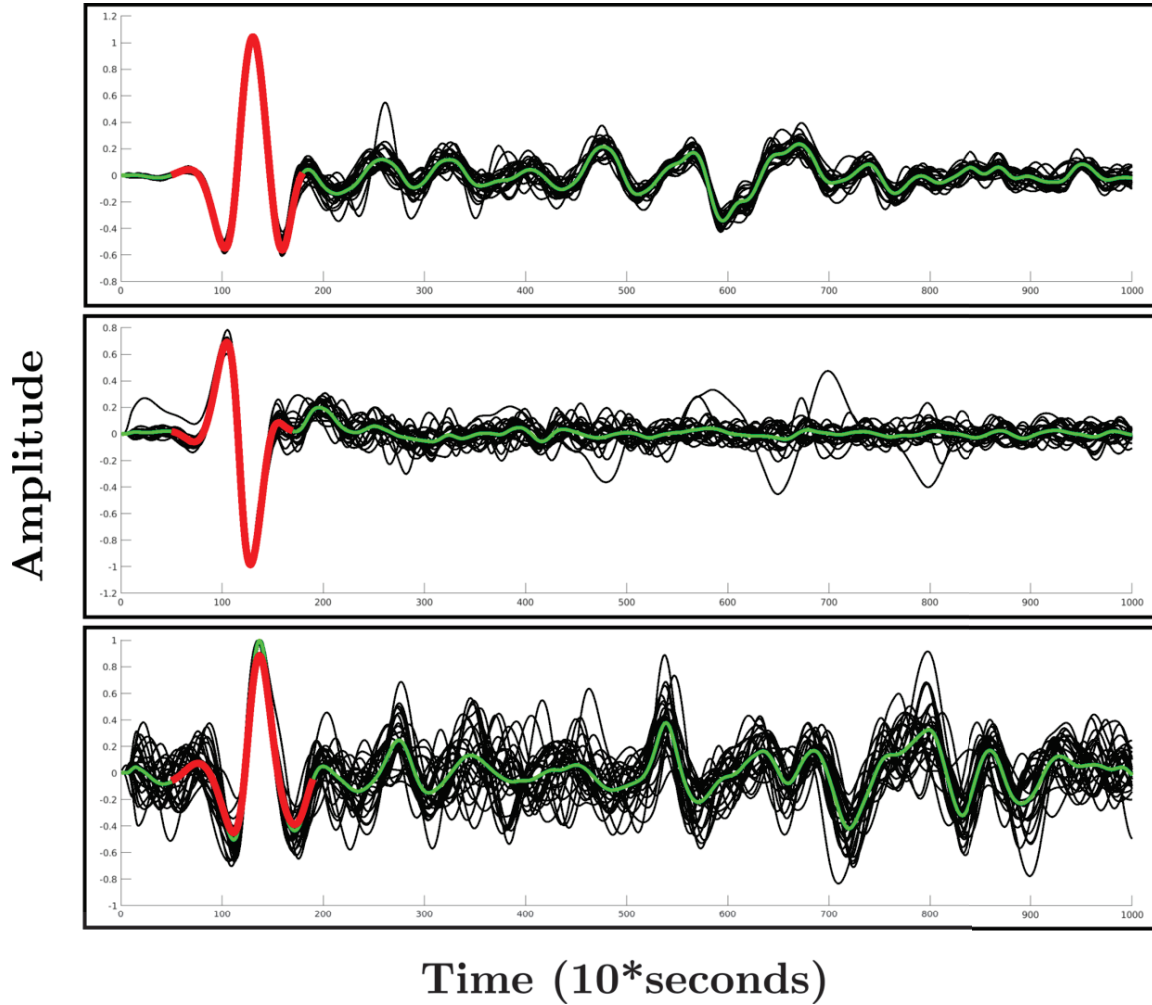


**Figure 19** – Source estimation with PCA for three different events. All waveforms for a given event in black, first component of PCA in green and the estimated source impulse in red. The STF is zero on the whole duration except for the impulse response (not explicitly shown here).

The pre-selected events are sent into the GRT pre-processing codes. The data are automatically rotated from the North-East-Vertical reference frame to the P-SV-SH reference frame and the waveforms for individual events aligned on the primary P arrival. This serves as a basis to estimate the STF (figure 19). To do so, we filter the waveforms and extract the common part of the aligned signals using principal component analysis (PCA) (Wold et al., 1987; Abdi and Williams, 2010). Effectively, the first component of the PCA roughly corresponds the average waveform from all the stations for a given event. This allows to remove the part of the P scattered signal (from the PpP multiple for example) that corresponds to dipping reflectors and point scattering from the source estimation, as their delay times will vary from station to station and not be reflected in the average waveform. This estimate is then cut to contain only the strongest first or first few oscillations, which is what we then use as the STF.

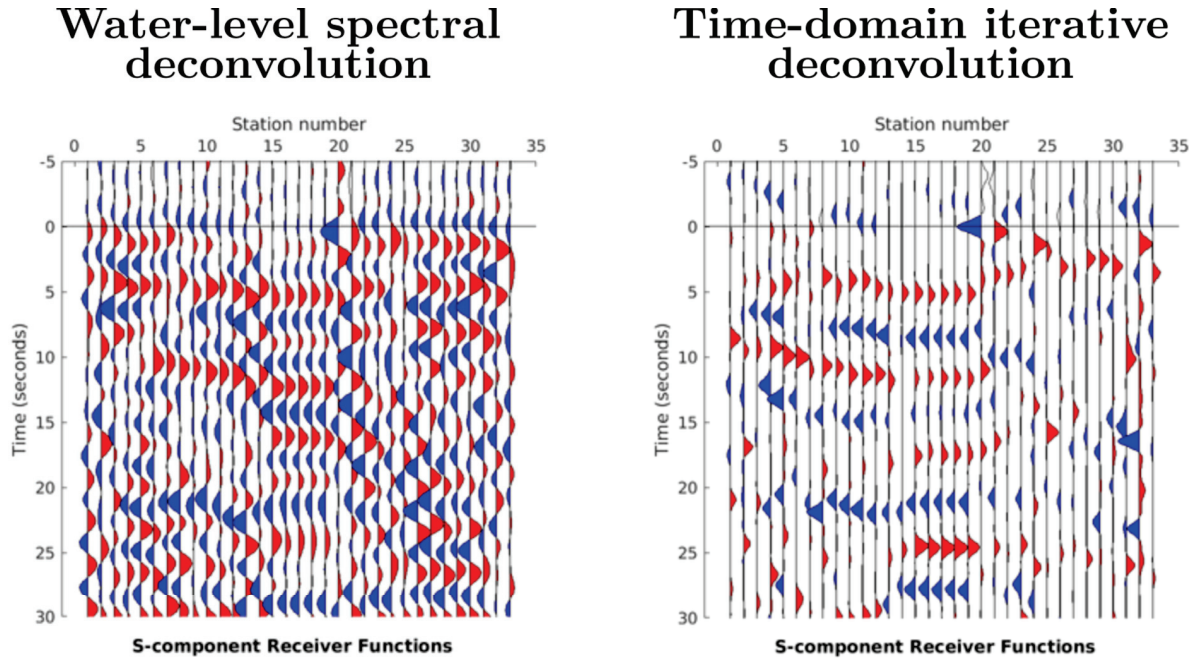


**Figure 20** – Results of the two main deconvolution types that we use on the same data. Data from the BEAAR array arranged from south to north (see chapter 3). One can see the continental Moho at  $\sim 5$  seconds, dipping slab top at  $\sim 8$  seconds and subducting Moho at  $\sim 12$  seconds. There are less oscillations on the time domain deconvolution, but multiples still clearly visible ( $\sim 21$  and  $\sim 25$  seconds for example).

We then perform the deconvolution of the three components waveforms by the source estimate. During our evaluation of the automation of this part of the processing, we have tested two different deconvolution methods (Spieker, 2017). The first one is a spectral division code with automatic noise detection and frequency dependent water-level selection (Clayton and Wiggins, 1976). It has the advantage of being fully automated, quick, stable and with less artifact than classical water-level type deconvolutions (figure 20).

The second one is an iterative time domain deconvolution based on Ligorría and Ammon (1999). It is slower but provides high quality RFs that contain less unwanted oscillations (figure 20). In this method we choose a width for the gaussian peaks that we add on the RF, which effectively acts as a filter (see section 3.1) and controls the frequency content of the final RFs. In both cases, the deconvolution is performed independently on all 3 components of the wavefield, hence we obtain one RF per component on the P-SV-SH reference frame.

Finally we rotate the data in the Radial-Transverse-Vertical reference frame for use in the migration code. Data for the hellenic subduction zone (chapter 2) were provided by Stephane Rondenay and obtained using a spectral deconvolution, whereas data for the southern Alaska subduction zone (chapter 3) were obtained directly from IRIS (`ds.iris`).



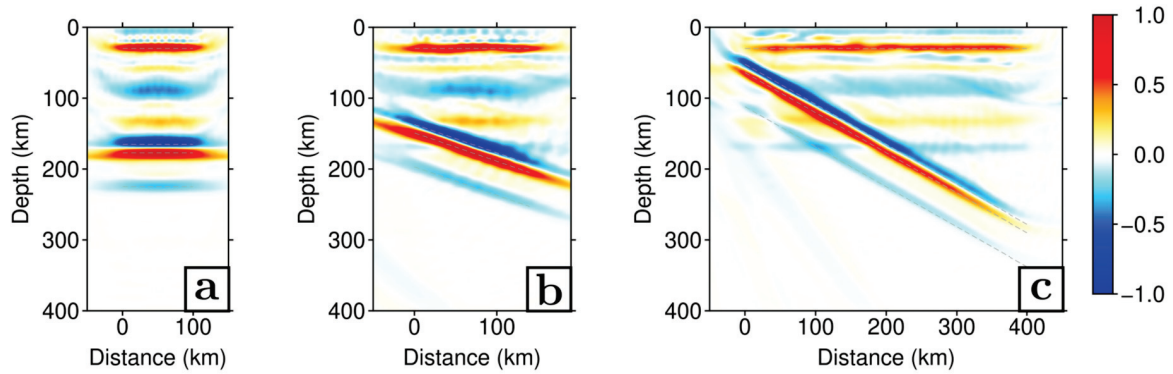


**Figure 21** – Off-dip profiles across the 3D migrated image of a synthetic subduction zone model. The receiver array is 100 km in the along-strike direction and 400 km in the dip direction. Profiles are cut through the imaged volume (a) along-strike, (b) oblique and (c) in the dip direction. The imaging principle recovers the correct depths and dips of structures in all cases, regardless of orientation.

[edu/ds/nodes/dmc/](#)) and deconvolved using the iterative time domain method.

#### 4.1.2 Migration and imaging

The four key points and improvements of our method are (1) fast fully 3D travel time computations using FMM, (2) elastic scattering amplitude and phase corrections using scattering patterns, (3) multi-component receiver functions and (4) linear and non-linear multi-mode stacking. We compute the travel times for the four main first order scattering phases PS, PpP, PpS and PsS, using the efficient FMM eikonal solver in a 3D velocity background. Given an accurate 3D velocity model, the computed wavefields resemble closely how the waves propagate in the real Earth (de Kool et al., 2006). In addition to correct travel times, these 3D calculations also provide us with an accurate description of the scattering geometry, i.e. the angle of the incoming and scattered waves, at each point in depth, which can in turn be used to apply elastic corrections, i.e. the scattering patterns. We use the four scattering modes in conjunction using linear and nonlinear stacks (Tauzin et al., 2016). During the stacking operation, the four scattering modes add up where they provide coherent information and spurious signals are reduced. Noise is also reduced.

When optimizing the multi-mode migration, we found that the stacking is more efficient if we allow for different data to be used in different modes. We can use RFs with different frequency content, or even obtained using different deconvolution techniques, for different modes. For example, as discussed in chapter 2, the free-surface multiples have a higher resolution power (Rondenay et al., 2005). This can be useful at times but the

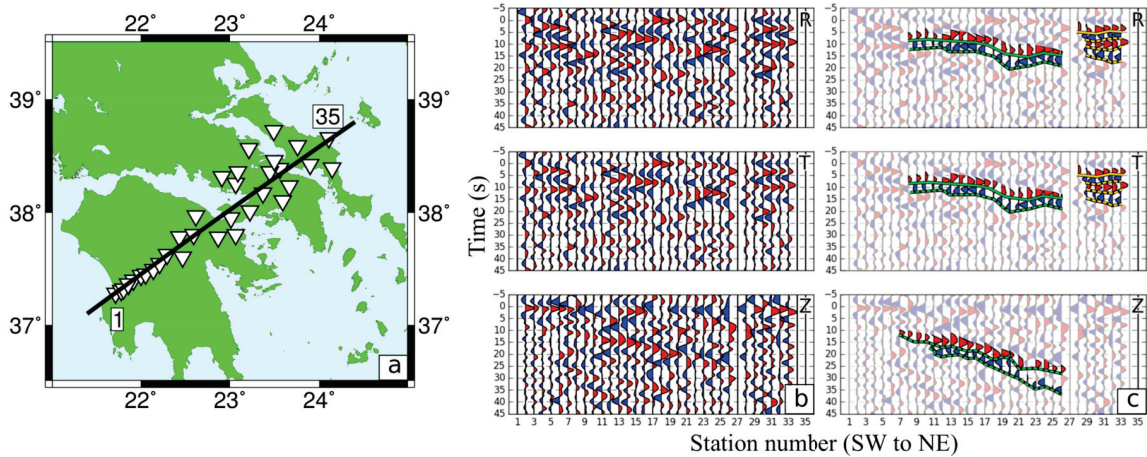


**Figure 22** – Setup, raw and interpreted data from the MEDUSA experiment. (a) corresponds to the array setup, with white triangles representing the stations position from 1 (south-western corner) to 35 (north-eastern corner) and the projecting line in solid black. (b) is the data for one event sorted by station number. (c) is the interpreted data where we highlight the presence of the continental Moho (orange) and the subducting slab (green). We differentiate between the forward conversions (solid lines) from the free surface multiples (dashed lines).

stacking tends to be less effective when the vertical resolution of the various scattering modes are different and stations further apart. Therefore, in our analysis we use lower frequency RFs for the free surface multiples than for the forward scattering (Millet et al., 2019).

By optimizing the amount of calculations required to compute all the travel time fields using the FMM solver and by simply applying geometrical elastic amplitude corrections (see section 3.3), we manage to obtain 3D elastic migration images in reasonable time. Once we obtain the 3D model of scattering potential inside the study region, we can draw arbitrary line through it to visualize 2D sections under the densest parts. Synthetics tests show that we are able to retrieve correct polarities, amplitudes and relative contrasts between different interfaces for all potential scattering geometries (Millet et al., 2019). We also show that we are able to retrieve very steep dip angles (up to  $80^\circ$ ). However, in this case the free-surface multiples tend to become less useful, hence the multimode migration as well. In our tests, synthetic Earth model have a size of  $5^\circ \times 5^\circ \times 400$  km with a grid spacing of 5 km in all directions, but we note here that it is scalable, albeit at the expense of the grid spacing.

Our applications to both synthetic and field data show that we recover the 3D structure of the Earth accurately, and unlike typical 2D methods that need to assume certain symmetries along the dip axis, we can recover along-strike structure. This is a key point as it allows to use 3D array geometry to its fullest (figure 21, reproduced from Millet

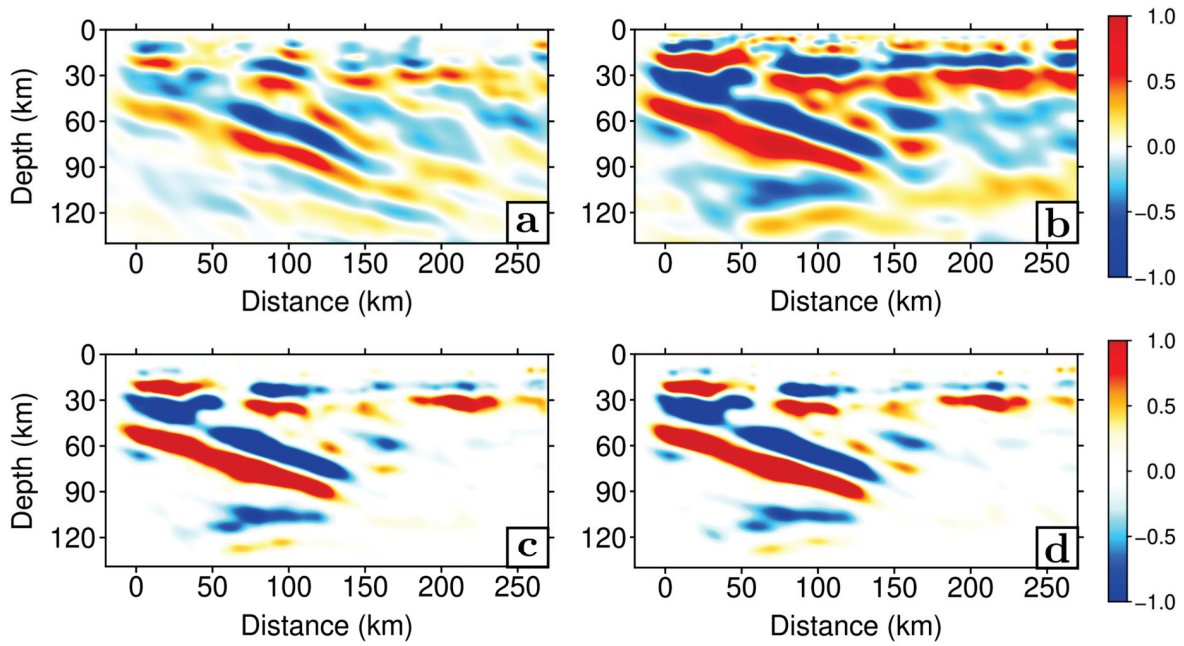


**Figure 23** – Images obtained with the multi-mode migration on the MEDUSA experiment dataset. Panel (a) shows the linear multi-mode migration with original geometry. Panels (b)-(d) show the linear, phase-weighted and 2<sup>nd</sup> root multi-mode stacks with data projected on the migration line, respectively. The overriding Moho, the subducting crust upper and lower limits are clearly imaged.

et al. (2019)). Another key point in the accuracy of the method is that, because we do not project the data on a given migration line beforehand, we are sure to migrate the data where it comes from and not next to it. This leads to less artifacts in the final image. This point can be contrasted however by the artificial enhancement in station density that 2D methods achieved by merging regional arrays onto linear migration lines (Bostock and Rondenay, 1999).

## 4.2 Application of the migration method to the Western Hellenic subduction zone

In this section, we briefly describe the main objectives and findings of the paper reproduced in chapter 2 (Millet et al., 2019). In this paper, we describe the migration method in greater detail and explicitly derive the equations for our Kirchhoff imaging principle, as well as the implementation of all the functions of the algorithm in the numerical code. We show the results from synthetic tests, and how we can recover scattering structures accurately with minimal artifacts, as well as an application to real data from the MEDUSA experiment in the western hellenic subduction zone (Rondenay, 2006; Pearce et al., 2012).

We confirm the observations by (Pearce et al., 2012), which we share the same data

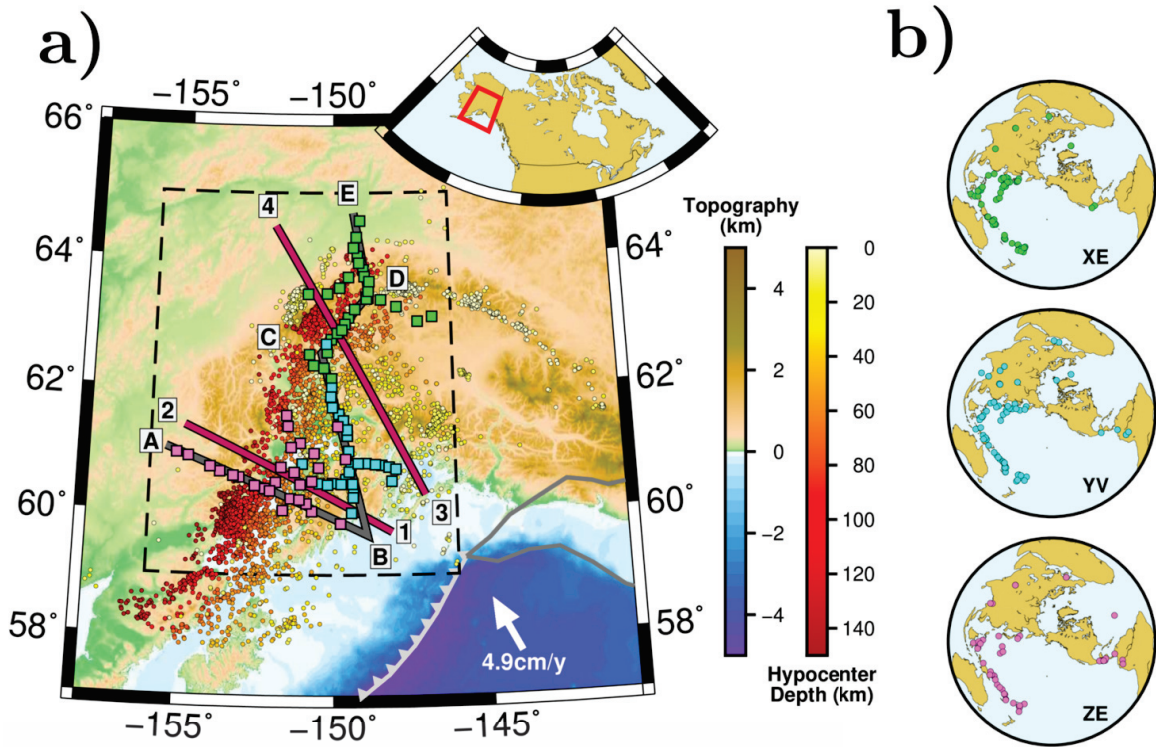


**Figure 24** – (a) Map of Southern Alaska. Stations colored by array: BEAAR is green, MOOS blue and SALMON pink. Events obtained from the AEIC catalog and colored by hypocenter depths. Lines 1-2 and 3-4 represent the 2D GRT migration lines. Lines A-B, B-C, C-D and D-E are the slices through the 3D Kirchhoff migration model. (b) Distribution of earthquakes selected for the final migrations on the three arrays.

with (figure 22, reproduced from Millet et al. (2019)). This serves to validate both previous results and our method. We show that our method provides good images with the unaltered 2D array geometry, and that by performing the same projection on the migration line before the migration we obtain very similar images to (Pearce et al., 2012).

More specifically, we find that our images are similar to those obtained by 2D GRT migration. The overriding Moho from the Eurasian plate, the African subducted slab top and Moho are visible at the same depth, and with the same dip, as the GRT images. The results from this study show a thickness of the subducted low-velocity layer that is in agreement with the previous GRT results. The final results are visible in figure 23, reproduced from Millet et al. (2019).

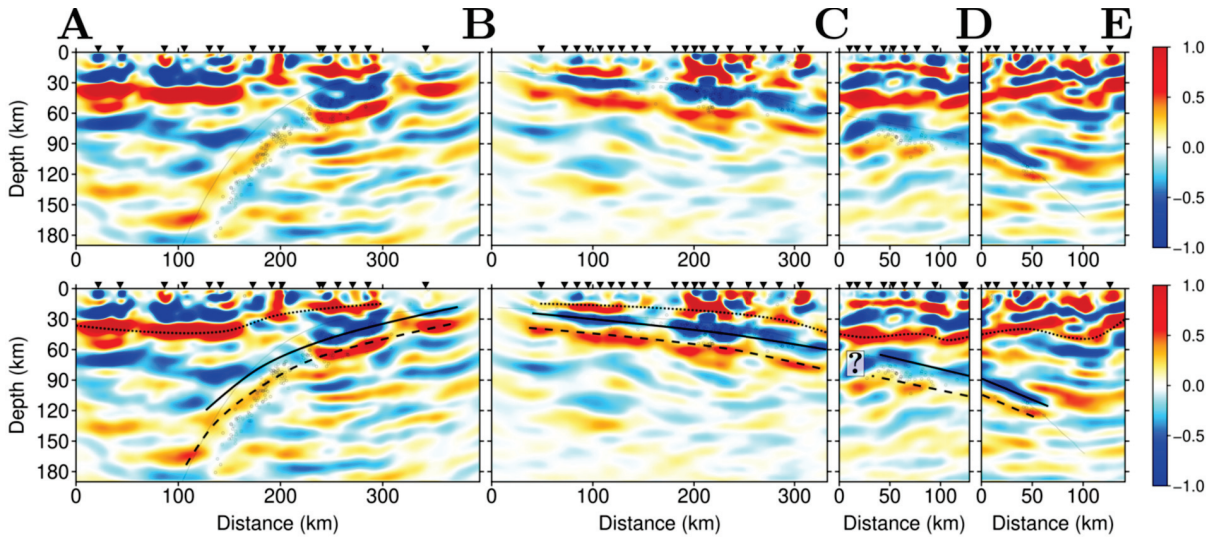


**Figure 25** – Kirchhoff images along lines A-B, B-C, C-D and D-E. (a) Final linear multi-mode profiles. Thin black line represents the slab contour based on slab2. (b) Interpretations. Thick dotted lines represent the continental Moho, thick solid lines represent the slab top and thick dashed lines represent the oceanic Moho.

### 4.3 Application of the migration method to the Southern Alaska subduction zone

In this section, we briefly describe the main objectives and findings of chapter 3. In this chapter, we describe the data processing that is used to transform the raw seismic recordings into usable RF in greater detail. We start by expliciting all the parameters for the filtering, source estimation and deconvolution of the data. We discuss the limits of the automation of the data processing and how we need to visually check the data to ensure optimal quality deconvolved data before the migration process. We compare the advantages and drawbacks of the 2D GRT and 3D Kirchhoff methods, that we both use in the study. We describe how they provide complementary views on the Southern Alaska subduction zone (figure 24), as their different imaging resolution and resilience to 3D artifacts allow to cross-check the results. We then apply both methods to data from three temporary networks deployed in southern Alaska over the past 20 years and analyse the results.

We confirm the results obtained previously by Rondenay et al. (2010); Kim et al. (2014) regarding the North-South transect across the region through the subducting Yakutat terrane. The same change in subduction dip and low-velocity crutal layer is observed and linked to the transition from the Pacific to the Yakutat slab. We use the novel SALMON array (Tape et al., 2017) to explore the differences between the previously imaged Yakutat and the more classic Pacific plate subduction to the west of it, providing the first high

resolution scattered wave image of the Pacific slab in this region.

More specifically, we find that our results show that the transition from the Pacific crust to the Yakutat terrane, which is marked by an abrupt change in crustal thickness at depths of 60 to 80 km in both methods, happens further north than previously thought. The subducted Pacific plate is observed down to 170 km to the northwest of Cook inlet. The Kirchhoff migration also shows a departure at depth between the imaged subducting interfaces and the seismicity envelope in this region, which is linked to the progressive eclogitization of the crust. There is no clear evidence for this phenomenon under the Denali Volcanic Gap where the Yakutat terrane subducts under Alaska. The final results are visible on figure 25.



# Bibliography

- Abdi, H. and Williams, L. J. (2010). Principal component analysis. *Wiley interdisciplinary reviews: computational statistics*, 2(4):433–459.
- Abers, G. (2005). Seismic low-velocity layer at the top of subducting slabs: observations, predictions, and systematics. *Physics of the Earth and Planetary Interiors*, 149(1-2):7–29.
- Aetius (n.d.). *De fide*.
- Ammon, C. (1991). The isolation of receiver effects from teleseismic P waveforms. *Bulletin-Seismological Society of America*, 81(6):2504–2510.
- Anderson, D. (1967). Phase changes in the upper mantle. *Science*, 157(3793):1165–1173.
- Anderson, D., Sammis, C., and Jordan, T. (1971). Composition and evolution of the mantle and core. *Science*, 171(3976):1103–1112.
- Aristotle (n.d.). *Meteorologica*.
- Badro, J., Fiquet, G., Guyot, F., Gregoryanz, E., Ocelli, F., Antonangeli, D., and d’Astuto, M. (2007). Effect of light elements on the sound velocities in solid iron: Implications for the composition of Earth’s core. *Earth and Planetary Science Letters*, 254(1-2):233–238.
- Ballmer, M., van Keken, P., and Ito, G. (2015). 7.10 - Hotspots, large igneous provinces, and melting anomalies. In Schubert, G., editor, *Treatise on Geophysics*, pages 393 – 459. Elsevier, Oxford, second edition.
- Beylkin, G. and Burridge, R. (1990). Linearized inverse scattering problems in acoustics and elasticity. *Wave motion*, 12(1):15–52.
- Bilek, S., Lay, T., and Ruff, L. (2004). Radiated seismic energy and earthquake source duration variations from teleseismic source time functions for shallow subduction zone thrust earthquakes. *Journal of Geophysical Research: Solid Earth*, 109(B9).



- Bodin, T., Sambridge, M., and Gallagher, K. (2009). A self-parametrizing partition model approach to tomographic inverse problems. *Inverse Problems*, 25(5):055009.
- Bonnier, G. (ca. 1900). *Enseignement secondaire des jeune filles, Histoire Naturelle deuxième année*. Librairie générale de l'enseignement.
- Bostock, M. (2015). 1.08 - Theory and observations - Seismology and the structure of the Earth: Teleseismic body-wave scattering and receiver-side structure. In Schubert, G., editor, *Treatise on Geophysics*, pages 253 – 275. Elsevier, Oxford, second edition.
- Bostock, M. and Rondenay, S. (1999). Migration of scattered teleseismic body waves. *Geophysical journal international*, 137(3):732–746.
- Bostock, M., Rondenay, S., and Shragge, J. (2001). Multiparameter two-dimensional inversion of scattered teleseismic body waves 1. Theory for oblique incidence. *Journal of Geophysical Research: Solid Earth*, 106(B12):30771–30782.
- Bouguer (1749). *La forme de la Terre*.
- Bowring, S., Williams, I., and Compston, W. (1989). 3.96 ga gneisses from the slave province, Northwest Territories, Canada. *Geology*, 17(11):971–975.
- Brocher, T. M., Fuis, G. S., Fisher, M. A., Plafker, G., Moses, M. J., Taber, J. J., and Christensen, N. I. (1994). Mapping the megathrust beneath the northern Gulf of Alaska using wide-angle seismic data. *Journal of Geophysical Research: Solid Earth*, 99(B6):11663–11685.
- Buck, W. (2015). 6.08 - The dynamics of continental breakup and extension. In Schubert, G., editor, *Treatise on Geophysics*, pages 325 – 379. Elsevier, Oxford, second edition.
- Buffett, B. and Becker, T. (2012). Bending stress and dissipation in subducted lithosphere. *Journal of Geophysical Research: Solid Earth*, 117(B5).
- Buffon (1749). *Histoire naturelle, générale et particulière*.
- Buland, R. and Chapman, C. (1983). The computation of seismic travel times. *Bulletin of the Seismological Society of America*, 73(5):1271–1302.
- Burdick, S., de Hoop, M., Wang, S., and van der Hilst, R. (2013). Reverse-time migration-based reflection tomography using teleseismic free surface multiples. *Geophysical Journal International*, 196(2):996–1017.
- Cardin, P. and Olson, P. (2015). 8.13 - Experiments on core dynamics. In Schubert, G., editor, *Treatise on Geophysics*, pages 317 – 339. Elsevier, Oxford, second edition.
- Castle, R. (1994). A theory of normal moveout. *Geophysics*, 59(6):983–999.

- Chapman, D. and Pollack, H. (1977). Regional geotherms and lithospheric thickness. *Geology*, 5(5):265–268.
- Charley, J., Voronin, S., Nolet, G., Loris, I., Simons, F. J., Sigloch, K., and Daubechies, I. C. (2013). Global seismic tomography with sparsity constraints: Comparison with smoothing and damping regularization. *Journal of Geophysical Research: Solid Earth*, 118(9):4887–4899.
- Cheng, C., Bodin, T., and Allen, R. M. (2016). Three-dimensional pre-stack depth migration of receiver functions with the fast marching method: a Kirchhoff approach. *Geophysical Journal International*, 205(2):819–829.
- Cheng, C., Bodin, T., Tauzin, B., and Allen, R. M. (2017). Cascadia subduction slab heterogeneity revealed by three-dimensional receiver function Kirchhoff migration. *Geophysical Research Letters*, 44(2):694–701.
- Clayton, R. and Wiggins, R. (1976). Source shape estimation and deconvolution of teleseismic bodywaves. *Geophysical Journal International*, 47(1):151–177.
- D’Alembert, J. (1747). *Recherches sur la courbe que forme une corde tendue mise en vibration*. Académie royale des sciences et belles lettres de Berlin.
- Dasgupta, R. and Hirschmann, M. (2010). The deep carbon cycle and melting in Earth’s interior. *Earth and Planetary Science Letters*, 298(1-2):1–13.
- de Kool, M., Rawlinson, N., and Sambridge, M. (2006). A practical grid-based method for tracking multiple refraction and reflection phases in three-dimensional heterogeneous media. *Geophysical Journal International*, 167(1):253–270.
- Doin, M.-P. and Henry, P. (2001). Subduction initiation and continental crust recycling: the roles of rheology and eclogitization. *Tectonophysics*, 342(1-2):163–191.
- Dueker, K. and Sheehan, A. (1997). Mantle discontinuity structure from midpoint stacks of converted P to S waves across the Yellowstone hotspot track. *Journal of Geophysical Research: Solid Earth*, 102(B4):8313–8327.
- Duffy, T. and Anderson, D. (1989). Seismic velocities in mantle minerals and the mineralogy of the upper mantle. *Journal of Geophysical Research: Solid Earth*, 94(B2):1895–1912.
- Dunkin, J. and Levin, F. (1973). Effect of normal moveout on a seismic pulse. *Geophysics*, 38(4):635–642.
- Dunn, R. (2015). 1.13 - Crust and lithospheric structure - Seismic structure of mid-ocean ridges. In Schubert, G., editor, *Treatise on Geophysics*, pages 419 – 451. Elsevier, Oxford, second edition.

- Dziewonski, A. and Anderson, D. (1981). Preliminary reference Earth model. *Physics of the earth and planetary interiors*, 25(4):297–356.
- Dziewonski, A. and Romanowicz, B. (2015). 1.01 - Deep Earth seismology: An introduction and overview. In Schubert, G., editor, *Treatise on Geophysics*, pages 1 – 28. Elsevier, Oxford, second edition.
- Elsasser, W. (1956). Hydromagnetic dynamo theory. *Reviews of modern Physics*, 28(2):135.
- Farra, V. and Vinnik, L. (2000). Upper mantle stratification by P and S receiver functions. *Geophysical Journal International*, 141(3):699–712.
- Fitterman, D. (2015). 11.10 - Tools and techniques: Active-source electromagnetic methods. In Schubert, G., editor, *Treatise on Geophysics*, pages 295 – 333. Elsevier, Oxford, second edition.
- Fukao, Y. and Obayashi, M. (2015). 1.20 - Deep Earth structure - Subduction zone structure in the mantle transition zone. In Schubert, G., editor, *Treatise on Geophysics*, pages 641 – 654. Elsevier, Oxford, second edition.
- Gilbert, W. (1600). *Magno magnetes tellure*.
- Gray, S. (1986). Efficient traveltimes calculations for Kirchhoff migration. *Geophysics*, 51(8):1685–1688.
- Gutenberg, B. (1912). Über die Konstitution des Erdinnern, erschlossen aus Erdbebenbeobachtungen. *Phys. Z*, 14:1217–1218.
- Hagedoorn, J. (1954). A process of seismic reflection interpretation. *Geophysical Prospecting*, 2(2):85–127.
- Halpaap, F., Rondenay, S., Liu, Q., and Millet, F. (2019). Toward waveform-based characterization of slab earthquakes. *PhD. Thesis*.
- Heiskanen, V. (1924). *Untersuchungen über Schwerkraft und Isostasie*.
- Helmstetter, A. and Sornette, D. (2003). Predictability in the epidemic-type aftershock sequence model of interacting triggered seismicity. *Journal of Geophysical Research: Solid Earth*, 108(B10).
- Hess, H. (1962). History of ocean basins. *Petrologic studies*.
- Houston, H. (2001). Influence of depth, focal mechanism, and tectonic setting on the shape and duration of earthquake source time functions. *Journal of Geophysical Research: Solid Earth*, 106(B6):11137–11150.

- Hudson, J. and Heritage, J. (1981). The use of the Born approximation in seismic scattering problems. *Geophysical Journal International*, 66(1):221–240.
- Huygens, C. (1690). *Traité de la Lumière*.
- Jamtveit, B., Bucher-Nurminen, K., and Austrheim, H. (1990). Fluid controlled eclogitization of granulites in deep crustal shear zones, Bergen arcs, Western Norway. *Contributions to Mineralogy and Petrology*, 104(2):184–193.
- Jeffreys, H. (1926). The rigidity of the Earth’s central core. *Geophysical Supplements to the Monthly Notices of the Royal Astronomical Society*, 1(7):371–383.
- Jekeli, C. (2015). 3.02 - Potential theory and the static gravity field of the Earth. In Schubert, G., editor, *Treatise on Geophysics*, pages 9 – 35. Elsevier, Oxford, second edition.
- Kennett, B. and Engdahl, E. (1991). Traveltimes for global earthquake location and phase identification. *Geophysical Journal International*, 105(2):429–465.
- Kennett, B., Engdahl, E., and Buland, R. (1995). Constraints on seismic velocities in the Earth from traveltimes. *Geophysical Journal International*, 122(1):108–124.
- Kepler, J. (1609). *Astronomia nova*.
- Kerrick, D. and Connolly, J. (2001). Metamorphic devolatilization of subducted oceanic metabasalts: implications for seismicity, arc magmatism and volatile recycling. *Earth and Planetary Science Letters*, 189(1-2):19–29.
- Kim, Y., Abers, G. A., Li, J., Christensen, D., Calkins, J., and Rondenay, S. (2014). Alaska megathrust 2: Imaging the megathrust zone and Yakutat/Pacific plate interface in the Alaska subduction zone. *Journal of Geophysical Research: Solid Earth*, 119(3):1924–1941.
- Kircher (1664). *Mundus subterraneus*.
- Kissling, E., Husen, S., and Haslinger, F. (2001). Model parametrization in seismic tomography: a choice of consequence for the solution quality. *Physics of the Earth and Planetary Interiors*, 123(2-4):89–101.
- Knapp, R. and Steeples, D. (1986). High-resolution common-depth-point reflection profiling: Field acquisition parameter design. *Geophysics*, 51(2):283–294.
- Lamb, S. and Davis, P. (2003). Cenozoic climate change as a possible cause for the rise of the Andes. *Nature*, 425(6960):792.
- Lamé, G. (1852). *Leçons sur la théorie mathématique de l’élasticité des corps solides*.

- Langston, C. (1979). Structure under Mount Rainier, Washington, inferred from teleseismic body waves. *Journal of Geophysical Research: Solid Earth*, 84(B9):4749–4762.
- Lankston, R. (1990). High-resolution refraction seismic data acquisition and interpretation. In *Geotechnical and Environmental Geophysics: Volume I: Review and Tutorial*, pages 45–74.
- Lawrence, J. and Shearer, P. (2006). A global study of transition zone thickness using receiver functions. *Journal of Geophysical Research: Solid Earth*, 111(B6).
- Le Pichon, X. (1968). Sea-floor spreading and continental drift. *Journal of Geophysical Research*, 73(12):3661–3697.
- Lehmann, I. (1936). P. *Bur. Centr. Seism. Internat. Serie A*, 14:87–115.
- Levander, A., Zelt, C., and Symes, W. (2007). 1.15 - Crust and lithospheric structure - Active source studies of crust and lithospheric structure. In Schubert, G., editor, *Treatise on Geophysics*, pages 479 – 511. Elsevier, Oxford, second edition.
- Ligorria, J. and Ammon, C. (1999). Iterative deconvolution and receiver-function estimation. *Bulletin of the seismological Society of America*, 89(5):1395–1400.
- Madariaga, R. (2015). 4.02 - Seismic source theory. In Schubert, G., editor, *Treatise on Geophysics*, pages 51 – 71. Elsevier, Oxford, second edition.
- Marsh, B. (2015). 6.07 - Magmatism, magma, and magma chambers. In Schubert, G., editor, *Treatise on Geophysics*, pages 273 – 323. Elsevier, Oxford, second edition.
- Martin-Short, R., Allen, R., Bastow, I., Porritt, R., and Miller, M. (2018). Seismic imaging of the Alaska subduction zone: Implications for slab geometry and volcanism. *Geochemistry, Geophysics, Geosystems*, 19(11):4541–4560.
- Mayne, W. (1962). Common reflection point horizontal data stacking techniques. *Geophysics*, 27(6):927–938.
- McKenzie, D. and Parker, R. (1967). The North Pacific: an example of tectonics on a sphere. *Nature*, 216(5122):1276.
- Miles, J. (1960). Scattering of elastic waves by small inhomogeneities. *Geophysics*, 25(3):642–648.
- Millet, F., Bodin, T., and Rondenay, S. (2019). Multimode 3-D Kirchhoff migration of receiver function at continental scale. *Journal of Geophysical Research*, pages –.
- Mohorovičić, A. (1909). Das Beben vom 8. x. 1909. *Jahrb Meteorol Obs Zagreb*, 9:1–63.
- Mooney, W. (2015). 1.11 - Crust and lithospheric structure - Global crustal structure. In

- Schubert, G., editor, *Treatise on Geophysics*, pages 339 – 390. Elsevier, Oxford, second edition.
- Morgan, J. (1968). Rises, trenches, great faults, and crustal blocks. *Journal of Geophysical Research*, 73(6):1959–1982.
- Newton, I. (1687). *Philosophiae naturalis principia mathematica*.
- Oldham, R. D. (1906). The constitution of the interior of the Earth, as revealed by earthquakes. *Quarterly Journal of the Geological Society*, 62(1-4):456–475.
- Owens, T. J., Zandt, G., and Taylor, S. R. (1984). Seismic evidence for an ancient rift beneath the Cumberland Plateau, Tennessee: A detailed analysis of broadband teleseismic P waveforms. *Journal of Geophysical Research: Solid Earth*, 89(B9):7783–7795.
- Panet, I., Mikhailov, V., Diament, M., Pollitz, F., King, G., De Viron, O., Holschneider, M., Biancale, R., and Lemoine, J.-M. (2007). Coseismic and post-seismic signatures of the Sumatra 2004 december and 2005 march earthquakes in GRACE satellite gravity. *Geophysical Journal International*, 171(1):177–190.
- Pavlis, G. (2011). Three-dimensional, wavefield imaging of broadband seismic array data. *Computers & geosciences*, 37(8):1054–1066.
- Pearce, F., Rondenay, S., Sachpazi, M., Charalampakis, M., and Royden, L. (2012). Seismic investigation of the transition from continental to oceanic subduction along the western Hellenic Subduction Zone. *Journal of Geophysical Research: Solid Earth*, 117(B7).
- Phinney, R. (1964). Structure of the Earth’s crust from spectral behavior of long-period body waves. *Journal of Geophysical Research*, 69(14):2997–3017.
- Plato (n.d.). *Phaedo*.
- Poisson, S. (1829). *Mémoire sur l’équilibre et le mouvement des corps élastiques*. Mémoires de l’Académie Royale des Sciences de l’Institut de France.
- Pratt, J. (1855). I. On the attraction of the Himalaya Mountains, and of the elevated regions beyond them, upon the plumb-line in India. *Philosophical Transactions of the Royal Society of London*, (145):53–100.
- Priestley, K., Jackson, J., and McKenzie, D. (2008). Lithospheric structure and deep earthquakes beneath India, the Himalaya and southern Tibet. *Geophysical Journal International*, 172(1):345–362.
- Ravaut, C., Operto, S., Improta, L., Virieux, J., Herrero, A., and Dell’Aversana, P. (2004). Multiscale imaging of complex structures from multifold wide-aperture seismic data by

- frequency-domain full-waveform tomography: Application to a thrust belt. *Geophysical Journal International*, 159(3):1032–1056.
- Rawlinson, N., Houseman, G. A., and Collins, C. D. (2001). Inversion of seismic refraction and wide-angle reflection traveltimes for three-dimensional layered crustal structure. *Geophysical Journal International*, 145(2):381–400.
- Rawlinson, N. and Sambridge, M. (2004). Multiple reflection and transmission phases in complex layered media using a multistage fast marching method. *Geophysics*, 69(5):1338–1350.
- Rondenay, S. (2006). Multi-disciplinary experiments for dynamic understanding of subduction under the Aegean sea. *International Federation of Digital Seismograph Networks*, Dataset/Seismic Network.
- Rondenay, S. (2009). Upper mantle imaging with array recordings of converted and scattered teleseismic waves. *Surveys in geophysics*, 30(4-5):377–405.
- Rondenay, S., Bostock, M., and Fischer, K. (2005). Multichannel inversion of scattered teleseismic body waves: practical considerations and applicability. *Geophysical monograph-american geophysical union*, 157:187.
- Rondenay, S., Bostock, M., and Shragge, J. (2001). Multiparameter two-dimensional inversion of scattered teleseismic body waves 3. Application to the Cascadia 1993 data set. *Journal of Geophysical Research: Solid Earth*, 106(B12):30795–30807.
- Rondenay, S., Montesi, L. G., and Abers, G. A. (2010). New geophysical insight into the origin of the Denali volcanic gap. *Geophysical Journal International*, 182(2):613–630.
- Rondenay, S., Spieker, K., Sawade, L., Halpaap, F., and Farestveit, M. (2016). GLImER: A new global database of teleseismic receiver functions for imaging Earth structure. *Seismological Research Letters*, 88(1):39–48.
- Satake, K. (2015). 4.19 - Tsunamis. In Schubert, G., editor, *Treatise on Geophysics*, pages 477 – 504. Elsevier, Oxford, second edition.
- Savage, J. and Prescott, W. (1978). Asthenosphere readjustment and the earthquake cycle. *Journal of Geophysical Research: Solid Earth*, 83(B7):3369–3376.
- Searle, M. (2015). 6.11 - Mountain Building, tectonic evolution, rheology, and crustal flow in the Himalaya, Karakoram, and Tibet. In Schubert, G., editor, *Treatise on Geophysics*, pages 469 – 511. Elsevier, Oxford, second edition.
- Shang, X., de Hoop, M. V., and van der Hilst, R. D. (2012). Beyond receiver functions: Passive source reverse time migration and inverse scattering of converted waves. *Geophysical Research Letters*, 39(15).

- Shang, X., de Hoop, M. V., and van der Hilst, R. D. (2017). Common conversion point stacking of receiver functions versus passive-source reverse time migration and wavefield regularization. *Geophysical Journal International*, 209(2):923–934.
- Shibutani, T., Sambridge, M., and Kennett, B. (1996). Genetic algorithm inversion for receiver functions with application to crust and uppermost mantle structure beneath eastern Australia. *Geophysical Research Letters*, 23(14):1829–1832.
- Singh, S., Chauhan, A., Calvert, A., Hananto, N., Ghosal, D., Rai, A., and Carton, H. (2012). Seismic evidence of bending and unbending of subducting oceanic crust and the presence of mantle megathrust in the 2004 Great Sumatra earthquake rupture zone. *Earth and Planetary Science Letters*, 321:166–176.
- Sornette, D. and Pisarenko, V. (2003). Fractal plate tectonics. *Geophysical research letters*, 30(3).
- Speranza, F., Minelli, L., Pignatelli, A., and Chiappini, M. (2012). The Ionian Sea: The oldest in situ ocean fragment of the world? *Journal of Geophysical Research: Solid Earth*, 117(B12).
- Spieker, K. (2017). Imaging of crust and mantle using receiver function analysis. *PhD Thesis*.
- Stein, J. (2015). 1.02 - Theory and observations - Instrumentation for global and regional seismology. In Schubert, G., editor, *Treatise on Geophysics*, pages 29 – 78. Elsevier, Oxford, second edition.
- Suess, E. (1885). *Das Antlitz der Erde*.
- Tape, C., Christensen, D., Moore-Driskell, M. M., Sweet, J., and Smith, K. (2017). Southern Alaska lithosphere and mantle observation network (SALMON): A seismic experiment covering the active arc by road, boat, plane, and helicopter. *Seismological Research Letters*, 88(4):1185–1202.
- Tapley, B., Bettadpur, S., Watkins, M., and Reigber, C. (2004). The gravity recovery and climate experiment: Mission overview and early results. *Geophysical Research Letters*, 31(9).
- Tarantola, A. (1984). Inversion of seismic reflection data in the acoustic approximation. *Geophysics*, 49(8):1259–1266.
- Tauzin, B., Bodin, T., Debayle, E., Perrillat, J.-P., and Reynard, B. (2016). Multi-mode conversion imaging of the subducted Gorda and Juan de Fuca plates below the North American continent. *Earth and Planetary Science Letters*, 440:135–146.
- Thomas, C., Weber, M., Wicks, C., and Scherbaum, F. (1999). Small scatterers in the



- lower mantle observed at German broadband arrays. *Journal of Geophysical Research: Solid Earth*, 104(B7):15073–15088.
- Thurber, C. and Ritsema, J. (2015). 1.10 - Theory and observations - Seismic tomography and inverse methods. In Schubert, G., editor, *Treatise on Geophysics*, pages 307 – 337. Elsevier, Oxford, second edition.
- Van Keken, P. E., Kiefer, B., and Peacock, S. (2002). High-resolution models of subduction zones: Implications for mineral dehydration reactions and the transport of water into the deep mantle. *Geochemistry, Geophysics, Geosystems*, 3(10):1–of.
- Vidale, J. and Hedlin, M. (1998). Evidence for partial melt at the core-mantle boundary north of Tonga from the strong scattering of seismic waves. *Nature*, 391(6668):682.
- Vinnik, L. (1977). Detection of waves converted from P to SV in the mantle. *Physics of the Earth and planetary interiors*, 15(1):39–45.
- Virieux, J. and Operto, S. (2009). An overview of full-waveform inversion in exploration geophysics. *Geophysics*, 74(6):WCC1–WCC26.
- von Rebeur-Paschwitz, E. (1889). The earthquake of Tokio, April 18, 1889. *Nature*, (40):294–295.
- Wada, I. and King, S. (2015). 7.09 - Dynamics of subducting slabs: Numerical modeling and constraints from seismology, geoid, topography, geochemistry, and petrology. In Schubert, G., editor, *Treatise on Geophysics*, pages 339 – 391. Elsevier, Oxford, second edition.
- Wang, Z. and Zhao, D. (2005). Seismic imaging of the entire arc of Tohoku and Hokkaido in Japan using P-wave, S-wave and sP depth-phase data. *Physics of the Earth and Planetary Interiors*, 152(3):144–162.
- Wegener, A. (1929). Die Entstehung der Kontinente und Ozeane. *Ges., Braunschweig*.
- Wessel, P. and Müller, R. (2015). 6.02 - Plate tectonics. In Schubert, G., editor, *Treatise on Geophysics*, pages 45 – 93. Elsevier, Oxford, second edition.
- Wiechert, E. (1897). Über die Massenvertheilung im Innern der Erde. *Nachrichten von der Königlichen Gesellschaft der Wissenschaften zu Göttingen, Mathematisch-physikalische Klasse*, 1897:221–243.
- Wold, S., Esbensen, K., and Geladi, P. (1987). Principal component analysis. *Chemometrics and intelligent laboratory systems*, 2(1-3):37–52.
- Worzewski, T., Jegen, M., Kopp, H., Brasse, H., and Castillo, W. (2011). Magnetotelluric image of the fluid cycle in the costa rican subduction zone. *Nature Geoscience*, 4(2):108.

- Wu, R. and Aki, K. (1985). Scattering characteristics of elastic waves by an elastic heterogeneity. *Geophysics*, 50(4):582–595.
- Xu, W., Lithgow-Bertelloni, C., Stixrude, L., and Ritsema, J. (2008). The effect of bulk composition and temperature on mantle seismic structure. *Earth and Planetary Science Letters*, 275(1-2):70–79.
- Yilmaz, O. (2001). *Seismic data analysis: Processing, inversion, and interpretation of seismic data*. Society of exploration geophysicists.
- Zelt, C. A., Sain, K., Naumenko, J. V., and Sawyer, D. S. (2003). Assessment of crustal velocity models using seismic refraction and reflection tomography. *Geophysical Journal International*, 153(3):609–626.
- Zhu, L. and Helmberger, D. (1996). Advancement in source estimation techniques using broadband regional seismograms. *Bulletin of the Seismological Society of America*, 86(5):1634–1641.



# Multi-Mode 3D Kirchhoff Migration of Receiver Functions at Continental Scale

Published in *Journal of Geophysical Research*

Florian Millet<sup>1,2</sup>, Thomas Bodin<sup>1</sup>, Stéphane Rondenay<sup>2</sup>

[1] Laboratoire de Géologie de Lyon, UMR 5276, Université de Lyon, Villeurbanne, France

[2] Department of Earth Science, University of Bergen, Bergen, Norway

## Keypoints

- We develop a fully 3D teleseismic scattered waves imaging method that uses fast 3D travel-time calculations.
- Our method accounts for free-surface multiple scattering modes and polarity reversals for non-horizontal interfaces.
- Application of our method to field data in the Hellenic Subduction Zone yields images that are coherent with previous 2D imaging results.

## Abstract

Receiver Function analysis is widely used to image sharp structures in the Earth, such as the Moho or transition zone discontinuities. Standard procedures either rely on the

assumption that underlying discontinuities are horizontal (Common Conversion Point stacking), or are computationally expensive and usually limited to 2D geometries (Reverse Time Migration, Generalized Radon Transform). Here, we develop a teleseismic imaging method that uses fast 3D travel-time calculations with minimal assumption about the underlying structure. This allows us to achieve high computational efficiency without limiting ourselves to 1D or 2D geometries. In our method, we apply acoustic Kirchhoff migration to transmitted and reflected teleseismic waves (i.e. receiver functions). The approach expands on the work of [Cheng et al. \(2016\)](#) to account for free surface multiples. We use an Eikonal solver based on the fast marching method to compute travel times for all scattered phases. 3D scattering patterns are computed to correct the amplitudes and polarities of the three component input signals. We consider three different stacking methods (linear, phase weighted and 2<sup>nd</sup> root) to enhance the structures that are most coherent across scattering modes, and find that 2<sup>nd</sup> root stack is the most effective. Results from synthetic tests show that our imaging principle can recover scattering structures accurately with minimal artifacts. Application to real data from the MEDUSA experiment in the Hellenic subduction zone yields images that are similar to those obtained by 2D GRT migration at no additional computational cost, further supporting the robustness of our approach.

## 1 Introduction

Scattered phases in the coda of main teleseismic body-wave phases have been used to map discontinuities at various scales in the Earth. As opposed to direct phases that are mainly sensitive to volumetric heterogeneities, the scattered wavefield contains information about sharp structures that standard travel-time or surface wave tomography cannot resolve ([Langston, 1979](#)). The large amount of computations needed to exploit the scattered wavefield has limited its first applications to small-scale studies. However, there has been a growing interest to exploit the scattered wavefield at larger scale because the scattering structures are associated with variations in composition, mineralogical or water content that are often linked to global scale phenomena. Exploiting this data in the form of receiver functions sheds light on open research topics such as the dehydration of slabs ([Tauzin et al., 2017](#)), deep phase transitions in secondary minerals ([Cottaar and Deuss, 2016](#)) and the water content of the mantle transition zone ([Zheng et al., 2007](#)).

Receiver Function (RF) analysis extracts structural information from body-wave seismograms by removing the source component to retrieve the P-to-S and S-to-P converted waves (see, e.g., [Langston, 1979](#); [Bostock and Rondenay, 1999](#); [Park and Levin, 2000](#);

Levander and Miller, 2012). It is based on the separation between the signal of the incident wave and that of the scattered wavefield in seismograms recorded at teleseismic distances (Phinney, 1964; Langston, 1979). In the case of first order forward P-to-S scattering at a horizontal interface, the incident wave is the direct P-wave and the scattered energy corresponds to an  $S_V$ -wave that is mostly recorded on the radial component of the seismograms. The data is selected for epicentral distances ranging from  $30^\circ$  to  $95^\circ$  to avoid core phases and triplications from the mantle transition zone. The simplest way to exploit this P-to-S data is to deconvolve the vertical component from the radial. This assumes that the signal on the vertical component corresponds to the P-wave and that it represents the source time function. This deconvolution removes the complexity associated with the source time function from the S-waves on the radial component, and thus produces a waveform that can be interpreted in terms of scattering structure. More advanced deconvolution methods optimize the source and noise estimates on three components for station arrays (Chen et al., 2010). Estimating a source time function in 3D allows to get three component RFs that contain more information about the scattering structure than simple vertically-deconvolved radial RFs.

Deconvolved teleseismic waveforms can be interpreted with Common Conversion Point (CCP) stacking methods, which are a useful tool to obtain first-order images of the structure in the crust and upper mantle below an array of seismic stations (Tessmer and Behle, 1988; Dueker and Sheehan, 1997). By using a reference 1D velocity model and applying lateral move-out corrections, these methods allow to project stacked scattering potential back at depth. These methods have been successfully applied to large datasets such as USArray in North America (Levander and Miller, 2012) and J-array/Hi-net in Japan (Yamauchi et al., 2003). Many of these CCP imaging methods only use the radial component of the RF as it is faster and easier to interpret. Tonegawa et al. (2008) showed that the transverse component CCPs can also provide information about dipping reflectors. However, in the case of dipping structures, the polarity of S-waves in the transverse component varies with back-azimuth, and caution must be taken when stacking. This usually means that analysts restrain their datasets to convenient back-azimuth directions where polarities are coherent.

CCP methods rely on the fundamental assumption that imaged structures are horizontal, which allows for fast move-out corrections and stacking. This assumption is clearly not valid in many geological settings such as subduction zones or orogens. Some approaches, such as the one-way wave equation migration (Chen et al., 2005), include 3D filtering to effectively take lateral heterogeneities into account. More complex methods such as Reverse Time Migration (RTM, Burdick et al., 2013) rely on an inversion that requires the

numerical computation of full scattered waveforms for every source-receiver pair in a complex reference velocity model. Generalized Radon Transform (GRT) migration includes amplitude-sensitive weights that recover 2D or 3D velocity anomalies (see, e.g., [Bostock et al., 2001](#); [Pavlis, 2011](#)). These more sophisticated approaches treat the full scattered wavefield, and hence use all three components of the RF. They are more accurate but also computationally more expensive and require higher data coverage than CCP. They are therefore usually limited to local-scale applications on dense linear arrays ([Rondenay, 2009](#)). As many geological settings tend to exhibit nearly 2D geometries, imaging in 2D is often sufficient to resolve subsurface structure accurately (see, e.g., [Pearce et al., 2012](#)). These methods have been applied successfully in complex tectonic settings such as the Tibetan plateau ([Shang et al., 2017](#)) or Cascadia subduction zone ([Rondenay et al., 2001](#); [Abers et al., 2009](#)). An extensive review of scattered body waves imaging techniques can be found in [Rondenay \(2009\)](#).

Until the last decade, the cost associated with 3D migration was too prohibitive to develop fully 3D imaging methods for scattered body waves. In recent years, however, the advent of new fast computational tools gave rise to a new generation of methods for imaging laterally varying structures over a range of scales. For example, a fully 3D P-wave coda waveform inversion has been proposed by [Frederiksen and Revenaugh \(2004\)](#) and is a promising tool for local to regional studies, but remains computationally expensive. 2D and 3D CCP approaches have also been devised to image laterally varying media at large scales and have been successfully applied to several regions in North America and Asia ([Tauzin et al., 2016](#); [Rondenay et al., 2017](#)). Recently, [Pavlis \(2011\)](#) extended the GRT imaging principle to image 3D structures. [Wang and Pavlis \(2016\)](#) used a plane wave approximation and performed ray-tracing in a radially symmetric 1D reference Earth model. This approach is certainly valid for looking at structures that are fairly continuous laterally, such as the mantle transition zone. However, it can be inadequate in regions where there are strong lateral variations in background seismic properties, such as subduction zones, where local focussing and defocusing effects can become predominant.

[Cheng et al. \(2016\)](#) took another approach and devised a 3D migration method based on the Kirchhoff imaging principle, a well established method in exploration geophysics ([Claerbout, 1985](#)). It has been adapted for use with teleseismic data in the past decades ([Ryberg and Weber, 2000](#)), and is the basis for the Regularized Kirchhoff migration ([Wilson and Aster, 2005](#)) and the GRT migrations ([Bostock et al., 2001](#); [Liu and Levander, 2013](#)). In the data space (i.e., the time domain), teleseismic Kirchhoff imaging stacks the data along diffraction hyperbolae corresponding to an ensemble of arrivals consistent with a scattering point. In the model space (i.e., the depth domain), this is equivalent to

mapping a given observed phase to an ensemble of grid points that predict the arrival time of that phase, i.e. a migration isochron. By migrating all the waveforms along isochrons, and stacking over multiples source-receiver pairs, the structure can be recovered. However, one of the drawbacks of this method is that the data coverage needs to be dense enough for the migration isochrons to stack up constructively.

What makes Kirchhoff migration attractive is that only the travel times of the scattered phases need to be estimated, instead of the complex scattered wavefield required by other methods (RTM, GRT). The advantage is that the travel times can be quickly computed by solving the Eikonal equation. We compute them using the fast marching approach with the FM3D software package developed by [de Kool et al. \(2006\)](#). [Cheng et al. \(2016\)](#) showed that a fully 3D Kirchhoff prestack migration is computationally tractable. Their method was tested using 2.5D synthetic data obtained from ray tracing ([Raysum, Frederiksen and Bostock, 2000](#)), as well as data from the Cascadia93, Mendocino and USArray experiments. A similar method based on sensitivity kernels for P-to-S and S-to-P conversions has been devised by [Hansen and Schmandt \(2017\)](#) and tested using 2D synthetics obtained from spectral element simulations ([Specfem2D, Tromp et al., 2008](#)). Both methods have the same order of computational cost as 2D GRT, and can image laterally varying structures such as subducting slabs given a dense ray coverage of the region of interest.

Here we extend the work of [Cheng et al. \(2016\)](#) on Kirchhoff prestack depth migration of teleseismic receiver functions with amplitude corrections from scattering patterns. We propose three improvements to this work. First, we migrate all three components of the recorded wavefield to enhance the coherence of the stack. Second, we incorporate the free-surface multiples in the migration algorithm. One of the problems that was highlighted in [Cheng et al. \(2016\)](#) is the presence of artifacts in the final image due to free surface multiples. These spurious signals might be misinterpreted as direct P-to-S conversions at the Lithosphere - Asthenosphere Boundary (LAB). Here we address this problem by migrating the data a first time assuming that the arrivals correspond to a direct P-to-S conversion, and three more times assuming the arrivals correspond to free surface multiples (i.e., surface back-scattering). We use the fast marching method (FM3D software) to compute efficiently the travel-times for any given reflected and transmitted phases combination. Third, we use fully 3D scattering patterns to correctly treat all components ( $P, S_V, S_H$ ) that are observed at the surface. Once the travel times are computed for all the scattered phases, one needs to account for the amplitude and polarity of these phases, which can vary in the case of non-horizontal structures ([Tonegawa et al., 2008](#); [Cheng et al., 2016](#)). The polarities and amplitudes are corrected using 3D scattering patterns as



those described in [Beylkin and Burrige \(1990\)](#). The scattering patterns can be seen as simulating the physics of elastic wave propagation without having to compute expensive scattered wavefields.

Similar to approaches discussed by [Rondenay \(2009\)](#), our new method initially generates one image per scattering mode, so four images in total. A final migrated image is then built by stacking these individual scattering mode images. We test three stacking techniques to enhance the structure that is most coherent between the forward and back-scattered modes. We first try a linear stack between the four modes. Then we implement a phase-weighted stack, which acts as a phase coherence filter. Lastly we implement a 2<sup>nd</sup> root stack that acts as an amplitude coherence filter.

In the following sections, we derive our improved 3D Kirchhoff imaging approach and discuss its ability to resolve complex 2D and 3D structures. Here, we only describe the method for use with the P-to-S RF, but one could devise a similar method for use with S-to-P RF. After describing in detail the method in Section 2, we test it in Section 3 by conducting a series of synthetic tests using the Raysum software ([Frederiksen and Bostock, 2000](#)) in both artificially challenging and realistic scenarios. We show that a typical subduction zone structure can be retrieved. Finally, we test our method on a field dataset from Greece in Section 4.

## 2 Methodology

### 2.1 Three component Receiver Functions

The radial, transverse and vertical components of seismograms and RFs record different yet coherent responses to discontinuities in the Earth, and therefore provide complementary information about the structure of the Earth (see, e.g., [Tonegawa et al., 2008](#)). For horizontal interfaces and isotropic media, we know that the P-to-S conversions for a near vertical incidence are mostly recorded on the radial component. As RFs are usually computed for near vertical incidences of teleseismic waves in isotropic horizontally layer media, traditional studies consider only the radial component in the deconvolution. However, in the case of dipping interfaces, this energy is partitioned between the radial and transverse horizontal components. Moreover, because teleseismic arrivals are never truly vertical, some of the P-to-S energy is recorded on the vertical component and some of the P-to-P and S-to-P conversions are recorded on the horizontal components. These effects are even stronger in the case of large volumetric velocity heterogeneities. In this study, we use three component teleseismic RFs as we aim to properly account for effects of dipping

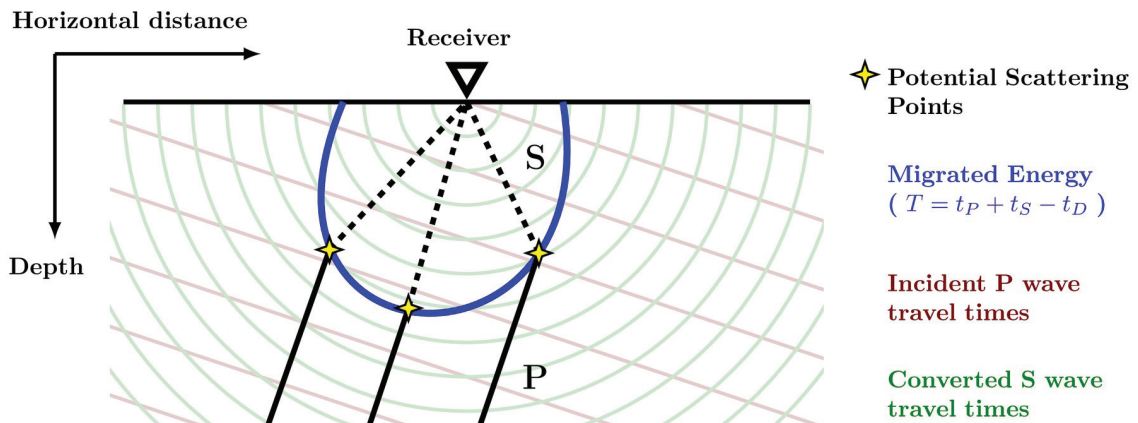


**Figure 1** – Schematic illustration of the 3D Kirchhoff prestack imaging principle along a 2D profile. The incoming P-waves (solid lines, red background isochrone lines) and scattered S-waves (dashed lines, green background isochrone lines) arrival times are computed at each grid point in the 3D model box and the energy is migrated (blue curve) along a differential isochron that corresponds to the time delay between the incident and scattered wave – i.e., the difference in travel time  $T$  between the direct wave ( $t_D$ ) and the P-wave to the scatterer ( $t_P$ ) added to the S-wave to the receiver ( $t_S$ ). This isochron represents all the points in depth in the 3D model space that could account for scattered energy seen at a given time on the RF. In the 3D case, the isochron extends as an ellipsoid whose shape depends on the source-receiver geometry and the reference velocity model.

interfaces and lateral variations in elastic properties.

For the synthetic cases presented below, we directly migrate the 3 component waveforms obtained with the Raysum calculations as they already correspond to the structural impulse response convolved with a Gaussian source time function. For the field data, we use a multichannel preprocessing approach similar to the one described in Rondenay (2009) to extract the scattered wavefield for each source. The three component RFs at all the stations for each source are obtained by (1) estimating the source time function through Principal Component Analysis (PCA) on the  $P$  components of the  $P - S_V - S_H$  rotated seismograms, (2) removing the source waveform  $\bar{P}$  from the records to obtain the estimated three component scattered wavefields  $P' - S_V - S_H$  where  $P' = P - \bar{P}$  and (3) deconvolving the estimated scattered wavefields by the estimated source waveform in the frequency domain using a regularized least-square inversion with optimal damping parameter for each seismogram and each component (Pearce et al., 2012; Bostock and Rondenay, 1999).

## 2.2 Kirchhoff prestack depth migration

In order to exploit these three-component RF signals, we implement a prestack migration that allows to naturally take 3D effects into account. Kirchhoff prestack depth migration is a technique that was developed in exploration geophysics and that maps scattered phases observed on seismograms located at the surface back at depth to scattering points (see, e.g., [Ylmaz, 2001](#)). Using a reference velocity model, the energy is propagated back in depth to all the points in 3D that would provide the same observed arrival. By doing so, we effectively treat each grid point as a potential scatterer and smear the energy of a given observed arrival along a migration isochron in the depth domain. The energy at depth for each observed trace is then stacked after migration. Alternatively, in the data space, this corresponds to finding the scattering points or interfaces by stacking the energy peaks along coherent diffraction hyperbolae. A visual representation of the Kirchhoff imaging principle in the model space is shown in figure 1.

For two observed phases on two different waveforms corresponding to the same scattering point (i.e. on the same diffraction hyperbola), the depth-migrated isochrons will intersect at the actual scattering point and stack up constructively. Extending this observation to all source-receiver couples and all scattering points, one can see that this stacking in the depth domain will focus the energy from the isochrons to the actual scattering features. However, for this method to work correctly, a high density of data is required. For teleseismic data, an ideal array would have an inter-station spacing of less than half the depth of the shallowest structure that we are interested in imaging ([Rondenay et al., 2005](#)). As summarized in [Rondenay \(2009\)](#), the imaging principle for the teleseismic Kirchhoff prestack depth migration can be written in general terms as:

$$f(x) = \iint \vec{w}(x, r) \cdot \Delta \vec{u}(r, t = T(r, x)) dr \quad (1)$$

where  $f(x)$  is the scattering potential at a given image point  $x$  in depth,  $r$  describes the source-receiver geometry on the region of interest, the weights  $\vec{w}(x, r)$  are linked to the treatment of the wavefield's amplitude and polarity during the migration,  $\Delta \vec{u}$  is the three-dimensional scattered wavefield obtained through the multichannel preprocessing approach described in previous section with a  $i\omega$  wavelet shaping factor applied in the frequency domain, and  $T(r, x)$  represents the arrival times associated with a given (source - scatterer - receiver) geometry estimated in a reference 3D velocity model. For the forward P-to-S scattering, for example, we have  $T(r, x) = t_P + t_S - t_D$ , where  $t_P$ ,  $t_S$  and  $t_D$  are travel times computed in the reference 3D velocity model.  $t_P$  is the travel time for the P-wave traveling from the source to the scattering point,  $t_S$  for the S-wave traveling

from the scattering point to the receiver, and  $t_D$  for the direct P-wave traveling from the source to the receiver. We use the fast marching method (FM3D, [de Kool et al., 2006](#)) to compute these travel time fields. FM3D solves the Eikonal equation in our 3D space after initializing the teleseismic arrival times at the border of the domain. It yields the travel-time fields for all the scattered phases, including the free surface multiples, by propagating the wavefield a first time upwards (direct) and a second time downwards (reflected). It uses this multi-stage approach to obtain all the travel times with only one computation. This makes this approach computationally efficient. The integration is carried out over all the sources and receivers.

The wavelet shaping factor ( $i\omega$ ) must be applied to the scattered wavefield data  $\Delta\vec{u}$  to account for the 3D propagation of the wavefield in the Kirchhoff migration theory ([Ylmaz, 2001](#)). This means that instead of migrating the proper Receiver Function, we migrate its derivative. More precisely, the  $i\omega$  factor transforms a Gaussian pulse on the Receiver Function into two consecutive pulses, the second one having the same polarity as the Gaussian and the first one the opposite polarity. These two pulses are at twice the frequency from the original signal and shifted by a half wavelength of the original signal, to earlier times for the first pulse and later times for the second one. This allows for the stacking to occur exactly on the interface where the second pulse is migrated and to reduce the noise above the interface through destructive interference with the first pulse.

The weights  $\vec{w}(x, r)$  account for the amplitude of the migrated waveforms. They are a linear combination of the geometrical spreading, the scattering patterns and the projection of the incoming polarization vector of the scattered phase on the (R,T,Z) reference frame at the station. Note that the reference frame changes for each event. The geometrical spreading accounts for amplitude reduction due to 3D wave propagation from the scattering point to the receiver. The scattering patterns can be seen as simulating the physics of elastic wave propagation (e.g. amplitude of a P-to-S conversion) without having to numerically compute the full wavefield. These weights allow us to model the amplitudes of the scattered wavefield, and to take into account amplitude information in the observed data. The application of the  $i\omega$  shaping factor does not alter the amplitudes as it amounts simply to a derivation of the signal (i.e., a linear operation).

### 2.3 Accounting for scattering theory

[Cheng et al. \(2016\)](#) showed that, in order to image dipping discontinuities for any incoming slowness and back-azimuth, the polarities and amplitudes of the RF can be corrected by using scattering patterns. However, the authors used the scattering patterns from

Rondenay (2009), which are 3D scattering patterns projected in 2D. This approximation is valid for  $S_V$  scattered waves that are polarized in the plane defined by the source, the scattering point and the receiver (hereafter called the scattering plane), and is applicable to the case of forward P-to-S scattering. However, in order to treat the  $S_H$  waves generated by scattering of free surface reverberations, we need to use fully 3D scattering patterns.

Scattering patterns describe the amplitude and orientation of the polarization vector of the wave scattered at any point  $x$  in our 3D model space, for a given source-receiver geometry  $r$ . That is, for a given angle between the incoming and scattered wave, they give the amplitude and sign of the scattered phase. We compute this value for every  $r$  geometry and each possible scattering point  $x$  in our 3D model. The projection of the estimated polarization vector from  $x$  to the station on the (R,T,Z) reference frame at the station is a measure of how much a scatterer at  $x$  would contribute to each component of the RF. Applying the dot product between this resulting vector and the observed wavefield  $\Delta\vec{u}(r, t = T(r, x))$  tells us how much energy should be migrated to  $x$ .

As suggested in Tonegawa et al. (2008), migrating multiple component RFs improves the final image if polarities are correctly treated. Using three component RFs gives rise to three possible situations regarding the coherence of the data. If a given grid point corresponds to an actual scatterer, we will extract coherent information on the three components of the RF. If the grid point corresponds to a geometry where no scattering is theoretically expected (e.g. a 180 angle between an incoming P and a scattered S wave), no energy will be migrated from the RF. Finally, if the grid point has high potential scattering values but the three components of the RF are not coherent, i.e. there is no scattering at that point, recorded amplitudes will be migrated, but will interfere destructively when stacked together. This allows us to consistently extract the coherent information of the RF. We will now explicitly describe the terms in  $\vec{w}(x, r)$  and how we modify the imaging principle to incorporate the free surface multiples.

## 2.4 Three-dimensional scattering patterns

Three-dimensional scattering patterns have been derived by a number of authors (e.g., Wu and Aki, 1985; Frederiksen and Revenaugh, 2004). Here we employ the 3D scattering patterns derived for a single scattering point that were obtained by Beylkin and Burridge (1990). The authors describe the behavior of a plane wave propagating in a smooth velocity model that hits a scattering point. Extending the equations for volumetric scattering to point scattering under the single scattering Born approximation, they express the amplitude and polarization of scattered waves for incoming unit vectors. This defines the

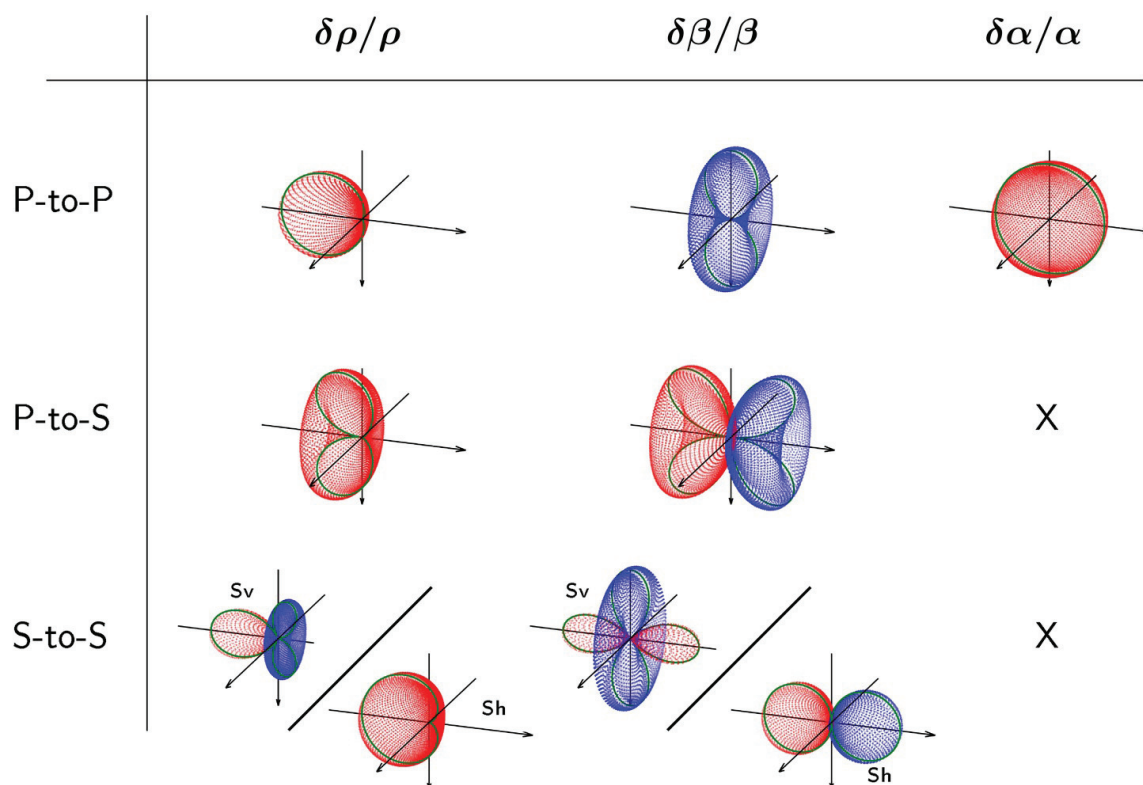


**Figure 2** – Representation of the 3D scattering patterns. The incoming wave arrives from the left-hand side along the horizontal axis as either a P-wave oscillating rightwards or an S-wave oscillating upwards, and leaves according to the scattering geometry. The scattering amplitude is represented as distance to the scattering point (center of each plot) and the polarity is represented by color, red being positive and blue negative. Here we can take both forward and back-scattering into account. All of them are symmetrical with respect to the horizontal incoming wave propagation axis. Note that  $\rho$  perturbations generate mostly back scattering and  $\alpha$ - $\beta$  perturbations have equal parts of forward and back scattering. The final value for a given scattering geometry is obtained by multiplying the amplitude value by the polarity for that scattering angle.

following scattering patterns,  $\varepsilon^{X_1 X_2}$ , for any given incident  $X_1$  and departing  $X_2$  seismic wave at the scattering point:

$$\begin{aligned} \varepsilon^{pp}(\theta) &= \frac{\delta\rho}{\rho_0} \left( 1 + \cos(\theta) + \frac{\beta_0}{\alpha_0} (\cos(2\theta) - 1) \right) \\ &\quad + 2 \frac{\delta\alpha}{\alpha_0} + \frac{\delta\beta}{\beta_0} \left( 2 \frac{\beta_0^2}{\alpha_0^2} (\cos(2\theta) - 1) \right) \end{aligned} \quad (2)$$

$$\begin{aligned} \varepsilon^{ps}(\theta) &= \frac{\delta\rho}{\rho_0} \left( \sin(\theta) + \frac{\beta_0}{\alpha_0} \sin(2\theta) \right) \\ &\quad + \frac{\delta\beta}{\beta_0} \left( 2 \frac{\beta_0}{\alpha_0} \sin(2\theta) \right) \end{aligned} \quad (3)$$

$$\varepsilon^{sp}(\theta) = -\varepsilon^{ps} \quad (4)$$

$$\begin{aligned} \varepsilon^{svsv}(\theta) &= \frac{\delta\rho}{\rho_0} \left( \cos(\theta) + \cos(2\theta) \right) \\ &\quad + \frac{\delta\beta}{\beta_0} \left( 2 \cos(2\theta) \right) \end{aligned} \quad (5)$$

$$\varepsilon^{sHsH}(\theta) = \frac{\delta\rho}{\rho_0} \left( 1 + \cos(\theta) \right) + \frac{\delta\beta}{\beta_0} \left( 2 \cos(\theta) \right) \quad (6)$$

where  $\alpha$  is the P-wave velocity,  $\beta$  is the S-wave velocity,  $\rho$  is the density, subscript  $\cdot_0$  corresponds to the smooth reference model,  $\delta$  corresponds to the local heterogeneity at the scattering point and  $\theta$  is the scattering angle between the incoming  $X_1$  phase and the  $X_2$  scattered phase in the scattering plane at the scattering point. A visual representation of the 3D scattering patterns can be found in figure 2. Here, we note that  $S_V$  is defined locally at the scattering point and is the part of the S-wave that oscillates in the scattering plane, not in the great-circle plane. Conversely,  $S_H$  oscillates orthogonally to the scattering plane.

In the scope of this article, we will use fixed values for  $\delta\alpha$ ,  $\delta\beta$  and  $\delta\rho$ . More specifically, we use (1)  $\delta\rho = 0$  in all equations, effectively removing the back-scattering linked to jumps in density from our analysis, (2)  $\delta\alpha = 0$  for the P-to-S and S-to-S scattering and (3)  $\delta\beta = 0$  for the P-to-P scattering. We have to resort to these arbitrary choices because our migration method does not rely on an inversion, hence we cannot easily mitigate the individual contributions of variations in  $\rho$ ,  $\alpha$  and  $\beta$ . Therefore we decide to focus on the main parameter for each scattering configuration, with  $\alpha$  variations preferred for outgoing P-waves and  $\beta$  variations preferred for outgoing S-waves (see, e.g., [Bostock and Rondenay, 1999](#); [Bostock et al., 2001](#)). This will be represented by subscript  $\cdot_\beta$  and  $\cdot_\alpha$  respectively hereafter.

The scattering angle  $\theta$  is estimated from the directions of propagation of the incoming and scattered waves at the grid point, which are obtained from the gradient of the wavefront given by the Eikonal solver. The angle  $\theta$  is used to estimate the amplitude and polarity of the scattered wave (eqs.(2) to (6)). This polarization vector is then projected on the (R,T,Z) reference frame at the station, thus resulting in a predicted amplitude vector  $\vec{w}(x, r)$ . The level of coherence between the observed waveforms and amplitudes predicted from the scattering geometry is measured by computing the dot product of the recorded energy vector  $\Delta\vec{u}(r, t = T(r, x))$  and the predicted energy vector  $\vec{w}(x, r)$  from the surface projection. This tells us how much energy scattered at point  $x$  is expected to contribute to each component of the RF, and thus defines the level of recorded amplitude that is migrated to depth.

## 2.5 Forward scattered waves and free surface back-scattered multiples

Standard RF studies interpret the phases observed in deconvolved waveforms only as forward P-to-S or S-to-P conversions, referred to as PS and SP hereafter, although a well-known issue is the influence of the free surface multiples (Levander and Miller, 2012; Lekić and Fischer, 2013). Interferences from these multiples can stack up at spurious depths, and can generate serious artifacts that hinder the interpretation of features in the migrated images (Cheng et al., 2017). However, if properly accounted for, multiple reflections can become useful as they bring complementary information about the structure (see, e.g., Tauzin et al., 2016).

The free surface multiples are the waves that reflect at the surface of the Earth and are then backscattered towards the surface by the same heterogeneities that generate the direct PS scattering. In the case of the Born approximation, we are looking at three different modes. The first one to arrive is reflected as a P-wave at the surface, hereafter referred to as lower case p, and backscattered as a P-wave. The second one is also reflected as a P-wave but backscattered as an S-wave towards the station. The third one is reflected as a converted S-wave at the surface, hereafter referred to as lower case s, and backscattered as an S-wave. These phases will be referred to as PpP, PpS and PsS respectively. Note that the S-to-S scattering for the PsS wave has as both an  $S_V$ -to- $S_V$  and an  $S_H$ -to- $S_H$  component.

In the next section we will show how these phases reflected at the surface (i.e., PpP, PpS and PsS) are accounted for in the migration algorithm. Let us first write the imaging principle in the case of forward PS scattering mode. Since we work with a finite number



of sources  $i$  and stations  $j$ , and use a finite number of grid points  $k$ , equation eq.(1) can be rewritten in a discrete form:

$$f_{ps}(k) = \sum_i \sum_j G(j, k) \varepsilon^{ps}(i, j, k) \vec{\delta}_{ps}(j, k) \cdot \Delta \vec{u}(i, j, t_P + t_S - t_D) \quad (7)$$

where  $f_{ps}(k)$  is the scattering potential for the forward PS scattering mode at a given grid point  $k$ ,  $G(j, k) = 1/d(j, k)$  is the amplitude correction for geometrical spreading with  $d(j, k) = |x(k) - r(j)|$  the distance between the receiver and the scatterer,  $\varepsilon^{ps}$  and  $\vec{\delta}_{ps}$  represent the amplitude and polarization of the scattered S-wave given by the scattering pattern for the Ps mode (eqs.(3)). Finally,  $t_P$ ,  $t_S$  and  $t_D$  are travel times computed in the reference 3D velocity model described in the previous section. We use the fast marching method (FM3D, de Kool et al., 2006) to compute these travel time fields.

## 2.6 Integration of free surface multiples

To incorporate the scattering modes from free-surface multiples in the migration and map their energy back at the correct location, we must compute their associated travel times and amplitudes corrections. Specifically, we need to compute the travel times for the initial P-wave from the source to the surface, the reflected downward going P- and S-waves and the back-scattered P and S-waves from all the grid points to the receivers. Again, we use the fast marching method to compute three travel time fields (P, Ps and Pp) for each source and two (upgoing P and S) for each receiver. By combining these Pp and Ps travel times with the P and S scattered wave travel times we get the travel times for all modes.

We use the scattering patterns described above to get the amplitudes and polarities for these modes as well. However, in the case of the free surface multiples, the behavior of the amplitude and polarity of the phases is more complex than a single scattering pattern. In this case, we combine the appropriate  $\varepsilon^{X_1 X_2}$  scattering patterns in a complete, phase-specific scattering pattern  $S_m$ , where  $m$  represents one of the four scattering modes. We effectively treat the multiples as a double scattering problem with one of the scattering being a reflection at the free surface of the Earth and the other the scattering at depth. Note that the reflection at the free surface is not a scattering per se, as the surface is seen as a horizontal discontinuity, and only one direction is possible for the reflected wave. This way we are still in the Born approximation and in a single scattering regime.

The expressions for all the  $S_m$  can be found hereafter and are illustrated along migration isochrons in figure 3. To obtain the sections in figure 3, we first computed the

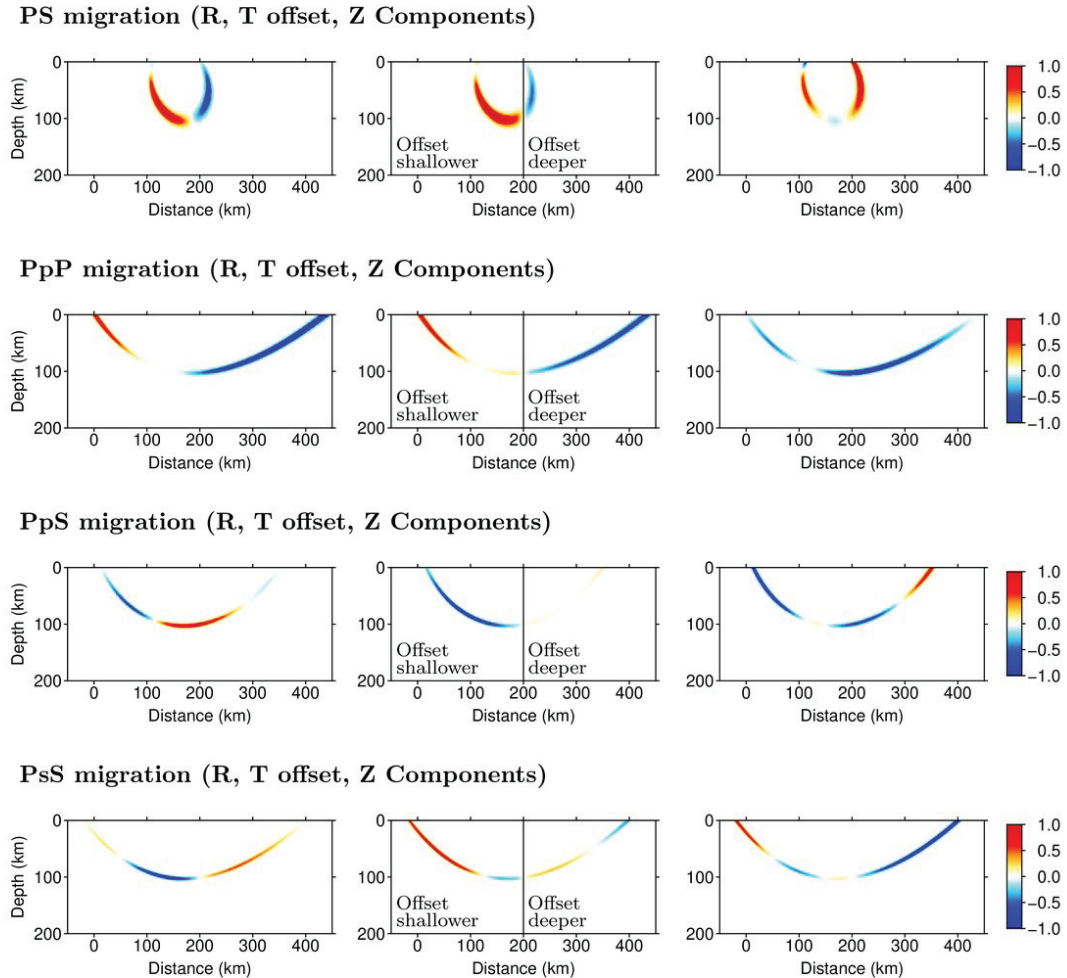


**Figure 3** – 2D representation of the complete scattering weights, without focussing, for the four scattering modes and the three components migration. These are obtained by migrating a unit gaussian pulse along the isochron for a given scattering mode for a source that arrives under the station from the right-hand side. They correspond to the projection of the weights from the scattering patterns at the surface for each recorded component, with blue corresponding to a polarity reversal and red to a preserved polarity. Each row corresponds to a different scattering mode and the columns correspond to the three components of the recorded wavefield. For the transverse component, because its amplitude is null along the great circle plane, the slice through the 3D model is offset shallower (towards the reader) or deeper (away from the reader) to better visualize its amplitude and polarity behaviour. This is what produces the visible polarity reversals at 200km.

theoretical arrival times for all modes associated with a 100km deep horizontal discontinuity. We then created independant synthetic waveforms for all modes by generating a positive unit gaussian pulse centered on these arrival times. Finally we migrated these waveforms independently according to their respective complete scattering pattern for each mode. This figure shows how the scattering patterns allow to invert the polarity of the incoming phases independently for each mode and on each component. This is particularly visible on the radial and vertical components of the PpS mode. The complete scattering patterns are as follows:

$$S_{ps} = \varepsilon_{\beta}^{ps}(\theta) \quad (8)$$

$$S_{ppp} = \varepsilon_{\alpha}^{pp}(\theta') \varepsilon_{\alpha}^{pp}(\theta) \quad (9)$$

$$S_{pps} = \varepsilon_{\alpha}^{pp}(\theta') \varepsilon_{\beta}^{ps}(\theta) \quad (10)$$

$$S_{pss} = \varepsilon_{\beta}^{ps}(\theta') \left( (\vec{\delta}' \cdot \vec{\delta}) \varepsilon_{\beta}^{sVsV}(\theta) + (\vec{\delta}' \cdot \vec{\gamma}) \varepsilon_{\beta}^{sHsH}(\theta) \right) \quad (11)$$

For the PS scattering this simply corresponds to the direct scattering pattern restricted to the  $\delta\beta/\beta$  contribution. In contrast to the direct PS scattering mode, there are two scattering angles to consider for the multiples. The first one is the angle  $\theta'$  at the free surface reflection, which is the angle of the incident wave in the great circle plane that contains the source and the scattering point. The second one is the angle  $\theta$  at the scattering point, which is in a second scattering plane defined by the free surface reflection point, the scattering point and the receiver. Moreover, for the S-to-S scattering in the PsS scattering mode, we have to consider the polarization of the wave. In this case,  $\delta'$  is the polarization of the wave that is reflected at the surface along the great circle path. This reflected wave is scattered partly as an  $S_V$ -wave along  $\delta$  and partly as an  $S_H$ -wave along  $\gamma$ , which is orthogonal to  $\delta$ . This leads to a generalized definition of the imaging principle, derived from equation eq.(7), for every scattering mode:

$$f_m(k) = \sum_i \sum_j G(j, k) S_m(i, j, k) \vec{\delta}_m(j, k) \cdot \Delta \vec{u}(i, j, T_m) \quad (12)$$

where  $f_m(k)$  is the scattering potential for the scattering mode  $m$  at the grid point  $k$ ,  $m \in [1, 4]$  represents one of the four the scattering modes (either PS, PpP, PpS, PsS),  $S_m(i, j, k)$  is the complete scattering pattern for a given  $m$  mode,  $\vec{\delta}_m(j, k)$  is the unit polarization vector of the scattered wave arriving at the receiver for a given  $m$  mode, and  $T_m$  corresponds to the travel time estimated in a reference 3D model for a given  $m$  scattering mode. In the case of the PpP phase, this corresponds to  $T_{PpP} = t_P(i, x') +$

$t_p(x', x) + t_P(x, j) - t_D$  with  $x'$  denoting the surface reflection point and  $x$  the potential scattering point.

Since estimating the exact direction of polarization  $\vec{\delta}_m(j, k)$  of the scattered wave at the receiver requires considerable extra computational cost, here we assume that the polarizations do not change from the scattering point  $k$  to the receiver  $j$  at the surface. This is equivalent to assuming straight rays in a homogeneous medium from the scattering point  $k$  to the receiver  $j$ . It is a reasonable approximation for lithospheric and upper mantle investigations but may represent an oversimplification for lower mantle studies, where the variations in elastic property bend the rays significantly before they reach the surface.

An additional weight is applied to the data in order to limit the contribution of long distance interactions at shallow depths as they leak significant amounts of energy into the images above the region of interest and blur the images. This means that we effectively put a sensitivity region below the receivers that minimizes the arrivals with large incidence angles. Cheng et al. (2016) proved that this kind of sensitivity function helps remove artifacts in the migrated images. However, this means that we limit our ability to image steeply dipping reflectors. For the PS migration, this limits the dip of recoverable structures to  $45^\circ$ , and for the free surface multiples it means that we lose sensitivity above  $\sim 30^\circ$  dip. To down-weight our data, we use a 4<sup>th</sup> power cosine function of the incidence angle that provides a sharp roll-off at an angle of  $45^\circ$ , leading to the following updated expression for our imaging principle:

$$f_{m, foc}(k) = \sum_i \sum_j F(j, k) G(j, k) S_m(i, j, k) \vec{\delta}_m(j, k) \cdot \Delta \vec{u}(i, j, T_m) \quad (13)$$

where  $f_{m, foc}(k)$  is the focused scattering potential for the scattering mode  $m$  at the grid point  $k$ ,  $F(j, k) = \cos^4(\nu)$  is the focusing factor and  $\nu(j, k)$  is the incidence angle of the scattered wave under the station. This factor can be set to 1 if one wants full coverage of possible dip angle resolution.

Using this imaging principle we get four separate images, one for each scattering mode. In every image, the energy migrated from the waveforms due to one of the scattering mode is back propagated at the correct depth, while the other three modes are migrated at spurious depths. However, the benefit of this approach is that these spurious features are migrated at different positions in each image, whereas real structure will be at coherent depths over all modes. This means that extracting the coherent information between these four images should penalize against spurious features and enhance true structures.

## 2.7 Image Stacking Techniques

To enhance the structure that is most coherent between the forward and back-scattered modes, we implement and test three stacking techniques: linear stacking, phase-weighted stacking, and 2<sup>nd</sup> root stacking. The phase weighted stack uses a measure of the coherence of the phases of all the migrated signals whereas the 2<sup>nd</sup> root stack acts as an amplitude coherence filter. The following sections describe each of these techniques.

### 2.7.1 Linear stacking

The first stacking technique is a linear stack over the four modes, and can be summarized in the following equation:

$$f_{lin}(k) = \sum_m \sum_i \sum_j F(j, k) G(j, k) S_m(i, j, k) \vec{\delta}_m(j, k) \cdot \Delta \vec{u}(i, j, T_m) \quad (14)$$

where  $f_{lin}(k)$  is the stacked scattering potential for all 4 modes at the grid point  $k$ .

As expected, this stacking scheme will enhance the features that are coherent across all four modes. However since the sum is linear, we also expect the spurious features to be reduced by less than an order of magnitude if all modes have roughly the same migrated amplitude. This means that the spurious features will still be visible on the final image.

### 2.7.2 Phase-Weighted stacking

The second technique we consider is phase-weighted stacking (PWS). In this approach, we compute the instantaneous phase  $\varphi(t)$  of the input RF signals based on their analytical signals (Schimmel and Paulssen, 1997; Costa et al., 2018). We then migrate and stack the complex phase  $e^{i\varphi_k(x)}$  at each grid point, and take the norm of the stacked complex phase as a measure of the coherence (Cooper, 2009). This can be summarized in the following general equation:

$$y(x) = \frac{1}{N} \sum_j s_j(x) \left| \frac{1}{N} \sum_k e^{i\varphi_k(x)} \right| \quad (15)$$

where the first sum represents the amplitude stack of the data  $s_j$ , the second sum is the norm of the stacked migrated complex phases  $e^{i\varphi_k}$  that acts as a filter to the amplitude stack, and  $y(x)$  is the stacked migrated signal. On one hand, if the signals are coherent, their instantaneous phases  $\varphi_k$  will point in the same direction and the modulus of the sum of the complex phases will be high. On the other hand, if the signals at a given grid point consists mainly of noise, then the instantaneous phases will point towards random

directions and cancel out, leading to a minimum in the modulus of the stacked complex phases.

In our case, we need to compute the instantaneous phase of the 3D incoming signal using the estimated polarization of the scattered waves, which is different at every grid point, based on the instantaneous phase of the three components of the RF. This leads to a reformulation of our imaging principle as follows:

$$f_{pws}(k) = C(k) \sum_m \sum_i \sum_j F(j, k) G(j, k) S_m(i, j, k) \vec{\delta}_m(j, k) \cdot \Delta\tilde{\mathbf{u}}(i, j, T_m) \quad (16)$$

where  $f_{pws}(k)$  is the phase-weighted stacked scattering potential for all 4 modes at the grid point  $k$ .  $C(k)$  is the coherence of the four modes defined as:

$$C(k) = \left| \sum_m \sum_i \sum_j e^{i\varphi(m, i, j, k)} \right| \quad (17)$$

with

$$\varphi = \arg(S_m \vec{\delta}_m \cdot \Delta\tilde{\mathbf{u}})$$

where  $\Delta\tilde{\mathbf{u}}$  is the analytical signal of  $\Delta\mathbf{u}$ .

### 2.7.3 2<sup>nd</sup> root stacking

Finally, we consider a 2<sup>nd</sup> root stacking technique based on Schimmel and Paulssen (1997). This is a non-linear stacking method that sums the square root of the amplitudes for all the traces and takes the resulting image to the power 2 after the stack. The general formula for N<sup>th</sup> root stacking can be summarized as follows:

$$y(x) = \text{sign}(r(x)) |r(x)|^n \quad (18)$$

with

$$r(x) = \frac{1}{N} \sum_j^N \text{sign}(s_j(x)) |s_j(x)|^{1/n}$$

where  $r(x)$  is the stack of the N<sup>th</sup> roots of the  $s_j(x)$  data, and  $y(x)$  is the final stacked migrated signal taken to the N<sup>th</sup> power. We tried other power values for the N<sup>th</sup> root stacking method but higher values tend to remove everything but the sharpest coherent contrasts, which can be problematic for smaller coherent scattering structures.

In our case, if we assign the variable  $\mathcal{A}(i, j, k)$  to the corrected amplitude for every  $(i, j, k)$  triplet and the variable  $\mathcal{S}(k)$  to the value of the stacked square root of the amplitudes at grid point  $k$ , we can rewrite our imaging condition as:

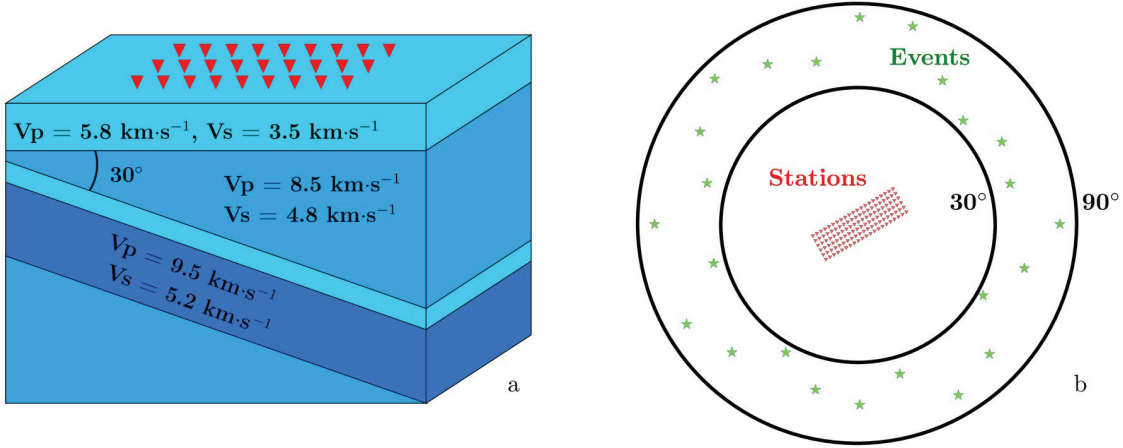


**Figure 4** – Synthetic setup for the tests in figures 5 to 9. Red triangles represent the stations in the array and green stars represent the events. The array is elongated in the along-dip direction and the sources are evenly spaced in backazimuth and assigned a random epicentral distance from  $30^\circ$  to  $90^\circ$ . (a) is a block diagram that represents the velocity model for figure 9 (cf. table 1). (b) is a map view of the array and shows the event distribution for the tests performed in figures 7 to 9. For enhanced clarity only half the rows and half the columns of the array are represented and figures are not to scale.

$$f_{2rs}(k) = \text{sign}(\mathcal{S}(k)) \left| \sum_m \sum_i \sum_j \text{sign}(\mathcal{A}(i, j, k)) \left| F(j, k) G(j, k) S_m(i, j, k) \vec{\delta}_m(j, k) \cdot \Delta \vec{u}(i, j, T_m) \right|^{1/2} \right|^2 \quad (19)$$

where  $f_{2rs}(k)$  is the 2<sup>nd</sup> root stacked scattering potential for all 4 modes at the grid point  $k$ .

In the current section we described the physics and the geometry of the problem with the scattering patterns. We explicitly described the equations and the imaging principles we need to obtain the final stacked images of the subsurface. In what follows, we use synthetic examples to show that the resulting imaging principle (eq.(13)) is robust, and that we are able to integrate all the available data in the analysis without back-azimuth or slowness restrictions. Then we show how the different stacking methods affect the results, and finally we discuss the computational efficiency of the method and apply the imaging principles to real data.

**Table 1** – Synthetic models and setups. Dip corresponds to the upper interface of the layer. The " $\infty$ " corresponds to the half-space at the bottom of the model. Thickness is taken at the center of the model and corrected for dip.

Model ID	Thickness ( $km$ )	Dip	$V_P(km \cdot s^{-1})$	$V_S(km \cdot s^{-1})$	Sources	Receivers
WCS1	200	$0^\circ$	8.0	5.0	4	451
	$\infty$	$40^\circ$	8.8	5.5		
WCS2	100	$0^\circ$	8.0	5.0	24	451
	$\infty$	$10^\circ$	8.8	5.5		
R2DSZ	40	$0^\circ$	5.8	3.5	24	451
	110	$0^\circ$	8.5	4.8		
	10	$30^\circ$	5.8	3.5		
	30	$30^\circ$	9.5	5.2		
	$\infty$	$30^\circ$	8.5	4.8		
MRT	40	$0^\circ$	6.0	4.0	52	35
	60	$0^\circ$	6.6	4.4		
	$\infty$	$20^\circ$	7.2	4.8		
MPKDM	20	$0^\circ$	6.2	3.6	52	35
	20	$0^\circ$	6.8	3.8		
	20	$0^\circ$	7.6	4.2		
	$\infty$	$0^\circ$	8.0	4.5		

### 3 Synthetic tests

Here we conduct a series of tests on three synthetic models that we designed to show how including scattering patterns, three component RFs and free-surface multiples in the migration improves the final images. The synthetic models and test geometries are described in table 1 and hereafter. The experimental setting for the third synthetic scenario (R2DSZ) is shown in figure 4.

#### 3.1 Model and setup

##### 3.1.1 Synthetic models

The first model WCS1 comprises 2 layers separated by an interface with contrasts of 10% in  $\alpha$ ,  $\beta$  and  $\rho$  at a  $40^\circ$  dip. This first synthetic model was designed to represent a typical challenging scenario where amplitude and polarities of the data strongly vary with epicentral distance and back-azimuth. In this case, the polarity reversals that arise from



**Table 2** – Index of migrated sections with the effects taken into account for each. Additional processing corresponds to the projection of the stations along the imaging line in the case of the MEDUSA experiment.

Fig.	Element	Components	Scat. Patterns	Multi-Mode	Sources	Additional Proc.
5	a/b/c	R	no	no	1-2	no
	d/e/f	R	yes	no	1-2	no
6	a/b/c	R	no	no	1-2	no
	d/e/f	T,Z	no	no	1-2	no
	g/h/i	R,T,Z	yes	no	1-2	no
7	a/b/c/d	R,T,Z	yes	no	24	no
8	a/b/c	R,T,Z	yes	yes	24	no
9	a/b/c/d	R,T,Z	yes	no	24	no
	e/f/g	R,T,Z	yes	yes	24	no
10	a/b/c	R,T,Z	yes	yes	24	no
12	a	R,T,Z	yes	yes	52	no
	b/c/d	R,T,Z	yes	yes	52	yes
13	a	R,T,Z	yes	yes	52	no
	b/c/d	R,T,Z	yes	yes	52	yes

step arrivals on dipping discontinuities need to be addressed to correctly interpret the data (Cheng et al., 2016).

The second synthetic model WCS2 represents a worst case scenario in terms of the influence of the free surface multiples. It has the same elastic contrasts and a  $10^\circ$  dip, and in this case we expect the free surface multiples to have a strong contribution in the migrated image for the PS mode.

The third model R2DSZ comprises 5 layers and represents an idealized 2D subduction zone. The first layer is a 30 km thick overriding crust. The second layer is the overriding mantle. The third and fourth layers are the subducting crust and lithospheric mantle that form the subducting plate, with respective thickness of 10 and 30 km, and dipping at a  $30^\circ$  angle. The last layer is the unperturbed mantle under the subducting plate.

The synthetic waveforms are calculated in the sharp models for models containing sharp interfaces. Conversely, the travel times used to migrate these data are computed

in a smoothed version of these models, with a 10km buffer around the discontinuities, in order to emulate reference models obtained through local or regional tomography.

### 3.1.2 Synthetic setup

In order to demonstrate that our migration method can be applied at continental scale, we test it on a synthetic array that spans 100 by 400 km (figure 4). The array comprises 11x41 regularly spaced stations, with station spacing of just above 10 km. The sources are regularly spaced in back azimuth, i.e. every 90° for WCS1/WCS2 and every 15° for R2DSZ. They are given a random epicentral distance from the center of the array between 30° and 90°. For R2DSZ, this simulates arrivals from a realistic range of slownesses and back azimuths. We acknowledge that this is an idealized geometry that is rarely available with field data as arrays usually have irregular shapes and sample an irregular distribution of back-azimuths. We used up to 24 sources and created a total of up to 10824 synthetic waveforms for each synthetic velocity model.

For the models WCS1 and WCS2, applying the successive imaging principles will help us demonstrate the improvements offered by three component RFs and correcting for scattering patterns. For the realistic 2D subduction (model R2DSZ), we expect this setup to image the overriding and subducting crust as a clear positive peak. We also expect the method to resolve both the crust and the LAB of the subducting slab.

### 3.1.3 Synthetic waveforms

The synthetic data are generated with a ray-based approach for modeling teleseismic body waves in dipping anisotropic structures (Raysum software, [Frederiksen and Bostock, 2000](#)). This approach computes the arrival times and amplitudes of all converted and reflected (i.e., first-order free surface multiples) phases in a layered geometry. The advantage of this algorithm is that it is accurate and computationally efficient as it uses analytical formulae to compute the travel times, amplitudes and phase of the transmitted and scattered waves.

The Raysum software can handle a large number of planar, homogeneous anisotropic layers with arbitrary strikes and dips. However, the models cannot contain velocity or anisotropy gradients inside the layers and the layers themselves cannot intersect in regions that are traversed by rays. Because of these limitations, we could not simulate a laterally limited slow mantle wedge in our idealized subduction zone model. Since our simulations cannot reproduce fully 3D conditions, we will refer to them as 2.5D synthetics hereafter.

Raysum outputs a sum of dirac delta functions convolved with a Gaussian source time

function with a variable standard deviation, set to 3 seconds in our case. We use these data directly as our “receiver functions”, without noise, as our source function is already a Gaussian pulse.

### 3.1.4 Overall computational cost

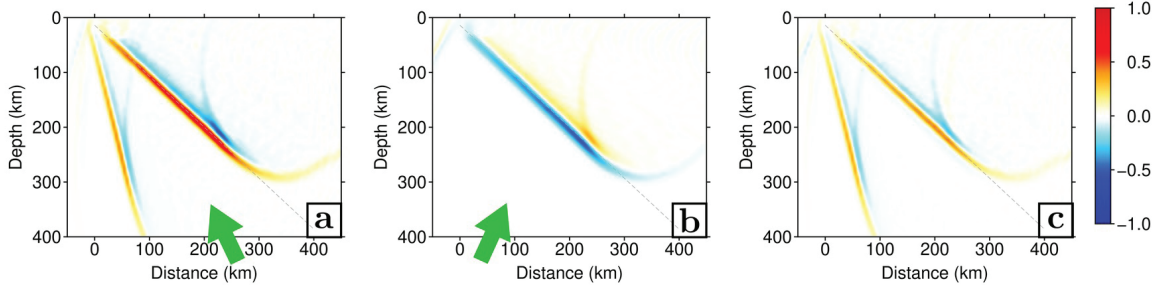
The Eikonal solver estimates the travel times of scattered waves through a cube of  $6^\circ \times 6^\circ$  in latitude and longitude and 500km in depth. Our migration is performed in a cube of  $5^\circ \times 5^\circ$  by 450km depth to account for potential edge effects in travel-time calculations. The computations and migrations for all the synthetic cases were carried out on a single core of an Intel Xeon E5-2650 v2 octa-core processor. The Raysum and analytical signal computation take under two minutes to run. The exact number of sources and receivers used for every model, for synthetic and field data, are detailed in table 2. Running FM3D for 24 sources and 451 receivers takes three hours with a voxel size of  $5 \times 5 \times 5$ km, on average. The migration of the 10824 RF with the multi-mode algorithm also takes three hours to run. The memory requirements for the case just described are approximately 12Gb. This includes the three time tables per source, namely the upgoing direct P and downgoing Pp and Ps wavefields, the two time tables per receiver, namely the upgoing scattered P and S wavefields, and the waveforms for all source-receiver pairs. For the smaller experiments on models WCS1 and WCS2, it takes 15 minutes and one hour to run all steps.

## 3.2 Scattering patterns and three-component migration

As shown in Cheng et al. (2016), the scattering patterns are important to account for amplitude variations and polarity reversals in the various phases. In this section, we illustrate this point by applying the method to the synthetic case WCS1 described in in table 1, with a single  $40^\circ$  dipping interface. Results are shown in figure 5 and figure 6, where arrows and symbols indicate the direction of the propagation of the incoming waves. In each row of these figures, the images are normalized by the maximum absolute amplitude of the strongest image.

The migrated images for the PS mode of two sources located on opposite sides of the structure, both in the imaging plane, are shown in figure 5. The wavefield for the first source (left column) comes from a down-dip direction, which is to the right in this geometry. The wavefield for the second source (middle column) comes from an up-dip direction, which is to the left in this geometry. The results for two sources that were rotated  $90^\circ$  compared to the previous ones, which puts them in the strike parallel plane, are

### No scattering patterns, R Component (down-dip, up-dip, both)



### Scattering patterns included, R Component (down-dip, up-dip, both)

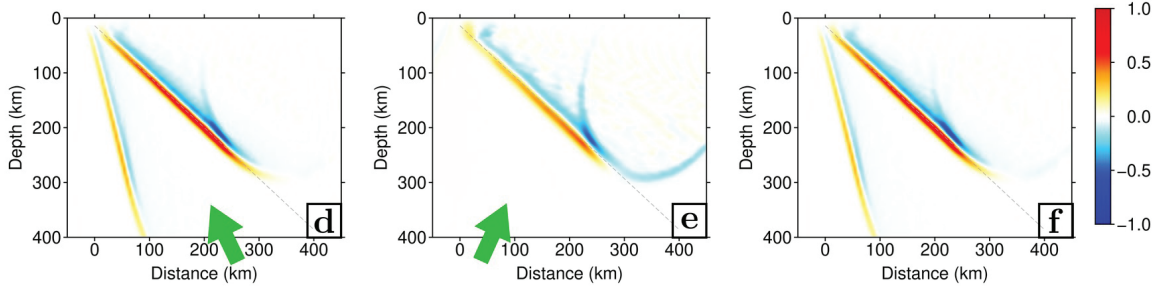
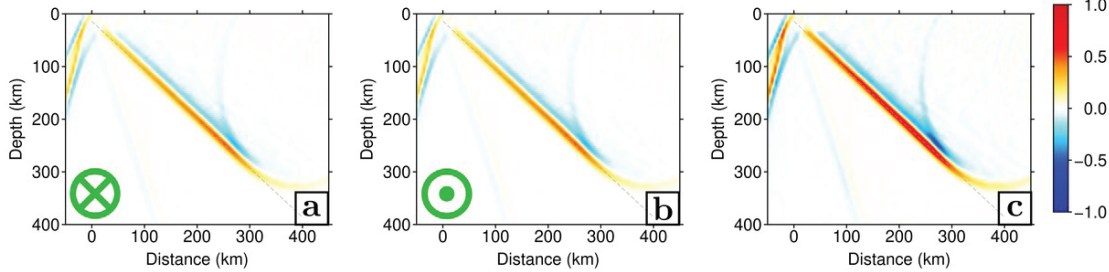


**Figure 5** – Influence of the Scattering Patterns. PS migration of radial RFs for a 2D model containing a single interface with  $40^\circ$  dip and 10%  $\delta V_P$ ,  $\delta V_S$  and  $\delta \rho$  perturbations (model WCS1, table 1). Arrows represent the direction of propagation of the incoming waves. (a) and (d) correspond to a down-dip source coming from the right-hand side, (b) and (e) to an up-dip source coming from the left-hand side, (c) and (f) correspond to the stacks of (a+b) and (d+e) respectively. (a) to (c) are migrated without the scattering patterns and show inconsistency in the migrated polarity. (d) to (f) are migrated with the effects of scattering patterns taken into account and show consistent polarity, which improves the stacked image.

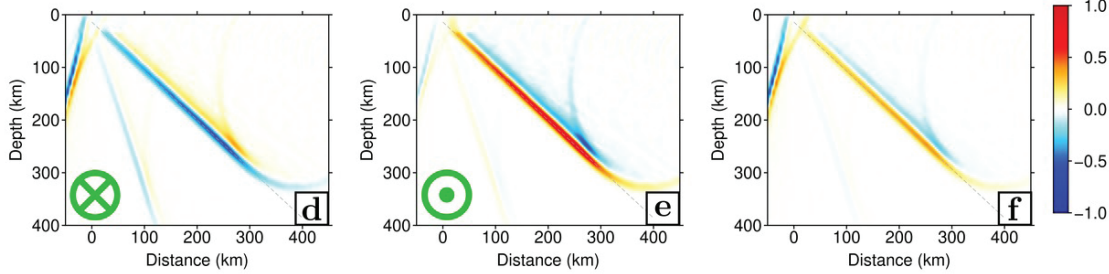
shown in figure 6. The wavefield for the first source (left column) comes from the reader’s perspective into the figure and the wavefield for the second source (middle column) comes from the opposite direction, facing the reader. We illustrate our method with single-source migrations by introducing the various elements described in section 2 one by one. Table 2 describes which elements of the imaging principle are taken into account in every figure.

We shall now describe each panel of figures 5 and 6. In figure 5 we migrate the radial component of the PS mode in the simple 2D model WCS1 to show the effect of applying the scattering pattern corrections. The images from figure 5a to 5c (top row) are migrated without taking the scattering patterns into account. In figure 5a (source on the right-hand side, first column) the migration algorithm focuses most of the energy on the discontinuity (dashed line). However, the free surface back-scattered phases leak into the image and introduce spurious structures with higher dip values and alternating signs. In this migrated image, some of the scattered energy is also smeared

No scattering patterns, R Component (into the page, out of the page, both)



No scattering patterns, T+Z Components (into the page, out of the page, both)



Scattering patterns included, 3 Components (into the page, out of the page, both)

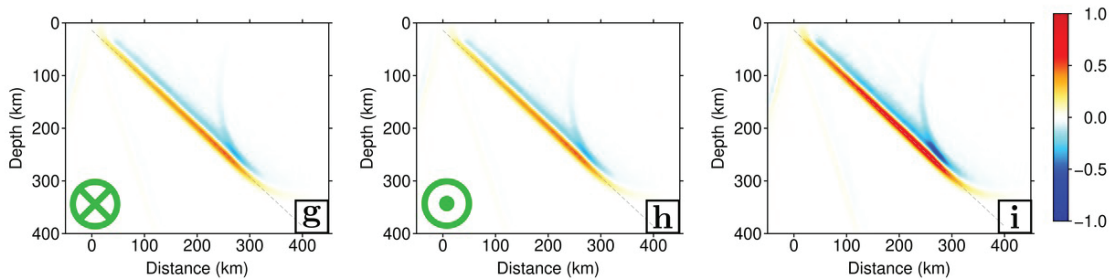


**Figure 6** – Influence of the three component migration. PS migration for a 2D model containing a single interface with  $40^\circ$  dip and 10%  $\delta V_P$ ,  $\delta V_S$  and  $\delta \rho$  perturbations (model WCS1, table 1). Symbols represent the direction of propagation of the incoming waves. (a), (d) and (g) correspond to an along-strike source coming from the reader’s perspective, (b), (e) and (h) to an along-strike source coming from inside the page, (c), (f) and (i) correspond to the stacks of (a+b), (d+e) and (g+h) respectively. (a) to (c) are the radial components of the RFs migrated without the scattering patterns and show coherent but relatively low amplitudes compared to figure 5a. (d) to (f) are transverse and vertical components of the RFs migrated without the scattering patterns and show higher energy content but inconsistent polarities. In (g) to (i), the three components of the RFs migrated with the effects of the scattering patterns taken into account.

above the discontinuity. The image in figure 5b shows that for a source on the opposite side (second column) the migration also focuses the energy on the discontinuity at the correct depths but the polarity reversal has not been accounted for and the sign of the migrated scattering potential is negative. Notice also that this image contains slightly less energy from the multiples as this particular geometry generates less scattering overall on the radial component of the RF. Figure 5c shows that the image generated by linearly stacking over both sources (third column) is dominated by the wavefield coming from the down-dip direction and that the two sources interfere destructively where they are supposed to stack up.

If we apply the amplitude and polarity corrections given by scattering patterns and redo the same migration, we can see on figure 5d and figure 5e (bottom row) that the sign of the scattering potential of the imaged structures are now coherent for the two sources. We also note that the image based on a wavefield coming from the down-dip direction (source on the right-hand side, first column) is significantly clearer as the positive and negative parts of the scattering pattern correction ellipse globally cancel out far away from the scattering interface. The results in figure 5f show that this time the two images interfere coherently where they are expected to. This proves that taking scattering physics into account greatly improves the imaging: we migrate the correct polarities each time, and hence the images stack constructively. We eliminate the polarity problem for large dip angles and can automatically assimilate data from all slownesses.

The benefit of migrating the 3 components of the RF for large dips and oblique, along-strike arrivals in the WCS1 scenario is shown in figure 6. We show that there is much complementary information to be gained from 3 components migration, provided that polarity reversals are properly accounted for. Similarly to figure 5, we migrate the PS mode for the same simple 2D model. The results in figure 6a to 6c (top row) show the migrated images of the radial component for two sources placed symmetrically on one side (into the page, first column) and the other (out of the page, second column) of the dipping structure. It shows identical images for the two sources, which is expected. The signs of the discontinuities are correct in both images for the PS mode but we also observe considerable energy from the PpS and PsS multiples stacked on the left side of the images. The summed image (third column) in figure 6c shows the same attributes. However, the maximum absolute amplitude in this image is lower than in figure 5a. When migrating the transverse and vertical components of the RF in figure 6d and 6e (middle row), the maximum amplitude is higher but there are polarity issues. Moreover, the images are not identical anymore because the transverse component is defined in opposite directions for both sources. Therefore we can see in figure 6f that the stack of the two previous

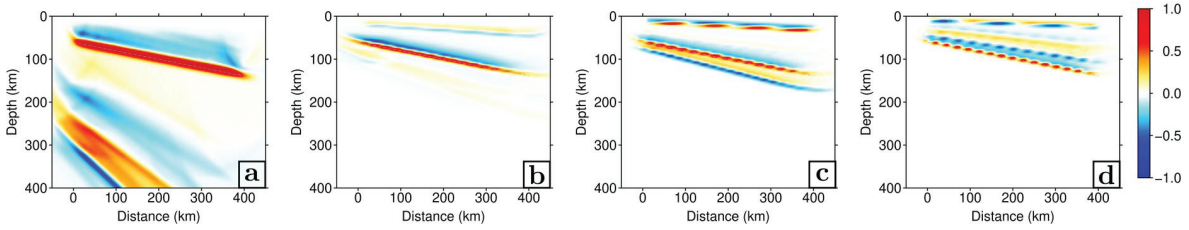


**Figure 7** – Single-mode migrations of three components RF for a 2D model containing a single interface with  $10^\circ$  dip and  $10\%$   $\delta V_P$ ,  $\delta V_S$  and  $\delta\rho$  perturbations (model WCS2, table 1). Panel (a) is the PS, (b) the PpP, (c) the PpS and (d) the PsS migrations (cf. text). The data were generated for 24 sources regularly spaced in back-azimuth and with epicentral distances ranging between  $30^\circ$  to  $90^\circ$ . The four images recover the structure with the correct polarity but are affected by the other modes. The spurious migrated signals are at different locations in each migration.

images does not give a satisfactory result. By applying the scattering patterns on the three components, we solve the problem in figure 6g to 6i (bottom row). In this case, by migrating the three components of the RF with their proper scattering weights, we find identical images again, which is what we expect after the correction, and the amplitude in the stacked images are on the same order of magnitude as their counterparts in figure 5. Additional tests for zero to very large ( $80^\circ$ ) dips are available in figure S1 from the supplementary information.

Further testing taking into account only the phase term, or polarity, of the scattered signals yielded degraded images in which the spurious features are enhanced. This is because such strategies place a high weight on ray configurations where no scattering is expected. In the tests that we ran, this happens to enhance especially the contaminating signals. These results show that taking the amplitude term of the scattering patterns into account is key to reducing the contamination of migrated images by the various scattered modes.

Here we demonstrated the importance of the scattering patterns when migrating three component data. Moreover, we showed that integrating the three components of the RF into the imaging principle allows us to coherently retrieve the scattering potential for arbitrarily dipping discontinuities from all back-azimuths.

### 3.3 Multi-mode migration

As seen in figures 5 and 6, free surface multiples are clearly visible in the PS migration, even for very simple settings. They are easily distinguishable in the PS migrated image for this particular model, but their interpretation become increasingly more difficult with

the complexity of the setting. Here we will show how jointly migrating the four main scattering modes can help mitigate the contamination by free surface multiples in the interpretations of migrated images.

Since free surface multiples tend to be stronger and more difficult to interpret correctly in sub-horizontal settings, we choose a model with a  $10^\circ$  dipping interface, thus placing ourselves in a worst case scenario situation with regards to free surface multiples (Cheng et al., 2017). In this simulation we use 24 sources to cover all possible back-azimuth and incidence angles. The results in figure 7 show the migrations for the 4 individual scattering modes for model WCS2 described in table 1, which has one interface at a  $10^\circ$  dip.

The results for the three-component PS migration are shown in figure 7a. The dashed line shows the only feature that is present in the synthetic model. We can see a coherent signal that lines up with the structure, but also three spurious features associated with multiples: (1) a negative feature at approximately 180km to 380km depth that corresponds to the PpP multiple; (2) a positive feature at 250km to 400km depth that corresponds to the PpS multiple; and (3) a negative feature between 300km and 400km depth that corresponds to the PsS multiple.

We perform one migration for each scattering mode and the resulting images can be seen on figure 7b (PpP), figure 7c (PpS) and figure 7d (PsS). We find that the free surface multiples in the synthetic waveforms are correctly migrated in their respective images. However, in each image, three out of the four modes are still visible and wrongly migrated. They appear at different depths, and produce spurious structures with different dip angles. Specifically, phases slower than the currently migrated mode are mapped below the true scattering feature (e.g. in figure 7a), and phases faster than the currently migrated mode are placed above the scattering feature (e.g. in figure 7d). On these four migrated images, there is overall more spurious features than true features, but their locations are not coherent across the four single scattering mode migrations. These four images allow us to visually discriminate between real features, which have coherent amplitude across all 4 images, and the spurious features, which do not correlate on the different single scattering-mode images.

In this example, we can also notice that the time delays are more compressed in the multiple modes, and hence they have a higher spatial resolution than the direct PS conversion mode, especially for the S scattered waves (Rondenay, 2009). This is due to the fact that a ray covers a single unit distance (upgoing) between two consecutive points in depth for the PS mode and two (downgoing and upgoing) when we migrate a multiple.

Here we showed that we are able to migrate the free surface multiples at their correct



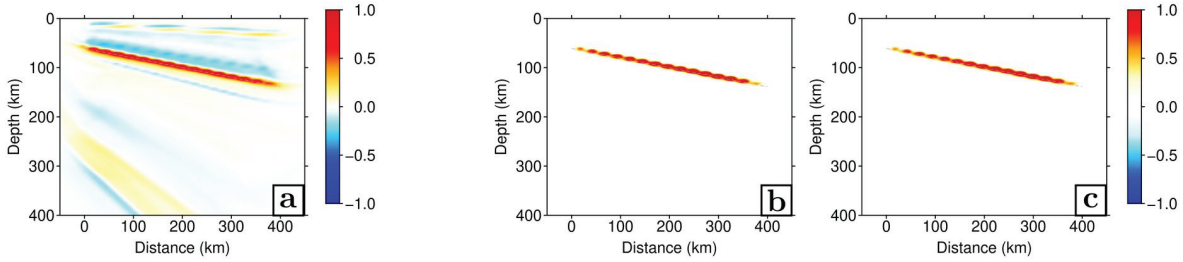


**Figure 8** – Multi-Mode migrations for a 2D model containing a single interface with a  $10^\circ$  dip and 10%  $\delta V_P$ ,  $\delta V_S$  and  $\delta \rho$  perturbations (model WCS2, table 1). (a) Linear stack, (b) phase-weighted stack, and (c) 2nd root stacks for the multi-mode migration of the 3 component RFs with scattering patterns, for 24 sources coming from all azimuths with epicentral distance between  $30^\circ$  to  $90^\circ$ .

polarities and positions in depths using the scattering patterns and their respective travel times computed with FM3D. Because the actual features are always focused at the same depth across all single scattering-mode images, they will sum up positively during the multi-mode migration. This is something we will exploit in the next section.

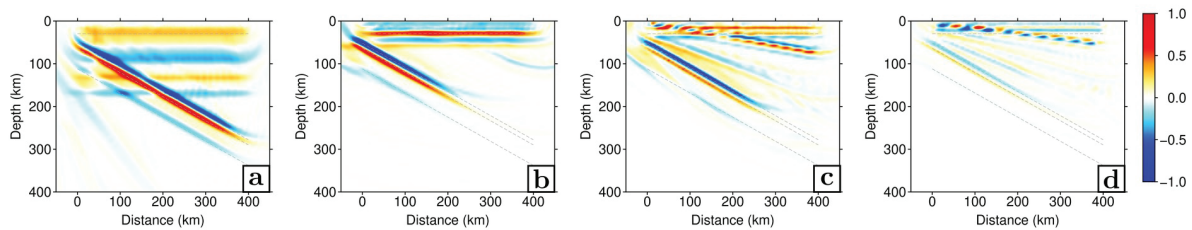
### 3.4 Stacking methods

We now test the three stacking methods introduced in Section 2.7 to see how well they enhance the coherent signals from the four single scattering-mode migrated images in figure 7. We consider one stacking method with no coherence filter (linear stacking, eq.(13)) and two stacking methods that incorporate coherence filters – phase-weighted stacking (phase coherence filter, eq.(16)) and 2<sup>nd</sup> root stacking (amplitude coherence filter, eq.(19)). The results are displayed in figure 8.

The first method we test is linear stacking (eq.(13), figure 8a), where we simply add the amplitudes of the four modes during the migration with no extra measure of coherence. The resulting amplitudes are then normalized to obtain the final image. Results show that the dipping interface is better imaged than in figure 7a. We note that the energy from spurious features is considerably reduced, but that they do not completely disappear. The three spurious streaks described in figure 7a are still present just under the actual discontinuity. We also see that there is more noise above the discontinuity than in figure 7a. In this case, the four modes have comparable amplitudes, and spurious features will only be reduced to about one fourth of their amplitude on a given scattering mode migration.

The second method we test is phase-weighted stacking and corresponds to the imaging principle in eq.(16). The results are shown in figure 8b. The resulting image exhibits fewer

### Individual scattering-mode migrations (Ps, PpP, PpS and PsS)



### Stacked multi-mode migrations (Linear, PWS, 2<sup>nd</sup> root)

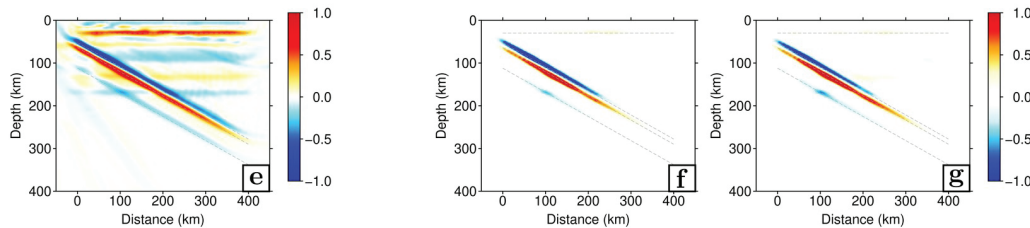


**Figure 9** – Single scattering-mode and multi-mode migrations for the 2.5D Subduction Zone (model R2DSZ, table 1). The upper 4 images (a=PS, b=PpP, c=PpS, d=PsS) are the 4 migrations for the 4 single-scattering modes (eq.(13)). The lower 3 images correspond to the linear (e, eq.(14)), phase-weighted (f, eq.(16)) and 2<sup>nd</sup> root (g, eq.(19)) stacked images.

artifacts than with the linear stack, as most spurious signals do not have a coherent phase over the 4 modes. The phase stack virtually acts as a filter applied to the linear amplitude stack, as the artifacts are at the same position in depth but their amplitude is even more reduced, representing less than 10% of their single-mode values.

Finally, the last method we test is 2<sup>nd</sup> root stacking and corresponds to the imaging principle in eq.(19). The results are shown in figure 8c. The image is very similar to figure 8b and has all the artifacts reduced to less than 10% of the actual discontinuity.

The test conducted in this section demonstrate that most artifacts can be eliminated by applying coherence filters based either on phase (phase-weighted stack) or amplitude (2<sup>nd</sup> root stack) in simple synthetic cases. We are now going to test these methods with a more complex synthetic model depicting an idealized subduction zone.

## 3.5 2.5D subduction zone

Here we show how our imaging principle can be used to improve interpretations in realistic settings. To do so, we design a synthetic subduction zone model, labelled R2DSZ in table 1, and analyse the migrated images obtained using eqs.(12), (13), (16) and (19). In this model, we have 4 different layers over a half-space with constant elastic properties and use a total of 24 sources equally spaced in back-azimuth with random epicentral distance

to the center of the array ranging between 30 to 90°. The array starts at lateral position 0km and covers 400km in length.

The results for the 4 single mode migrations are shown in figure 9a to 9d. Figure 9a shows the migration of the forward PS scattering mode. The single-mode migration is able to resolve the overriding Moho and the various dipping interfaces belonging to the oceanic lithosphere, but there are strong artifacts in the migrated image. In the right part of the image, we observe that for a simple 30 km deep Moho model, the free surface multiples can become predominant at around 100 km where one could interpret a spurious Lithosphere-Asthenosphere Boundary (LAB). Figure 9b shows the back-scattered PpP migration. The structure comes out more clearly because the PpP scattering mode is well isolated from the other phases – i.e., it is polarized mostly along the vertical component, in contrast to S-waves from the other scattering modes which are polarized mostly along the horizontal components. The results in figure 9c and 9d show the back-scattered PpS and PsS migration, respectively. Figure 9c exhibits clearly-defined structures corresponding to the Moho and the subducting slab. Figure 9d recovers the dipping interfaces well but shows only a very weak signal for the continental Moho. This is due to the resolution of the migration grid, which is too low (5km vertically) to image the highly vertically compressed signal of the PsS mode at the Moho level for a 1Hz synthetic Receiver Function. In addition, figures 9c-d also display some strong artifacts in the overriding mantle wedge, which correspond to the spurious migration of other slab conversions. The higher resolution of the back-scattered S modes is visible on these last two figures.

Overall, the 4 scattering modes produce a coherent view of the imaged medium. However, there are some notable differences between them. On one hand, the amplitudes of the shallow structures is stronger in images based on multiple modes than on those based on the direct mode. This can clearly be seen by comparing the PS and PpP images. On the other hand, the images based on multiple modes have less imaging power in the lower part of the image because phases reflected on the top of dipping interfaces at these depths are not recorded on the array and leave the imaged region. In each of these single-mode images, the specific scattering mode that is being processed is always migrated at the correct position, while the other modes are migrated as spurious features at different locations. Finally, we note that the signal of a discontinuity in a given mode can be affected by destructive interference with the projected signal from another discontinuity in another mode. This is best exemplified in the PpS and PsS images, where destructive interference between the continental Moho signal and the PS scattering from the subducting slab generate an apparent hole in the continental Moho even if it is a continuous feature.

The results for the 3 different stacking methods are displayed in figure 9e to 9g. Figure

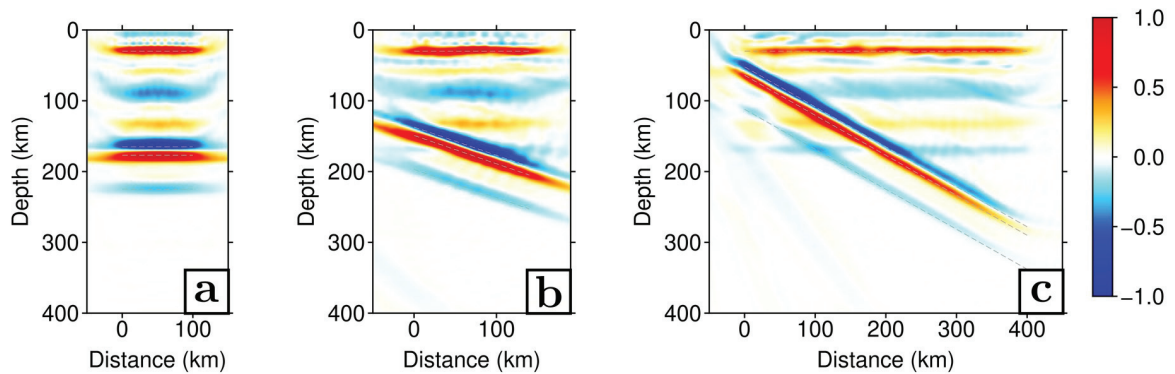


**Figure 10** – Off-dip profiles across the 3D migrated image of model R2DSZ. The imaging principle is the same as the linear multimode as in figure 9e (eq. (14)). The receiver array is 100km in the along-strike direction and 400km in the dip direction. Profiles are cut through the imaged volume at azimuths of (a)  $60^\circ$  – along-strike, (b)  $105^\circ$  – oblique and (c)  $150^\circ$  – dip. The imaging principle recovers the correct depths and dips of structures in all cases, regardless of orientation. Some artifacts can be seen in (b) and (c) at the continental Moho because of the interference with the PpP and PpS scattering modes from the dipping interfaces.

9e corresponds to the linear stack. It represents a considerable improvement over figure 9a, especially for the shallow structures. However, because the PS mode is dominating the final image, phases reflected at the continental Moho and migrated as PS transmissions are still visible. We also note that the contamination from free surface multiples for the dipping interfaces is strongly reduced. Figure 9f corresponds to the phase-weighted stack, which focuses the energy even more at the true location of discontinuities in the subducting slab. However, we note that the Moho is no longer visible. This is because the Moho is absent from the PsS migration, which leads to incoherent signals across the scattering modes, and subsequent down-weighting in the non linear stack. Nonetheless, there are no more visible artifacts in the rest of the image. Finally figure 9g corresponds to the 2<sup>nd</sup> root stack. This image is very similar to the phase-weighted migration, and the slab is recovered down to more than 200km depth.

The results in figure 9 prove that it is necessary to adopt a multi-mode migration strategy in order to avoid misinterpreting Moho multiples as a potential LAB. We also note here that the best imaged dipping interface is the subducting Moho, which corresponds to a 24% jump in seismic velocities. The top and bottom of the dipping slab correspond to 19% and 6% jump in seismic velocities respectively and are clearly visible in the Ps, PpP, PpS individual scattering modes and in the linear stack images. Conversely, the continental Moho suffers from the limited vertical resolution of this test setting. Being almost absent in the PsS migration, it is completely removed from the non linear stacks.

This can be mitigated by improving the vertical resolution of the migration grid at the expense of computation time.

Though our models are not truly 3D, we can still test the 3D capabilities of our method by investigating how it recovers structures for profiles that are not aligned with the dip direction. Methods that are purely 2D, such as the GRT and RTM, cannot recover the structure at oblique angles, because it effectively becomes a 3D problem (see, e.g., [Rondenay et al., 2010](#)). Figure 10 shows a series of profiles cut at various azimuths through our 3D image of R2DSZ. We find that the off-dip profiles recover the slab structure as well as the dip profile, confirming that our approach can handle 3D geometries, and that the recovered migration model is fully 3D.

The results from this section show that the imaging principles that we developed in section 2 are able to structure in both challenging and realistic settings provided that the vertical resolution is high enough. We tested the method with worst case scenarios with respect to polarity artifacts (WCS1) and strong free surface multiples (WCS2), as well as with a synthetic 2D subduction zone (R2DSZ). The data can be automatically processed with the scattering patterns on three components and the recovered model is fully 3D. This ensures maximum data coverage and allows for good focusing of the migrated energy along the scattering interfaces.

## 4 Application to field data and implications

We now apply the imaging principles to field data from the MEDUSA array in the Hellenic subduction zone ([Rondenay, 2006](#)). We will show that our method can retrieve the subsurface structure with fine details. Here we use a 1D reference velocity model, even though our method is capable of handling a 3D model, because we want to replicate the GRT images from [Pearce et al. \(2012\)](#) which were obtained with the same dataset.

### 4.1 Hellenic field data

The Hellenic subduction system represents an ideal laboratory to investigate the complex mechanisms that control oceanic and continental subduction. It spans 1300km from the south-eastern tip of Puglia in Italy to the region of Antalya in Turkey and has a convergence rate of 4mm/yr. In this work, we aim to investigate the structure of the subducting slab in the Western Hellenic Subduction Zone (WHSZ). This is the part of the subduction system that surrounds mainland Greece and the Peloponnese region from the West before transitioning into the Southern Hellenic Subduction Zone offshore Crete.

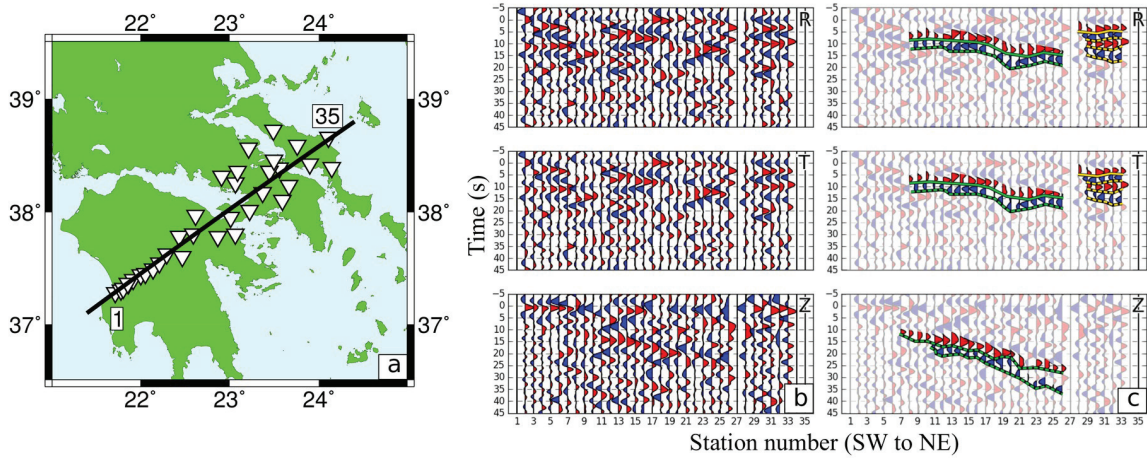


**Figure 11** – Setup, raw and interpreted data from the MEDUSA experiment (Pearce et al., 2012). (a) corresponds to the array setup, with white triangles representing the stations position from 1 (south-western corner) to 35 (north-eastern corner) and the projecting line in solid black. (b) is the data for one event sorted by station number. (c) is the interpreted data where we highlight the presence of the continental Moho (orange) and the subducting slab (green). We differentiate between the forward conversions (solid lines) from the free surface multiples (dashed lines).

Both oceanic and continental subduction coexist in the WHSZ and the link between the two systems has only been partially explained so far. Previous studies have shown that the convergence rates and slab retreat behavior strongly depend on the slab composition (Papanikolaou and Royden, 2007). The slab composition and water content also influence the hydration of the mantle wedge and the volcanic activity in the region, which have been studied structurally and geochemically (Pe-Piper and Piper, 2007). Complementary geophysical methods such as long period magnetotellurics (MT) have found potential fluid pathways, emerging both from the upper part of the slab and deeper portions of the subduction (Galanopoulos et al., 2005; Tzanis et al., 2018).

The data that we use in this application comes from the Multidisciplinary Experiments for Dynamic Understanding of Subduction under the Aegean Sea (MEDUSA) project, which was carried out across the Western Hellenic Subduction Zone (Pearce et al., 2012). This experiment had two seismic lines deployed. The first line was in the northern part of the region, spanning roughly from Corfu to Thessaloniki, and was aimed at studying the continental subduction. The second line was deployed in the southern part of the region and targeted the oceanic subduction under the Peloponnese and across the gulf of Corinth. Here, we take the data from the southern Line (SL) to test our imaging principle.

The data along this line is of higher quality than the northern line and the images display clearer features (Pearce et al., 2012). The station distribution is shown in figure 11a.

The direct and scattered wavefields are estimated using a multichannel approach on the three dimensional P-wave as described in section 2. The dataset consists of 52 events recorded at 35 temporary stations over the course of 1.5 years, with a total of about 1500 waveforms available. The maximum frequency of the data is 0.5hz.

The data is selected on an event by event basis based on visual inspection of single-event migration results. We analyze the 52 single-event images and reject data in two cases. First, we reject events when the migrated images display only horizontal streaks with a single main frequency. In the data space, this corresponds to traces dominated by unwanted oscillations, most likely linked to the deconvolution. Second, we reject events when the migrated images are dominated by southward dipping discontinuities, as it is the opposite behaviour to northwards dipping subduction that we are imaging. Based on this selection scheme, we retained 32 high-quality events for the final migration.

In their paper, Pearce et al. (2012) migrated the data using a GRT method that shares some similarities with our method but is limited to 2D geometries (Bostock et al., 2001). Using data from their study, we have reproduced the single scattering and multi-mode GRT images of Pearce et al. (2012). They are shown in figure S2 from the supplementary information. The multi-mode image shows a clear Moho in the overriding plate, as a continuous interface that smoothly dips south-westwards from 30 to 40km depth. It also shows clear signals from both the upper and lower limits of the subducting crust, which dips north-eastwards at  $17^\circ$  down to about 100km depth. In order to better compare our 3D images to previously published 2D results, we alter the original station distribution by projecting their location on the migration line used by Pearce et al. (2012). Note that there is an equivalent step in the GRT preprocessing (Rondenay et al., 2001).

Raw and interpreted data from a single event, filtered at 0.1Hz, are displayed in figure 11b and 11c. In the north-eastern (stations 28 to 35) part of the section we observe signals corresponding to the overriding Moho and its free-surface multiples on the radial and transverse components at around 3 to 15 seconds delay. The PS conversion from the slab are visible at 5 to 10 seconds delay on the radial component. Strong signals from multiples on the vertical component are visible at 10 to 30 seconds delay on stations 2 to 26.

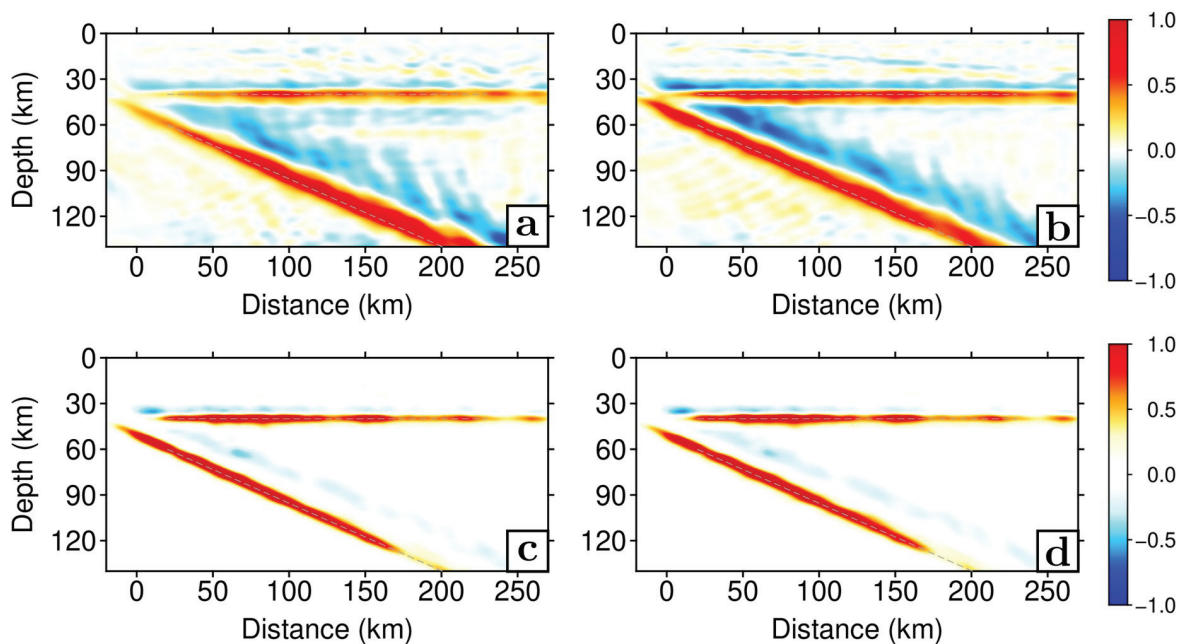


**Figure 12** – Resolution test with a 3 layer synthetic model for the geometry source distribution of the MEDUSA experiment. Panel (a) shows the linear multi-mode migration with original station geometry. Panels (b)-(d) are the linear, phase-weighted and 2<sup>nd</sup> root multi-mode stacks with data projected on the migration line, respectively (i.e., eqs.(14),(16),(19), see text).

## 4.2 Resolution test

In order to determine how well our method will be able to perform with this dataset, we first perform a synthetic resolution test on a 2D subduction model. We generate data for all 52 events recorded at a 35 stations setup corresponding to the MEDUSA South Line. The results will be used to determine the maximum resolution we can achieve given the data coverage, maximum frequency and station distribution. In order to better compare our image with GRT or RTM migrations, we project the locations of stations on the imaging line as previously stated.

To perform this test, we design a three layer reference model described in table 1 as MRT. The first layer is the 40km thick overriding crust, then there is a 10% velocity increase at the Moho and another 10% velocity increase at the slab interface. Since the amplitude of the velocity jump is similar for the two interfaces, we expect the two interfaces to show the same scattering potential on the final image. The data are generated with the Raysum code, and has a dominant frequency of 0.3Hz. This corresponds to wavelengths up to 20km for P-waves and 10km for S-waves, so for the resolution test and the real data we use a  $2 \times 2 \times 2$ km voxel size. Because the back-scattered S-wave multiples have shorter wavelengths in the model space, we allow for the data to be migrated in different



frequency bands for the various scattering (see, e.g., [Tauzin et al., 2016](#)). With an average station spacing of just under 10km, a 40km deep Moho should be easily retrievable.

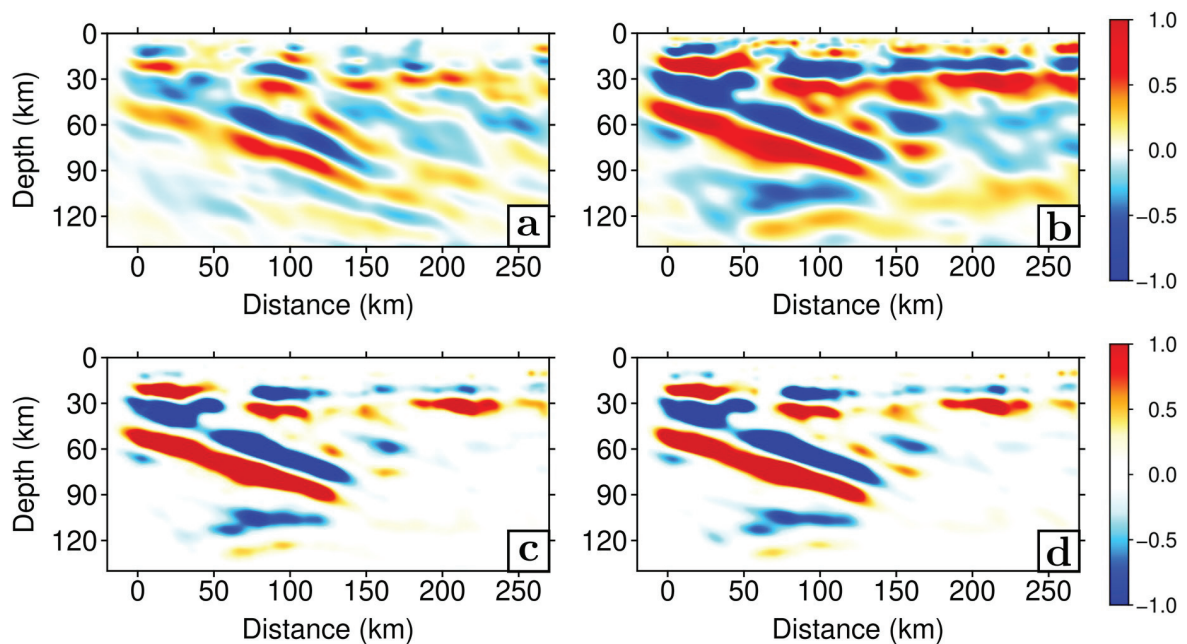
Results for this synthetic resolution tests (with same frequency range for all modes) are presented in figure 12. Figure 12a shows the result for the fully 3D imaging principle in eq.(13), without projecting the stations on the migration line. The energy focuses on the discontinuities, but there are some small coherent artifacts under the Moho with both negative (55km depth) and positive (65km depth) energy values. The features are retrieved at their correct positions but there are along-profile heterogeneities introduced by the uneven spatial distribution of stations. We individually down-weight the stations that are closer together in an effort to normalize the energy content across the image.

Figure 12b shows the result for the linear multi-mode stack with the array projected on the migration line and with individual station weights. The discontinuities are highlighted more finely with less along-dip variations. Nevertheless, some artifacts still remain, especially around the overriding Moho. Figure 12c shows the result for the phase-weighted stack from eq.(16) with station weights and station projection. There are fewer artifacts around the Moho than with the linear stacking. Figure 12d shows the result for the 2<sup>nd</sup> root stacking with the individual station weights and station projection. Here also there are practically no artifacts left in the vicinity of both the overriding Moho and the subducted slab.

This synthetic example shows that our method is capable of retrieving subsurface structure from an experimental setup such as that afforded by MEDUSA. The three stacking methods produce robust results and are efficient at removing most of the spurious energy from the final image. We expect to retrieve both flat and dipping discontinuities in the data and are confident that we can recover the structure properly in the field data using the multi-mode algorithm.

### 4.3 Field data migrated sections

The migrated sections for the MEDUSA data are presented in figure 13 (see figure S2 from the supplementary information for the single mode unstacked images). The background velocity model for the migration is the same 1D model as that used by [Pearce et al. \(2012\)](#) and is described in table 1 as MPKDM. We apply the following treatment to the data to enhance the imaging quality. We filter the data in different frequency bands to account for the difference in resolution power between the four modes ([Tauzin et al., 2016](#)). This helps to maximize the coherence on the final images. We filter the data between 0.03Hz and 0.5Hz for the PS and PpP data and between 0.03Hz and 0.3Hz for the PpS and PsS



**Figure 13** – Images obtained with the multi-mode migration on the MEDUSA experiment dataset (Pearce et al., 2012). Panel (a) shows the linear multi-mode migration with original geometry. Panels (b)-(d) show the linear, phase-weighted and 2<sup>nd</sup> root multi-mode stacks with data projected on the migration line, respectively (i.e., eqs.(14),(16),(19), see text). The overriding Moho, the subducting crust upper and lower limits are clearly imaged.

data. As we showed in the resolution test, we obtain the best images when we apply a weight that takes into account inter-station spacing. Therefore, we down-weight the data from the stations that are closer together to homogenize the energy content on the cross-section in figure 13b to 13d.

The results obtained with the different stacking methods are comparable overall with previous results from, e.g., Pearce et al. (2012). Two main features can be observed in the migrated sections: (1) a 25-35 km deep (from NE to SW) overriding Moho; and (2) a 12km thick, 18° north-eastwards dipping subducted crust. The Moho signal disappears close to the slab interface, whereas the subducting crust signal disappears at 85km for the upper limit and 100km for the lower limit. The strong similarities between our images and those of Pearce et al. (2012) can be attributed, at least in part, to the fact that the two methods share exactly the same pre-processing steps. This results in identical geometrical setups and datasets prior to filtering and application of the wavelet shaping factor.

We shall now describe each image individually, starting with figure 13a. The first image shows the linear multi-mode stack for the initial fully 3D geometry, similar to figure 12a. Here the overriding Moho and the subducting crust are visible but the image

is noisy. Next, figure 13b shows the result for the linear stack with data that has been projected on the migration line and with the individual station weights, similar to figure 12b. In this case the overriding Moho clearly appears as a linear feature and much of the noise has disappeared. The slab signature is also more consistent than on figure 13a, with a constant thickness. We can see a gap in the overriding Moho very close to where it intersects the dipping slab. This gap can be partially explained by the interference between the signals from the overriding Moho and the top of the slab in different migration modes, as stated in section 3.5. Lastly, figure 13c and 13d show the results for the phase-weighted stack and 2<sup>nd</sup> root stack, respectively. Colors have been saturated to emphasize the coherent structure. The two images are very similar. The signature of the overriding Moho is intermittent across these profiles. At greater depth, the bottom and top of the subducting crust are clearly isolated from their surroundings and there is less noise in the slab. The dipping signal is probably lost at depth due to eclogitization, as explained by Pearce et al. (2012). We acknowledge that we cannot interpret amplitudes in terms of velocity contrast  $\delta\beta/\beta$  in the images generated by our method. However, we find that the three main discontinuities, namely the top of the subducting crust, the slab Moho and the overriding Moho, have approximately the same scattering potential in our images. This roughly translates into the same changes in elastic properties, which is consistent with the previous GRT images (Pearce et al., 2012).

## 5 Discussion: Advantages and drawbacks of the method

In this paper, we presented a new, fully 3D prestack migration method, and demonstrated its applicability through a set of synthetic examples and a field case study. Here we will shortly discuss the advantages and drawbacks of our method compared to other imaging approaches based on scattered teleseismic waves.

### 5.1 Scattering potential vs elastic perturbations

Our method projects and stacks teleseismic waveform data in the depth domain to recover scattering structure. Other methods have the same basic principle, ranging from fast 1D CCP stacking (Dueker and Sheehan, 1997) to 2D multi-mode CCP (Tauzin et al., 2016) and 3D pre-stack techniques (Hansen and Schmandt, 2017, this paper). All these methods afford very high spatial resolution corresponding to one wavelength  $\lambda$  for PS scattering and  $\lambda/2$  for multiple modes, and pre-stack techniques are able to image structures as shallow as 2 times the inter-station spacing down to approximately the same depth as the array

aperture (Miller et al., 1987; Rondenay, 2009). These methods have high spatial resolution but all suffer from the fact that they provide information only about the location of the scatterers, not about their elastic perturbations.

In order to obtain high resolution elastic parameter perturbations, some authors combined pre-stack imaging methods, which have high spatial resolution, and inversion schemes that allow to distinguish density from velocity and access elastic parameters perturbations. Methods like the GRT migration (e.g., Bostock et al., 2001) recover these perturbations across scattering interfaces using linearized inversion techniques. Other methods like RTM rely on wavefield reconstruction across the whole study area for both the upgoing and reflected scattering modes. This requires accurate and expensive interpolation of the data into the model. The drawback with these methods is that they are computationally expensive and that the inversion steps require dense data coverage on all arrival geometries – i.e., comprehensive ray coverage over a slowness hemi-circle in 2D and a slowness $\times$ back-azimuth hemisphere in 3D. These two factors limit these methods mostly to 2D applications, while our method allows us to move to 3D migration.

Migration methods such as ours can be complemented by pure inversion approaches, which use the data to create a model parameterized in terms of elastic perturbations and go beyond the stacking offered in classic migration. Scattered waveforms can be used in expensive full waveform inversion schemes where the wave equation is solved in 3D (P-wave coda waveform inversion, Frederiksen and Revenaugh, 2004). However, these are very expensive and do not provide the high resolution power of migration methods, as they are often mixed-determined problems that require regularization, which reduces their resolution power. Another way to use the scattered data is in joint inversions with surface waves and other body waves (e.g., Bodin et al., 2016) using a fully non-linear Bayesian inference. This allows to estimate precise uncertainties about the elastic and structural parameter variations, but extensive model sampling has limited its application to 1D structure so far.

## 5.2 3D seismic imaging

In order to obtain high signal-to-noise ratio and interpret scattered data, migration methods require a large number of waveforms to be stacked. In CCP stacking, the waveforms are first stacked according to their incoming geometry and then projected in the depth domain, which effectively collapses the 3D data on a horizontally layered 1D profile. Including lateral variation effects back in the waveform stacking can be partially addressed by performing wavenumber filtering or designing 2D migration schemes (Chen et al., 2005;

Tauzin et al., 2016; Burdick et al., 2013; Bostock et al., 2001). 3D elastic parameter variations can be treated to first order by computing the arrival times or full waveforms in a 3D reference model. However there will always be some contamination if there are large lateral variations in structure or elastic properties.

Our method is a 3D pre-stack migration, which works in the opposite way to CCP stacking. In our case, projecting the data independently before the final stacking allows to preserve the 3D effects, and thus avoids to make any assumption about the scattering structure that we want to image. In this way, our method exhibits close to no artifacts when dealing with dipping interfaces and laterally varying media, and thus performs generally better than classic CCP stacking (Cheng et al., 2016). The drawback is that not using the horizontal interface assumption to stack all the traces slows down the depth mapping of the scattering information (Dueker and Sheehan, 1997). In this regard our method is very close to GRT migration. However, the dense data coverage required in GRT to perform a stable and meaningful inversion of elastic parameters is not required here as we simply migrate the scattering potential. This allows our method to be correctly applied in 3D even without optimal data coverage.

Adapting Kirchhoff migration into migration and inversion schemes for passive seismology has been pioneered and improved in the last 20 years (Sheehan et al., 2000; Ryberg and Weber, 2000; Levander et al., 2005; Wilson and Aster, 2005). However, none of those methods have attempted fully 3D migration as computation time has always been a hurdle. Wilson and Aster (2005) for example computed the arrival times in a one 1D reference velocity model to speed up computations. The final step towards fully 3D migration was taken by introducing 3D wavefront calculation (Cheng et al., 2016), but this method was only very recently extended to fully 3D by applying the fully 3D scattering patterns (Hansen and Schmandt, 2017, this paper). In our implementation of the Kirchhoff imaging principle, by computing the arrival times with a fully 3D scheme, we do not hinder our capacity to tackle even the strongest 3D effects. This is done at the expense of some computational efficiency, but the overall cost is reduced by the introduction of the fast marching method (FM3D, de Kool et al., 2006).

### 5.3 Scattering patterns

CCP analysis uses only a small part of the scattered wavefield, usually either the radial or the Q component of the RF, as they are the only components that are sensitive to scattering under the horizontal interface assumption. This usually produces good first-order images. However, in the case of dipping discontinuities, a lot more information

about subsurface structure may be gained from multiple component analysis (Tonegawa et al., 2008). Our method uses three-component RFs, similarly to inversion methods that use this multi-component data RFs to reconstruct the 2D or 3D wavefield and elastic perturbations. However, one has to be especially careful about the polarity issues that come with scattering on dipping discontinuities.

Taking the physics of scattering into account to deal with the polarity issues is what allows this step up in imaging quality. For waveform inversion methods this is done by solving the wave equation in 3D, which is expensive. In our method, this is done through the use of scattering patterns. We separate the calculation of the phase (travel times), that we obtain by running the FM3D software, from the calculation of the amplitudes, estimated using precise scattering geometry and scattering patterns, to avoid having to solve the wave equation in 3D. This way of computing scattering intensities is similar to what is done in GRT, and is faster than full-wavefield computations used in RTM methods. Also, by using fully 3D scattering patterns, as opposed to their projection in 2D, we can treat all scattered phases, including  $S_V$ -to- $S_V$  and  $S_H$ -to- $S_H$  scattering.

As shown in section 2, the use of scattering patterns allows us to automatically process data from all slownesses and back-azimuth without worrying about polarity and amplitude issues. Methods that do not take scattering patterns into account, such as CCP stacking and 1D inversions have to carefully select data to avoid these issues. This results in more data rejection and thus lower data coverage.

## 5.4 Multi-mode and stacking schemes

Other authors have implemented approaches that migrate multiple modes of teleseismic scattering (Bostock et al., 2001; Wilson and Aster, 2005; Tauzin et al., 2016). As shown in section 3, taking not only the PS mode into account, but also the PpP, PpS and PsS modes, largely improves the imaging quality. In addition to enhancing the data coverage with new ray paths, extracting the information from individual modes and comparing images across modes allows to discriminate between real and spurious structures. We demonstrated, for example, that multi-mode migration is a powerful tool to avoid misinterpreting a spurious LAB. Multi-mode algorithms have been devised for numerous migration methods and consistently show clear improvements both in synthetic and field data applications (see e.g., Tauzin et al., 2017).

One of the drawback in using the multiples in the migration scheme is the additional time required to migrate this data. In practice however, many of the calculations for a given scattering mode can be used in the other modes. In our case, we use four different

modes and three independent stacking methods but the migration only takes about twice as long as the PS migration alone.

Combining the information extracted from all the scattering modes by stacking the images linearly is an efficient tool to extract coherent information (Bostock et al., 2001; Hansen and Schmandt, 2017). In the case of GRT, the PS, PpS and PsS modes are combined to create a composite result for  $\delta\beta/\beta$  variations and the PpP mode gives the result for the  $\delta\alpha/\alpha$  variations. In our case, as we cannot easily extrapolate the results to elastic parameter variations, we stack all four modes together to get a single final image (figs 8a, 9e, 11a-b and 12a-b). Our examples confirm that linear stacking of scattering potential offers a significant advantage over PS migration alone, as the resolution power for the multiples is higher and the combination of  $\alpha$  and  $\beta$  variations helps clearly underline the structures.

Going past linear stacking, we explored a number of non-linear stacking strategies for multi-mode data, as originally proposed by Tauzin et al.(2017) for multi-mode CCP imaging. We first implemented a phase-weighted stack where the complex phase of our RF signals is first migrated independently from the amplitudes and then applied as a coherence filter to the amplitude image. This generates a joint coherence map of all the modes that removes the spurious signals and enhances the coherent scattering. Then we implement a 2<sup>nd</sup> root stack where square-root amplitudes for all modes are migrated together before taking the whole stacked field to the power of 2. This allows smaller coherent scattering signal to reach higher amplitudes on the final migrated image while also efficiently removing the larger incoherent peaks across all modes. We proved that both stacking methods are very efficient at removing incoherent features across modes, and that even though they act on a fundamentally different level, they have very similar stacking capabilities. They allow to nearly completely reject information that is present on only one mode, and maximum stacking is reached for features that are coherent on at least three modes.

## 5.5 Towards fully 3D settings

Our application to field data consists of a 1D array and a 2D slice, therefore it does not showcase the benefit of our fully 3D approach. We acknowledge here that the full potential of our method in 3D is yet to be demonstrated. However, there are two encouraging points that validate the potential of our method. First, we show that when performing the same processing to the data as for 2D GRT, we get a similar image with our fully 3D imaging principle. This demonstrates that our method is *a minima* as powerful as the GRT

migration to image the underlying structure of subduction zones in terms of scattering potential. Second, we show in figure 12a and figure 13a that by using the original station distribution, which deviates slightly from a 1D array, we can still recover the main features observed by authors of previous studies in the region.

## 6 Conclusions

In this study, we designed a new method to migrate teleseismic Receiver Functions and recover the three dimensional distribution of scattering structure in the subsurface. In order to overcome the drawbacks of both fast CCP methods (which rely on the assumption that the underlying discontinuities are horizontal), and complex Reverse-Time Migration or Generalized Radon Transform migrations (which are too computationally expensive to be run in fully 3D settings), we designed a new, computationally-efficient and fully-3D multi-mode Kirchhoff migration approach.

We adapted the Kirchhoff method from reflection to transmission scattering and applied it to passive seismic data. We expanded the work done by Cheng et al. (2016) to include three component data and free-surface multiples into an efficient multi-mode migration by computing the travel times for all scattered phases using the FM3D software. We use three-component RFs, 3D scattering patterns and coherence filters to extract the information from the data.

Our method was tested in challenging and realistic synthetic scenarios, using the Raysum package. It recovers scattering structures with minimal artifacts in all tested cases, and allows to take lateral heterogeneities into account with reasonable computational time. Our fully 3D method has a similar cost to 2D GRT.

Using data from the MEDUSA experiment in the Hellenic subduction zone, we show that our method performs correctly on field data as well. The images we obtain are similar to the ones obtained with a 2D GRT migration and serve as a benchmark for our imaging method. We believe that the passive multi-mode 3D Kirchhoff migration method will prove useful in complex settings where lateral variations play a large role.

## Acknowledgements

We want to thank Jean Virieux and Benoit Tauzin for helpful discussion about the methodological developments and Hellenic Subduction Zone image interpretation respectively. We also thank two anonymous reviewers and the Associate editor for their comments, which helped improve and clarify the manuscript. This work was funded by the



European Union’s Horizon 2020 research and innovation programme under Grant Agreement No. 716542, and by the Research Council of Norway via the project “Subduction zone Water and Metamorphism: A Modelling and Imaging Study” (project 231354). All data can be found on the Incorporated Research Institutions for Seismology (IRIS) Data Management Center, and at <https://doi.pangaea.de/10.1594/PANGAEA.901308> for the deconvolved receiver functions used in this study.

# Supporting Information for "Multi-Mode 3D Kirchhoff Migration of Receiver Functions at Continental Scale"

## **Contents of this file**

1. Tables S1 to S2
2. Figures S1 to S2

## **Introduction**

The supplementary information presents the stations and event used for the migration, as well as some complementary tests and images. The data is available for download at the IRIS DMC website or directly at Pangaea (soon). We also reproduce the images for the single mode GRT migrations using the data from Pearce et al. (2012) to plot them alongside our results for easier comparison.

**Table S1** – Stations used in the migration. Most stations were recording between June 2006 and October 2007. They correspond to the South Line of the MEDUSA deployment (DOI: 10.7914/SN/XS\_2006).

Name	Number	Latitude	Longitude	Elevation (km)
XS-S001	1	37.283	21.718	0.156
XS-S002	2	37.306	21.782	0.241
XS-S003	3	37.321	21.808	0.537
XS-S004	4	37.361	21.864	0.813
XS-S005	5	37.4	21.919	0.703
XS-S006	6	37.442	22.004	1.035
XS-S007	7	37.454	22.055	0.565
XS-S008	8	37.495	22.142	0.839
XS-S009	9	37.548	22.212	1.174
XS-S010	10	37.629	22.295	1.082
XS-S011	11	37.606	22.47	0.815
XS-S012	12	37.786	22.434	0.753
XS-S013	13	37.806	22.593	0.451
XS-S014	14	37.783	22.868	0.519
XS-S015	15	37.972	22.618	0.947
XS-S016	16	37.805	23.064	0.832
XS-S017	17	37.954	23.012	0.234
XS-S018	18	38.015	23.224	0.548
XS-S019	19	38.259	23.065	0.252
XS-S020	20	38.318	22.91	0.753
XS-S021	21	38.361	23.089	0.287
XS-S022	22	38.174	23.37	0.526
XS-S023	23	38.105	23.592	0.238
XS-S024	24	38.362	23.447	0.235
XS-S025	25	38.566	23.213	0.301
XS-S026	26	38.391	23.559	0.18
XS-S027	27	38.237	23.666	0.474
XS-S104	28	37.366	21.859	0.654
XS-S124	29	38.362	23.447	0.238
XS-S030	30	38.395	24.145	0.197
XS-S031	31	38.426	23.899	0.152
XS-S032	32	38.591	23.758	0.203
XS-S033	33	38.723	23.491	0.25
XS-S126	34	38.46	23.497	0.964
XS-S035	35	38.661	24.108	0.33

**Table S2** – Events used in the migration. Good quality corresponds to three or four modes being used in the migration, medium only one or two modes and for bad quality events no data was used.

Date (Julian)	Latitude	Longitude	Depth (km)	Quality
2007 008 12:48	8.077	92.437	11	bad
2006 364 08:30	13.313	51.365	15	good
2006 360 12:26	21.799	120.547	10	good
2006 351 21:10	4.815	95.018	36	good
2006 341 19:10	46.153	154.386	16	bad
2006 335 03:58	3.39	99.079	204	good
2006 321 18:03	28.591	129.895	22	good
2006 282 10:01	20.654	120.023	14	good
2006 273 17:50	46.351	153.166	11	bad
2006 273 12:47	7.283	-34.658	10	bad
2006 272 13:08	10.876	-61.756	53	bad
2006 267 22:56	-17.741	41.811	6	good
2006 236 21:50	51.148	157.522	43	good
2006 232 03:01	49.823	156.415	26	good
2006 229 15:20	46.542	141.908	14	good
2006 210 19:53	23.589	-63.923	10	good
2006 208 11:16	1.707	97.146	20	good
2006 189 20:40	51.214	-179.312	22	good
2006 173 10:53	45.417	149.343	95	medium
2006 169 18:28	33.028	-39.702	9	good
2007 275 18:00	54.511	-161.708	32	good
2007 263 08:31	-1.999	100.141	30	bad
2007 257 06:01	-4.075	101.169	23	good
2007 232 22:42	8.037	-39.251	6	good
2007 232 12:37	-0.256	-18.175	10	good
2007 220 17:05	-5.859	107.419	280	good
2007 212 22:55	-0.162	-17.795	11	good
2007 211 22:42	19.311	95.611	14.2	bad
2007 210 04:54	53.641	169.702	25.7	good
2007 198 14:10	-2.734	36.362	8	bad
2007 197 01:13	37.535	138.446	12	bad
2007 184 08:26	0.715	-30.272	10	good
2007 166 18:49	1.719	30.834	24	medium
2007 153 21:34	23.028	101.052	5	medium
2007 150 20:22	52.137	157.293	116	bad
2007 143 04:41	52.352	-31.814	10	good
2007 125 08:51	34.248	81.967	9	bad
2007 124 12:06	-1.41	-14.921	7	good
2007 119 12:41	52.007	-179.972	117	good
2007 110 19:37	27.471	128.379	42.4	bad
2007 110 01:45	25.71	125.108	9	bad
2007 097 07:09	37.306	-24.494	8	good
2007 095 03:56	37.306	-24.621	14	bad
2007 093 03:35	36.451	70.688	222.1	good
2007 087 21:17	-6.268	29.673	8	good
2007 084 00:41	37.336	136.588	8	bad
2007 068 03:22	43.224	133.526	441.2	good
2007 065 05:49	-0.488	100.53	11	bad
2007 048 00:02	41.794	143.553	31	bad
2007 017 23:18	10.125	58.708	8	good
2007 009 15:49	59.42	-137.118	10	good
2007 008 17:21	39.803	70.312	16	good

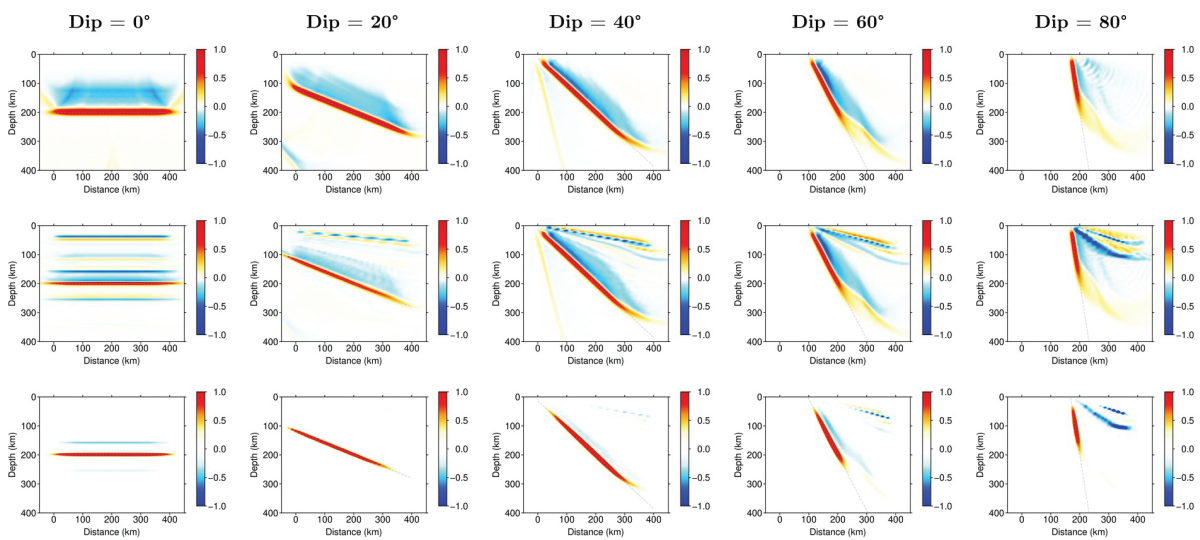


**Figure S1** – Dip resolution test for the 3D Kirchhoff migration. From left to right by  $20^\circ$  increments from horizontal. From top to bottom PS migration, Linear Multi-Mode stack and  $2^{\text{nd}}$  Root stack. Dips are correctly recovered in all modes up to  $40^\circ$ . For  $60^\circ$  and  $80^\circ$ , the free surface multiples escape the imaging region, therefore limiting the multi-mode stacking capabilities. Also for those high dip angles, the number of stations that actually record scattering rather than pure transmission shrinks. PS correctly images very high dips up to depth that correspond to half of the arrays aperture, here 200km depth for a 400km aperture.

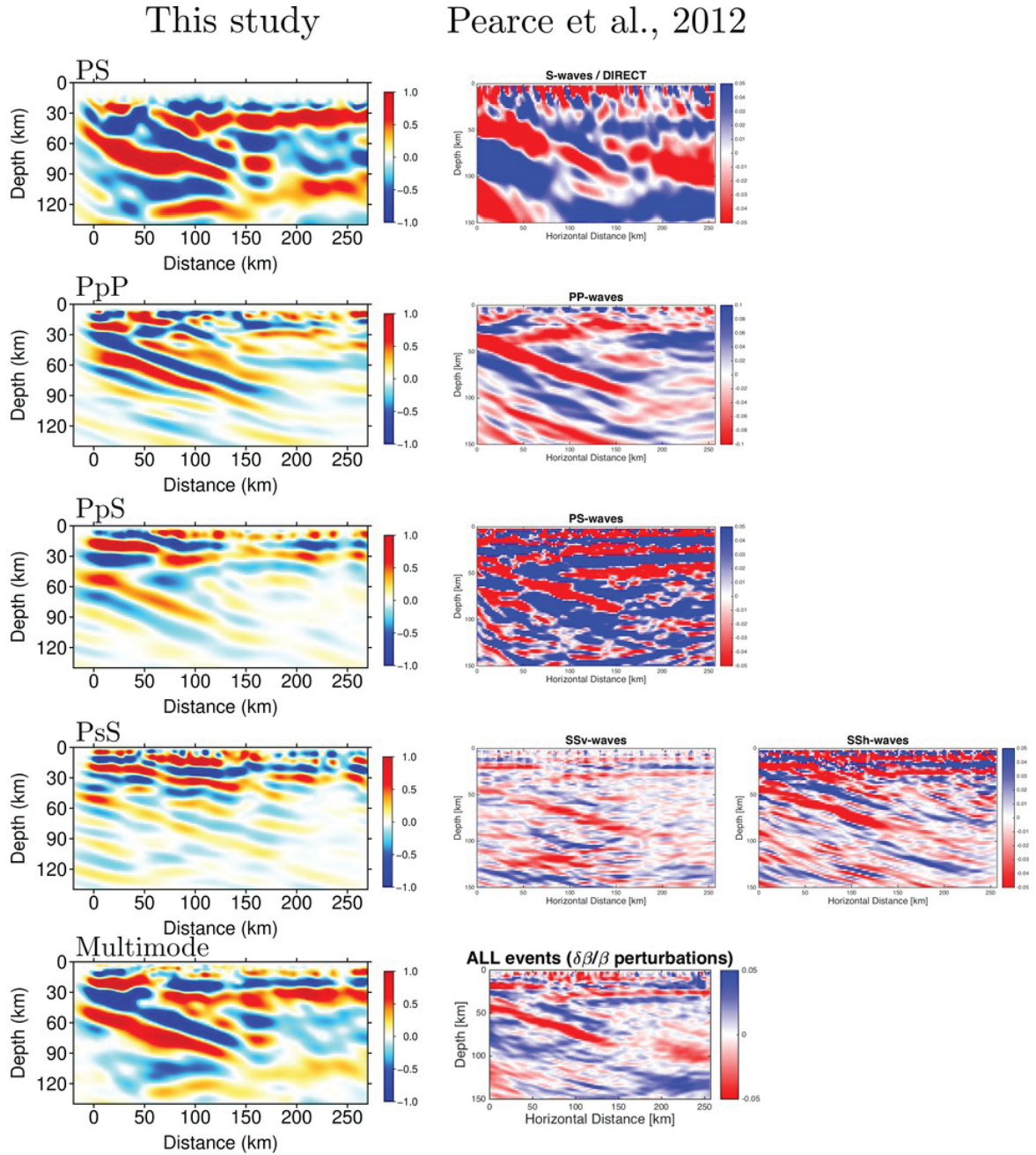


**Figure S2** – Individual and linear multi-mode migrations. Left is the 3D Kirchhoff migration from this study. Right are the results from Pearce et al., 2012 using a GRT inversion. The pre-processed data used is the same up to the selection criteria and filters, which are different.



# Bibliography

- Abers, G. A., MacKenzie, L. S., Rondenay, S., Zhang, Z., Wech, A. G., and Creager, K. C. (2009). Imaging the source region of Cascadia tremor and intermediate-depth earthquakes. *Geology*, 37:1119–1122.
- Beylkin, G. and Burridge, R. (1990). Linearized inverse scattering problems in acoustics and elasticity. *Wave Motion*, 12:15–52.
- Bodin, T., Leiva, J., Romanowicz, B., Maupin, V., and Yuan, H. (2016). Imaging anisotropic layering with bayesian inversion of multiple data types. *Geophysical Journal International*, 206:605–629.
- Bostock, M. and Rondenay, S. (1999). Migration of scattered teleseismic body waves. *Geophysical journal international*, 137(3):732–746.
- Bostock, M., Rondenay, S., and Shragge, J. (2001). Multiparameter two-dimensional inversion of scattered teleseismic body waves 1. Theory for oblique incidence. *Journal of Geophysical Research: Solid Earth*, 106(B12):30771–30782.
- Burdick, S., de Hoop, M., Wang, S., and van der Hilst, R. (2013). Reverse-time migration-based reflection tomography using teleseismic free surface multiples. *Geophysical Journal International*, 196(2):996–1017.
- Chen, C.-W., Miller, D. E., Djikpesse, H. A., Haldorsen, J. B. U., and Rondenay, S. (2010). Array-conditioned deconvolution of multiple-component teleseismic recordings. *Geophysical Journal International*, 182:967–976.
- Chen, L., Wen, L., and tianyu Zheng (2005). A wave equation migration method for receiver function imaging: 1. Theory. *Journal of Geophysical Research*, 110:1–15.
- Cheng, C., Bodin, T., and Allen, R. M. (2016). Three-dimensional pre-stack depth migration of receiver functions with the fast marching method: A Kirchhoff approach. *Geophysical Journal International*, 205:819–829.
- Cheng, C., Bodin, T., Tauzin, B., and Allen, R. M. (2017). Cascadia subduction slab



heterogeneity revealed by three-dimensional receiver function Kirchhoff migration. *Geophysical Research Letters*, 44:694–701.

Claerbout, J. F. (1985). *Imaging the Earth's Interior*.

Cooper, G. R. J. (2009). Stacking phase coherent signals. 10th SAGA Biennial Technical Meeting and Exhibition.

Costa, J. C., Medeiros, W. E., Schimmel, M., Santana, F. L., and Schleicher, J. (2018). Reverse time migration using phase cross-correlation. *Geophysics*, 83:1–65.

Cottaar, S. and Deuss, A. (2016). Large-scale mantle discontinuity topography beneath Europe: Signature of akimotoite in subducting slabs. *Journal of Geophysical Research: Solid Earth*, 121:279–292.

de Kool, M., Rawlinson, N., and Sambridge, M. (2006). A practical grid-based method for tracking multiple refraction and reflection phases in three-dimensional heterogeneous media. *Geophysical Journal International*, 167(1):253–270.

Dueker, K. and Sheehan, A. (1997). Mantle discontinuity structure from midpoint stacks of converted P to S waves across the Yellowstone hotspot track. *Journal of Geophysical Research: Solid Earth*, 102(B4):8313–8327.

Frederiksen, A. W. and Bostock, M. G. (2000). Modelling teleseismic waves in dipping anisotropic structures. *Geophysical Journal International*, 141:401–420.

Frederiksen, A. W. and Revenaugh, J. (2004). Lithospheric imaging via teleseismic scattering tomography. *Geophysical Journal International*, 159:978–990.

Galanopoulos, D., Sakkas, V., Kosmatos, D., and Lagios, E. (2005). Geoelectric investigation of the Hellenic subduction zone using long period magnetotelluric data. *Tectonophysics*, 409:73–84.

Hansen, M. S. and Schmandt, B. (2017). P- and S-wave receiver function imaging of subduction with scattering kernels. *Geochemistry Geophysics Geosystems*, 18:4487–4502.

Langston, C. (1979). Structure under Mount Rainier, Washington, inferred from teleseismic body waves. *Journal of Geophysical Research: Solid Earth*, 84(B9):4749–4762.

Lekić, V. and Fischer, K. M. (2013). Contrasting lithospheric signatures across the western United States revealed by Sp receiver functions. *Earth and Planetary Science Letters*, pages 1–13.

Levander, A. and Miller, M. S. (2012). Evolutionary aspects of lithosphere discontinuity structure in the western U.S. *Geochemistry Geophysics Geosystems*, 13:1–22.

- Levander, A., Niu, F., and Symes, W. W. (2005). Imaging teleseismic P to S scattered waves using the Kirchhoff integral. *AGU Monographs*, pages 1–13.
- Liu, K. and Levander, A. (2013). Three-dimensional Kirchhoff-approximate generalized Radon transform imaging using teleseismic P-to-S scattered waves. *Geophysical Journal International*, 192:1196–1216.
- Miller, D., Oristaglio, M., and Beylkin, G. (1987). A new slant on seismic imaging: Migration and integral geometry. *Geophysics*, 52:943–964.
- Papanikolaou, D. J. and Royden, L. H. (2007). Disruption of the Hellenic arc: Late Miocene extensional detachment faults and steep Pliocene-Quaternary normal faults – or what happened at Corinth? *Tectonics*, 26:1–16.
- Park, J. and Levin, V. (2000). Receiver functions from multiple-taper spectral correlation estimates. *Bulletin of the Seismological Society of America*, 90:1507–1520.
- Pavlis, G. (2011). Three-dimensional, wavefield imaging of broadband seismic array data. *Computers & geosciences*, 37(8):1054–1066.
- Pe-Piper, G. and Piper, D. J. W. (2007). Neogene backarc volcanism of the Aegean: New insights into the relationship between magmatism and tectonics. *Geological Society of America*, 418:17–31.
- Pearce, F., Rondenay, S., Sachpazi, M., Charalampakis, M., and Royden, L. (2012). Seismic investigation of the transition from continental to oceanic subduction along the western Hellenic Subduction Zone. *Journal of Geophysical Research: Solid Earth*, 117(B7).
- Phinney, R. (1964). Structure of the Earth’s crust from spectral behavior of long-period body waves. *Journal of Geophysical Research*, 69(14):2997–3017.
- Rondenay, S. (2006). Multi-disciplinary experiments for dynamic understanding of subduction under the Aegean sea. *International Federation of Digital Seismograph Networks*.
- Rondenay, S. (2009). Upper mantle imaging with array recordings of converted and scattered teleseismic waves. *Surveys in Geophysics*, 30:377–405.
- Rondenay, S., Bostock, M., and Fischer, K. (2005). Multichannel inversion of scattered teleseismic body waves: practical considerations and applicability. *Geophysical monograph-american geophysical union*, 157:187.
- Rondenay, S., Bostock, M., and Shragge, J. (2001). Multiparameter two-dimensional inversion of scattered teleseismic body waves 3. Application to the Cascadia 1993 data set. *Journal of Geophysical Research: Solid Earth*, 106(B12):30795–30807.

- Rondenay, S., Montesi, L. G., and Abers, G. A. (2010). New geophysical insight into the origin of the Denali volcanic gap. *Geophysical Journal International*, 182(2):613–630.
- Rondenay, S., Spieker, K., Sawade, L., Halpaap, F., and Farestveit, M. (2017). GLImER: A new global database of teleseismic receiver functions for imaging Earth structure. *Seismological Research Letters*, 88:1–10.
- Ryberg, T. and Weber, M. (2000). Receiver function arrays: a reflection seismic approach. *Geophysical Journal International*, 141:1–11.
- Schimmel, M. and Paulssen, H. (1997). Noise reduction and detection of weak, coherent signals through phase-weighted stacks. *Geophysical Journal International*, 130:497–505.
- Shang, X., de Hoop, M. V., and van der Hilst, R. D. (2017). Common conversion point stacking of receiver functions versus passive-source reverse time migration and wavefield regularization. *Geophysical Journal International*, 209(2):923–934.
- Sheehan, A. F., Shearer, P. M., Gilbert, H. J., and Dueker, K. G. (2000). Seismic migration processing of P-SV converted phases for mantle discontinuity structure beneath the Snake River Plain, western United States. *Journal of Geophysical Research*, 105:19055–19065.
- Tauzin, B., Bodin, T., Debayle, E., Perrillat, J.-P., and Reynard, B. (2016). Multi-mode conversion imaging of the subducted Gorda and Juan de Fuca plates below the North American continent. *Earth and Planetary Science Letters*, 440:135–146.
- Tauzin, B., Reynard, B., Perrillat, J.-P., Debayle, E., and Bodin, T. (2017). Deep crustal fracture zones control fluid escape and the seismic cycle in the Cascadia subduction zone. *Earth and Planetary Science Letters*, 460:1–11.
- Tessmer, G. and Behle, A. (1988). Common reflection point data-stacking technique for converted waves. *Geophysical Prospecting*, 36:671–688.
- Tonegawa, T., Hirahara, K., Shibutani, T., Iwamori, H., Kanamori, H., and Shiomi, K. (2008). Water flow to the mantle transition zone inferred from a receiver function image of the Pacific slab. *Earth and Planetary Science Letters*, 274:346–354.
- Tromp, J., Komatitsch, D., and Liu, Q. (2008). Spectral-element and adjoint methods in seismology. *Communications in Computational Physics*, 3:1–32.
- Tzanis, A., Efstathiou, A., Chailas, S., and Stamatakis, M. (2018). Evidence of recent plutonic magmatism beneath Northeast Peloponnesus (Greece) and its relationship to regional tectonics. *Geophysical Journal International*, 212:1600–1626.
- Wang, Y. and Pavlis, G. L. (2016). Roughness of the mantle transition zone discontinuities revealed by high-resolution wavefield imaging. *Journal of Geophysical Research*, 121:6757–6778.

- Wilson, D. and Aster, R. (2005). Seismic imaging of the crust and upper mantle using regularized joint receiver functions, frequency-wave number filtering and multimode Kirchhoff migration. *Journal of Geophysical Research*, 110:1–12.
- Wu, R. and Aki, K. (1985). Scattering characteristics of elastic waves by an elastic heterogeneity. *Geophysics*, 50:582–595.
- Yamauchi, M., Hirahara, K., and Shibutani, T. (2003). High resolution receiver function imaging of the seismic velocity discontinuities in the crust and the uppermost mantle beneath southwest Japan. *Earth, Planets, Space*, 55:59–64.
- Ylmaz, O. (2001). *Seismic Data Analysis*.
- Zheng, Y., Lay, T., Flanagan, M. P., and Williams, Q. (2007). Pervasive seismic wave reflectivity and metasomatism of the Tonga mantle wedge. *Science*, 316:855–859.



# A new look at the Southern Alaska Subduction Zone using 2D and 3D Migration of Receiver Function

To be submitted to *Journal of Geophysical Research*

Florian Millet<sup>1,2</sup>, Stéphane Rondenay<sup>2</sup>, Thomas Bodin<sup>1</sup>, Carl Tape<sup>3</sup>

[1] Laboratoire de Géologie de Lyon, UMR 5276, Université de Lyon, Villeurbanne, France

[2] Department of Earth Science, University of Bergen, Bergen, Norway

[3] University of Alaska Fairbanks, Geophysical Institute, Fairbanks, Alaska

## Keypoints

- We apply two complementary teleseismic migration methods to a new composite seismic dataset combining the data from three temporary arrays deployed in Southern Alaska from 2000 to 2018.
- The Pacific plate is observed down to 170 km northwest of Cook inlet, with a departure at depth between the subducting interfaces and the seismicity envelope.
- The transition from the Pacific crust to the Yakutat terrane is marked by an abrupt change in crustal thickness at depths of 60 to 80 km and happens further to the north-east than previously thought.

## Abstract

Southern Alaska is located at the northern interface between the Pacific plate and the North American continent. The subduction of the Pacific plate generates arc volcanoes along the whole Aleutian trench, but volcanic activity suddenly stops at the Denali Volcanic Gap, which links the subduction in the west to the collision and accretionary system to the east. The volcanic gap has been linked to the underthrusting of the Yakutat terrane. However, the transition from the Pacific slab to the Yakutat at depth is not fully understood. To investigate this issue, we use a new composite seismic dataset, combining the data from three temporary arrays deployed in the region from 2000 to 2018 (network codes XE, YV and ZE). We apply two complementary teleseismic migration methods, 2D GRT and 3D Kirchhoff migration, to obtain 3D scattering images of the region. Our results show that the transition from the Pacific crust to the Yakutat terrane, which is marked by an abrupt change in crustal thickness at depths of 60 to 80 km in both methods, happens further north than previously thought. The subducted Pacific plate is observed down to 170 km to the northwest of Cook inlet. The Kirchhoff migration also images a departure at depth between the imaged subducting interfaces and the seismicity envelope in this region, which is linked to the progressive eclogitization of the crust. There is no clear evidence for this phenomenon under the Denali Volcanic Gap where the Yakutat terrane subducts under Alaska.

## 1 Introduction

Southern Alaska, located at the interface between the Pacific plate and the North American continent, is comprised of several superimposed geological units. Currently, the Yakutat terrane is subducting under the North American plate (Brocher et al., 1994). The Yakutat terrane has been seismically imaged using local earthquake tomography, teleseismic body wave and surface wave analysis as well as active source experiments, and is characterized at depth by a crustal low velocity anomaly that is 10 to 15 km thicker than the regular Pacific crust (Chuang et al., 2017). The lateral extent of the Yakutat terrane is underlined by the abrupt end of volcanic activity along its western limit and a lack of seismicity to the east of its eastern limit.

It remains unclear how the Yakutat transitions to the Pacific crust at depth (Martin-Short et al., 2018). Based on geometric clues, this transition could be accompanied by a gradual bend, or even a tear in the subducting slab at the transition. However, so far there has been no seismological evidence of a tear in the slab (Eberhart-Phillips et al.,

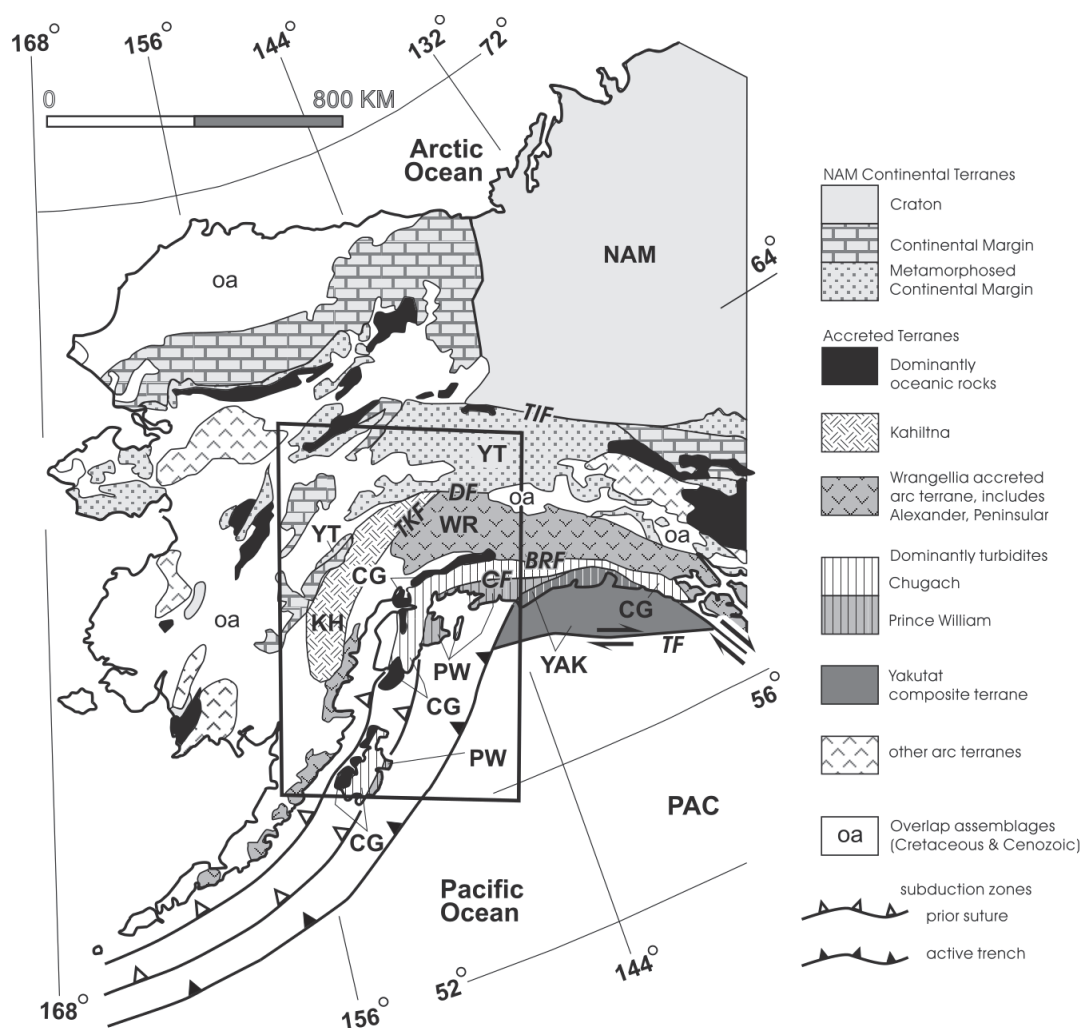


**Figure 1** – Tectonic setting of Alaska, reproduced from Eberhart-Phillips et al. (2006) based on terrane map by Nokleberg et al. (2000). Faults are TIF, Tintina; DF, Denali; TKF, Talkeetna; BRF, Border Ranges; CF, Contact; TF, Transition. Terranes are YT, Yukon-Tanana; KH, Kahiltna; WR, Wrangellia composite; CG, Chugach; PW, Prince William; YAK, Yakutat.

2006). Understanding how the Pacific crust transitions to the Yakutat terrane is crucial to understand the dynamics of the Southern Alaska subduction zone, but also the seismic hazard and volcanic activity in the area.

## 1.1 Geological setting

The northward subducting Pacific plate converges towards the continent at an estimated rate of 4.6 to 5 cm/y, and accreted several oceanic terranes over the past 160 to 220 My (Wang and Tape, 2014). The first accreted units are delimited by the Denali fault, and from north to south are the Kahiltna flysch, the Talkeetna terrane and associated ultramafic rocks, the composite Wrangellia terrane, the turbiditic Chugach and Prince William



terranes and finally the Yakutat terrane from 24 My onwards (see figure 1, reproduced from [Eberhart-Phillips et al., 2006](#)). The Denali fault also delineates the central part of the Alaska mountain range and a large Moho step, highlighting the thickening due to the accretion of these terranes ([Martin-Short et al., 2018](#)). To the south-west of the Alaska range, the subduction of the Pacific plate generates arc volcanoes that extend from the Aleutian subduction to central southern Alaska until 152°W, where the volcanic activity stops, forming the Denali Volcanic Gap. Further east, the Wrangell volcanic field is the last large volcanic area before the Cascadia region ([Rondenay et al., 2010](#)).

The largest recorded earthquake in the region happened on the 27th of October 1964 north and west of the Prince William sound and was of magnitude 9.2 ([Ichinose et al., 2007](#)). Since this earthquake, the faulting along this shallow part of subduction system has mostly been of normal type, with tension axis parallel to the dip direction, likely indicating an intraplate origin ([Li et al., 2013](#)). Recently, slow-slip events (SSE) and low frequency earthquakes (LFE) have been detected in the region as well, with the potential to release as much energy as magnitude  $\sim 8$  earthquakes over periods of 2 to 10 years ([Li et al., 2016](#); [Chuang et al., 2017](#)). However, the plate interface faulting in this region is still very active, as demonstrated by the 30th November 2018 Mw 7.1 event under Anchorage ([Liu et al., 2019](#)).

The subduction in the south of the region is complex. The region around the volcanic gap links the subduction of a ‘standard’ oceanic slab in the Aleutians to the west, to a collision and accretionary system involving the Yakutat terrane to the east. The collision of the Yakutat terrane is accommodated by the right-lateral Transition Fault ([Eberhart-Phillips et al., 2006](#)). The transition region between these two settings hosts one of the most shallowly dipping subduction in the world, at an estimated 3° dip under the Kenai peninsula ([Li et al., 2016](#)).

The volcanic gap has been linked to the subduction and underthrusting of the Yakutat terrane. Early studies suggest that the limit of the underthrusted Yakutat terrane is linked to a magnetic signal, the Magnetic Slope Anomaly, that has been inferred to be of lower crustal nature ([Brocher et al., 1994](#)). This section of the Yakutat terrane is highly magnetic, hence it might be enriched in iron and magnesium, leading to the idea that the Yakutat terrane is a former oceanic plateau, which is coherent with collages in the region. Offshore seismics confirm the different nature of either sides of the Slope Magnetic Anomaly, showing a 10 km thick high velocity layer on the eastern side of the anomaly that continues under the Prince William terrane, north of the surface expression of the Yakutat terrane ([Brocher et al., 1994](#)).

The eastern boundary of the Yakutat terrane is highlighted by the seismicity variations

across Southern Alaska, as deep seismicity completely stops east of 148°W (figure 2). The seismicity in this region between 60°N and 62°N is almost flat, further highlighting the low dip angle of subduction in this transition area. The deepest earthquakes to the east of the Kenai peninsula reach 200 km depth, but it remains unclear how the Yakutat transitions to the Pacific crust, as there is no major gap or step in seismicity between the two regions (figure 2).

## 1.2 Seismic imaging in the region

The global structure of this region has been studied with passive and scattered waves seismology. Receiver function (RF) analysis showed that the Yakutat crust is 11~20 km thick with velocities up to 20

Eberhart-Phillips et al. (2006) also observed a low  $V_p$  and high  $V_p/V_s$  ratio in the west, where it underlines volcanic activity, as well as in the subducted Yakutat terrane. The part of the mantle wedge above the subducted Yakutat crust is cold and may contain pieces of a Cretaceous aged slab. This has implications for volcanism, as fluids cannot travel through that type of mantle wedge material, and hence the fluid necessary for volcanic activity would only be able to escape the subducting plate at the edges and corners of the Yakutat terrane. These results are confirmed by thermal analysis of the state of the mantle wedge in the region (Rondenay et al., 2010). Due to the shallow dip, the whole subduction system cools before the slab is deep enough to release fluids, which inhibits the production of magmas, hence less volcanic activity above the subducted Yakutat slab.

However, the transition from the Pacific slab to the Yakutat at depth is not fully understood. 3D  $V_p$  inversion does not show any sign of tear in the slab with grid spacing down to 25 km. One would need results with a higher resolution, ideally of less than 10 km in depth and laterally, to confirm this observation. In order to obtain such resolution, a 3D model of the scattering structure in the region is needed, which current RF studies have failed to provide. Such a 3D model would allow us to see potential tears directly, or at least test their presence with synthetic waveforms. This requires a dense 2D coverage and a 3D scattered wave imaging method.

Here we use a new composite dataset to obtain 3D images of the region and compare the scattering structure of both ends of the subduction system. This dataset is created by combining the data from three temporary arrays deployed from 2000 to 2018, with about 2 years of data for each array. The arrays themselves are mostly arranged in straight lines and perpendicular crosses. They are described in greater detail in section 2. To

our knowledge, this is the most complete passive dataset spanning the entire southern Alaska study area. To obtain these images, two complementary migration methods are used. The first one is a 2D GRT that has been developed by [Bostock et al. \(2001\)](#). In this method, the data are projected on a 2D line, hence the inversion is more robust as it averages all data across the profile. The second one is a 3D Kirchhoff migration developed by [Millet et al. \(2019\)](#). In this method, the original station distribution is not altered, hence comparing the two results will allow to investigate and validate the 2D nature of the structures. They are described in greater detail in section 3.

The results for both migration methods are shown in section 4. Our images are coherent with previous observations in the region. They highlight different geometries and subduction dynamics to the west (Pacific crust) and the east (Yakutat terrane) of the Denali volcanic gap, with the former continuously steepening landwards and the latter seemingly separated in two distinct dipping structures. The results agree with local seismicity distribution and slab contour estimates. The results are discussed in section 5 before presenting some concluding remarks in section 6.

## 2 Data and processing

The objective of this study is to image sharp variations in seismic properties. For this, high frequency scattered wave data with good data coverage are needed. To that end, data from dense temporary deployments are used, as opposed to data from larger permanent deployments that have lower coverage density. Furthermore, to obtain the best image and extract as much information from the data, the scattering information from the free surface multiples is extracted along with the information from the forward scattering. These multiple scattered phases reflect off the Earth's surface as either P or S waves (lowercase p and s hereafter) and are scattered back up as either P or S waves (uppercase P and S hereafter). Those phases referred to as PpP, PpS, PsP and PsS respectively. The PsS mode can be further decomposed into PsSv and PsSh scattering as the S-to-S scattering can generate both Sv and Sh phases in the case of dipping discontinuities or anisotropy. We refer the reader to section 3 for more details on how these data are used.

The arrays are shown in figure 2 along with the imaging lines for both imaging methods. Note that the GRT and Kirchhoff have different imaging lines. GRT projects the data on an average migration line along the symmetry plane of the structures (i.e., along the dip direction here). Projection lines for the GRT are red and labelled 1-2 and 3-4. Kirchhoff does not alter the station distribution, therefore the imaging lines will be located under denser station lines in the deployments. Imaging lines for the Kirchhoff are

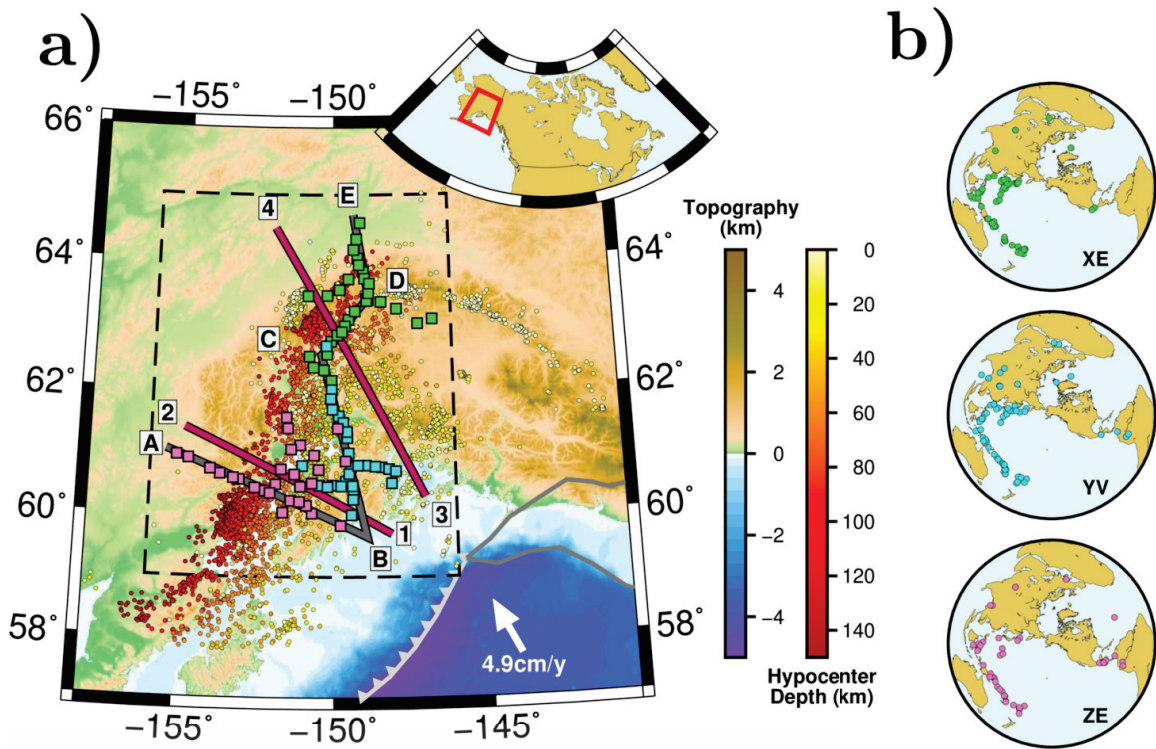


**Figure 2** – (a) Map of Southern Alaska. Plate interface after Kim et al. (2014). Stations colored by array: BEAAR is green, MOOS blue and SALMON pink. Events obtained from the AEIC catalog and colored by hypocenter depths. Lines 1-2 and 3-4 represent the 2D GRT migration lines. Lines A-B, B-C, C-D and D-E are the slices through the 3D Kirchhoff migration model. (b) Distribution of earthquakes selected for the final migrations on the three arrays.

in grey and labelled A-B, B-C, C-D and D-E.

The influence of the projection operation, which is done in the GRT but not the Kirchhoff, is most visible when the data are not regularly spaced and distributed. On one hand, projecting the data on a migration line artificially increases station density, thus increasing the coverage of scattered phases at a given point by collapsing all the incoming and outgoing rays in the same plane. On the other hand, projecting creates artifacts in the migrated images as 3D scattering cannot be taken into account. In dense temporary deployments, which are limited in station distribution by variability in accessibility to the station sites, data are rarely regularly distributed. This observation confirms that data from such dense temporary deployments will help us showcase the complementarity of both methods best. The GRT has its resolution enhanced and its 3D imaging capability reduced by the projection operation. Kirchhoff has lower data coverage and density but should produce less 3D artifacts. Adding permanent and semi-permanent stations (e.g.

stations from the TA, AK and AV networks) will be done later, and will highlight the potential of Kirchhoff even more.

## 2.1 Composite array for 2D and 3D imaging

Seismograms were collected exclusively on three temporary deployments across Southern Alaska (figure 2). The northernmost array is the Broadband Experiment Across the Alaska Range (BEAAR, network code XE, green squares in figure 2, Christensen et al. (1999)), comprising 36 stations and operating between 1999 (7 stations) and 2001 (17 stations) as part of an IRIS/PASSCAL experiment. It is cross shaped, with 28 stations following the mainly NS trend of Highway 3 and 8 stations aligned perpendicularly in a curly EW line (Ferris et al., 2003). Station spacing on the main line is just above 10 km.

The second array, just South of BEAAR, is the Multidisciplinary Observatory Of Subduction (MOOS, network code YV, blue squares in figure 2, Abers and Christensen (2006)), comprised of up to 34 stations recording between May 2006 and June 2008. It consists of a main NS line connecting the Kenai peninsula to the southern tip of BEAAR through Anchorage and a smaller dense EW cross on the Kenai Peninsula itself (Li et al., 2013). Overall inter-station spacing is about 15 km.

Finally, the most recent deployment is the Southern Alaska Lithosphere and Mantle Observation Network (SALMON, network code ZE, pink squares in figure 2, Tape et al. (2015)), comprised of 28 stations operating during the time period 2015 to 2018. This array has one mostly NW-SE 14 stations line, designed in an effort to follow closely the dip of the subduction, and beneath which the subducting slab has not yet been imaged, as well as a fully 2D deployment region around the Cook Inlet (Tape et al., 2017). Station spacing is quite variable with larger groups of stations about 15 km away from each other with gaps of up to 40 km between them.

Some stations are co-located from deployment to deployment. The networks are partly imbricated, which makes joint migration easier. This provides an almost continuous coverage from Whitefish Lake (point A on figure 2) west of the Cook Inlet to Nenana (point E on figure 2) in the Northern part of the region through point B just offshore the Kenai Peninsula, as shown by the grey lines, that represent the 2D imaging slices through the 3D Kirchhoff migration. This brand new composite array crosses the alleged western limit of the Yakutat in the southern part of MOOS, which means that our two main orientations are along-dip the Yakutat on one side (BEAAR and upper part of MOOS) and the Pacific plate (SALMON and lower part of MOOS).

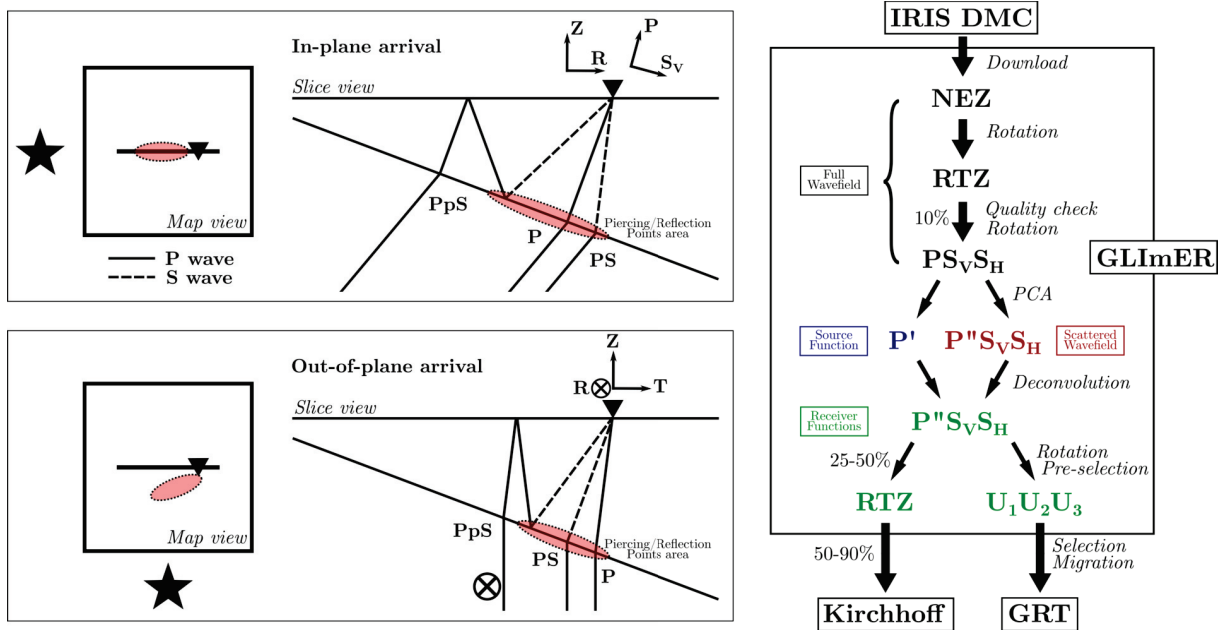


**Figure 3** – 3D scattering geometry and data-processing steps. (a) Representation of the forward and back-scattered waves (example of the PpS) with the 3D scattering geometries based on back-azimuth for a dipping interface. Red area corresponds to sensitivity region. (b) Processing steps in GLImER from download to migration of the scattered wavefield data. Percentages represent part of data selected at each step.

## 2.2 Pre-processing of the data

The data are processed with the GLImER package (Rondenay et al., 2016). This package was developed in an effort to create a global database of RF and automate most of the pre-processing workflow to obtain them. The first step is to set the region of interest (list of receivers, see previous section) as well as the time frame (list of sources) for our study. Here, pre-selection criteria are such that  $M_w > 5.5$  and the epicentral distance is between  $30^\circ$  and  $90^\circ$ . This yielded 822 events for XE, 759 events for YV and 451 events for ZE. There are slightly less events for ZE, which can be a problem in terms of relative amplitude when jointly migrating data for all arrays. Events that were finally selected (section 2.4) for the migration are visible on figure 2 for all 3 arrays.

The data for those 2032 events are automatically downloaded from the IRIS DMC in SAC format. All arrays are open access as of August 2019. These data need to be transformed from raw recordings to usable RF, which yield estimates of the intensity of the P-to-S, P-to-P and S-to-S scattering due to geologic structures under an array of receiver. The GLImER package is used to achieve that. The main steps of this process are described throughout the rest of this section and illustrate it in figure 3.

The data are then automatically rotated in the RTZ reference frame for each event

and the onset of the primary P-wave adjusted to zero lag. Here, there are two different automated pre-selection quality checks. The first is signal-to-noise ratios (SNR) on the R and Z components. This ensures that signal is present on every individual trace and that it is coherent on the components that record the larger amplitudes (R for P-to-S scattering and Z for the primary P). Parameters are as follows: the first time window is from -20 to -5 seconds around theoretical arrival, the second window is from -5 to +10 seconds and SNR criteria  $>5$  for R and  $>10$  for Z. These quite large windows allow to never miss events even if the waveforms are not at exactly zero lag.

The second quality check is amplitude decay on the P component. This ensures that the signals do not have a too long source time function (STF), which can cause problems in the deconvolution. Here, the same signal window as previously are used again, as well as a third window from +15 to +30 seconds after theoretical arrival, where most of the scattering is expected. The mean signal on the third window is divided by that on the second one, and the decay criterium is  $<1.2$ . Usually this is set to 1, which corresponds to as much energy for the scattered phases as for the main arrival. Here, this value is slightly increased, as the first time window from -5 to +10 seconds around primary signal has an artificially lower mean energy content because of the 5 second pre-event low amplitude segment.

Finally, the data is checked for completeness. Typically, only events recorded on at least half of the active stations at every time are retained. This is not absolutely necessary but allows to speed up the migration by avoiding computations for events that do not bring much information (see section 3). This results in the pre-selection of 72 events for XE, 73 events for YV and 50 events for ZE. At this stage there is also a first manual check of timings, amplitudes and processing errors to remove unwanted signals.

## 2.3 Deconvolution and receiver functions

Receiver functions aim at providing accurate estimate of the scattering intensity for the direct P-to-S scattering mode, hereafter referred to as PS, as well as for the free-surface multiple P and S modes. The multiples are described in section 2.1, and arrive at increasingly large times at the stations with more S wave legs (see figure 3). The PsP phase will be ignored in the migration process as it typically has very low energy because of the double conversion and arrives at similar times to the PpS multiple (Rondenay, 2009). Apart from their timing differences, the different scattered phases are also recorded differently on the three components of the seismograms. In particular, the S phases (PS, PpS and PsS) are mostly recorded on the horizontal components whereas the P phases (direct

wave and PpP multiple) are mostly recorded on the vertical component (figure 3). For this reason, the rest of the analysis is performed using multi-component data and seek to obtain accurate RF for all three components.

Once this is established, the data go through the multi-channel processing workflow. The data are rotated in the P-SV-SH reference frame and finely realigned on the primary P-wave onset on a per-event basis using a cross-correlation scheme on the P component. Note that because the direct P wave is primarily confined to the P component, the SV and SH component already represent mostly P-to-S scattered energy (figure 3). A principal component analysis (PCA) is performed for each event on the P component that separates the incoming coherent signal (first component, hereafter called P') on all records from the variable (higher components, hereafter called P'') part of the signal, which is interpreted as the STF for the event and first order P scattering, respectively. Mathematically,  $P'' = P - P'$  and P''-SV-SH represents the entire three component first order scattered wavefield (see figure 3).

Our estimates of the STF are as impulsive as possible. Longer STF also include the late reflections from flat interfaces, which therefore disappear from the RF and cannot be imaged anymore. This means just a couple of oscillations when the signal obtained from the PCA is very clear, and if this is not the case, the STF is cut when energy drops, with a maximum of 50 seconds. This way of performing the deconvolution allows us to get an accurate RF for the vertical component that contains most of the PpP energy. Indeed, the PCA is performed on the waveforms once they are aligned on the primary P-wave, putting it to infinite slowness. PpP has a finite slowness that differs from that of the direct P wave. Graphically, this means that it is not horizontal, and therefore not on the first component of the PCA.

The RF are obtained through time-domain iterative deconvolution with a Gaussian parameter width of 10 and filtered in the frequency band  $0.03 \sim 0.5$  Hz (Ligorria and Ammon, 1999). These correspond to wavelengths of 14 km at velocities of 7 km/s for P and 8 km at 4 km/s for the S-waves. As multiples have a vertical resolution of half a wavelength, this means 7 km for PpP and 4 km for PpS and PsS waves. These frequencies will be re-adjusted later in the migration algorithms to improve coherence in the multi-mode migration, as higher frequencies show better defined structures but lower frequencies allow for better stacking.



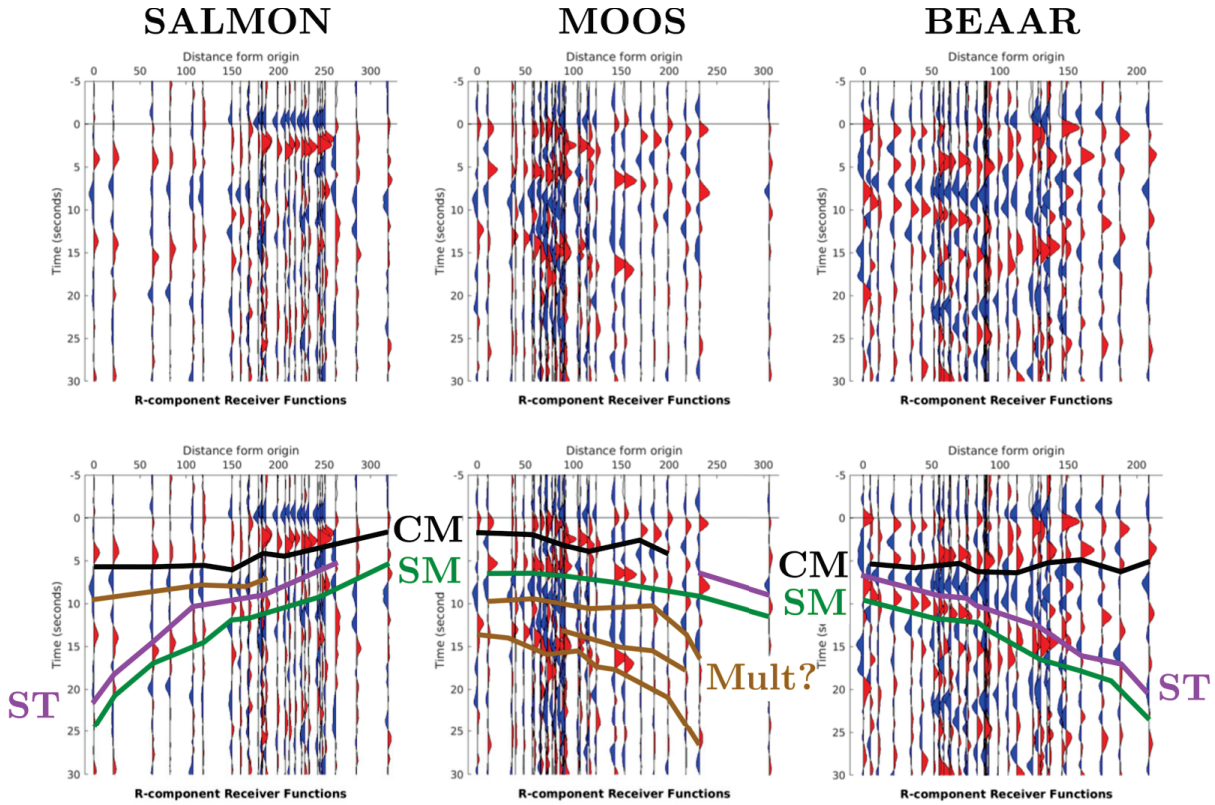


**Figure 4** – Raw and interpreted NMO stacked data for sections along the three arrays. Distance is taken along lines that are parallel to the GRT imaging lines (fig1) from the first station of the array, starting in the NW for SALMON (a) and in the South for MOOS (b) and BEAAR (c). Color lines represent our interpretations for the various interfaces, and are plotted just under the peaks that they are associated with for easier visualisation. Black lines show our interpretation for the Continental Moho (CM, positive), purple for the Slab Top (SL, negative), green for the Slab Moho (SM, positive) and brown for free surface multiples.

## 2.4 Visual inspection of the data

Selection of traces is event-based on individual GRT and Kirchhoff migrations. Special attention during this selection process is devoted to overall ringing of RFs, which is an artefact occurring at the deconvolution stage. Moreover, the modes are individually selected on every event. For a given event, we look at the features that are coherent across scattering modes, and select only the modes that show those coherent features. This is the most time-consuming and critical step during the selection process, and allows for better stacking of the different modes. It is especially critical in geometries where no high scattering energy from specific scattering modes is expecting given the orientation of the incoming wavefront.

This final step results in the selection of 28 events for XE, 27 events for YV and 28 events for ZE, representing 2% to 5% of the events that are downloaded on each array. In

regards to the potential issue of joint migration with different number of events for each array discussed in section 2.3, the number of events finally selected for the three arrays are almost identical, so no major discrepancy between the arrays is expected in the joint migration. The stacked RF for these selected events are presented in figure 4 along with preliminary interpretations of reflectors.

### 3 Methods

Two different migration techniques are used to interpret the data. Migration takes the data recorded at stations and uses it to find the scattering points and reflectors in the subsurface by correlating energy peaks that correspond to the same structure on different waveforms. In the data space, this corresponds to determining the shape of the hyperbolae that link those peaks between stations. In the model space, this corresponds to stacking the data along migration isochrons corresponding to the different timings of these energy peaks. The data are migrated to depth using a reference velocity model that represents a long-wavelength average of the seismic structure of the region. This can take the form of a 1D (which is used here), 2D or 3D velocity model.

#### 3.1 2D GRT migration

The first method is a generalized radon transform (GRT) based migration (Bostock et al., 2001). It converts the scattered wavefields from multiple events, that are obtained from the P-wave coda, into velocity variations in the subsurface. The migration is posed as an inverse problem where the solution corresponds to a map of elastic perturbations that fit the amplitude and phase of the observed individual RFs. This method is theoretically capable of retrieving volumetric heterogeneities. However, it requires a dense ray coverage through each point in the model space to work correctly. Restricting the three dimensional coverage to a two dimensional imaging plane instead of an imaging volume accelerates the forward calculations and stabilizes the inversion considerably. Therefore, our implementation is limited to 2D modeling and imaging. During the migration, a  $\sqrt{i\omega}$  filter is applied to the data to account for 2D wave propagation. Due to this filter and the inversion for elastic parameters, the discontinuities are interpreted at the base of the velocity anomalies. In depth explanation can be found in e.g. Bostock et al. (2001).

Advantages of the 2D GRT migration are as follows. First, GRT is computationally efficient. It takes a 1D input model and back-projection of the data in 2D is quick. Second, projecting the data on a single 2D plane artificially increases the station density.

By reducing the array geometry to an average line, the distance between stations is reduced and the resolution of the final images enhanced, of course, given that the actual structures are 2D. Third, GRT gives us velocity variations compared to the reference velocity model along the scattering interfaces. These values can be interpreted in terms of absolute velocities within the various geological boundaries, and in turn be directly interpreted in terms of lithologies, pressure, temperature and hydration conditions.

Drawbacks of the 2D GRT are as follows. First, projection of the data on a 2D line can produce significant artifacts in the case of 3D geological structures. In this case, one needs to remove selected stations to improve the efficiency of the stacking and reduce the artifacts that the projection creates. Second, our implementation of the GRT is so far limited to the use of a 1D reference model. Third, it requires comprehensive scattering coverage to recover accurate elastic perturbations. This means that, even if the scattering structure can be recover with limited data, the exact values for the velocity perturbation estimates obtained with the GRT are only accurate if enough data from all back-azimuths and incidence angles are used in the inversion (see, e.g., [Rondenay et al., 2005](#)). This can be difficult to achieve even in a 2D migration with only temporary data.

### 3.2 3D Kirchhoff migration

The second method is a fully 3D Kirchhoff migration. The method borrows from developments in active seismics, where dense datasets of active shots acquisitions across relatively small study areas allow for full 3D ray coverage of all points in the subsurface ([Hagedoorn, 1954](#)). It propagates the recorded scattering information, the RF, back into the Earth from the receivers to the sources at all potential scattering points and discriminates the actual scattering points from the non-scattering points through constructive stacking. The data interfere along their migration isochrons and the imaging condition allows us to obtain the amplitude of the scattering potential at depth, which is linked to the impedance contrasts at the scattering interfaces and heterogeneities.

[Millet et al. \(2019\)](#) adapted the fully 3D Kirchhoff imaging principle for teleseismic passive seismology. This method combines the efficiency of a 3D eikonal solver, the fast marching method (FM3D, [de Kool et al. \(2006\)](#)), with an implementation of first order scattering phase and amplitude calculations based on Ray-Born scattering. The data used in the 3D Kirchhoff migration are the same RFs as in the GRT. The migration is performed in a spherical 3D model with 1D or 3D background velocity model. The migrated data are then visualized by slicing through the 3D migration model on given 2D lines. During the migration, a  $i\omega$  filter is applied to the data to account for 3D wave propagation, hence

the discontinuities are interpreted in the middle of the scattering intensity anomalies.

This method is computationally efficient compared to fully elastic 3D migration methods. It computes the delay times for all scattered phases with a single FM3D run and uses these timefields to characterize both scattering timing and amplitude at each point in the model. It treats each grid point in the migration model as a potential scattering point. Taking the gradient of the timefields and comparing the resulting orientation vectors for the incoming outgoing waves allows to compute the scattering angle at every grid point. Using scattering patterns based on the Ray-Born approximation, which can be found in e.g. [Wu and Aki \(1985\)](#) or [Beylkin and Burridge \(1990\)](#), the 3D Kirchhoff migration can predict the amplitude and polarity of the expected scattering. This resembles closely what is done in the GRT inversion, and is very important for dipping discontinuities where polarity reversals can be problematic ([Cheng et al., 2016](#)). This allows to treat data from all incoming back-azimuths and slownesses correctly in an automated manner.

Advantages of the 3D Kirchhoff are as follows. First it can take a 3D velocity model as input at no additional computational cost. In this study however, a 1D model is used to better showcase the complementarity with the GRT migration, which cannot yet handle a 3D reference velocity model. We plan on using a 3D model for further investigations. Second, because it does not alter the original station geometry, it can image structures in every orientation, which is not the case with most 2D methods, including the GRT. This ensures that the data are migrated at the location where they originate from, and that there is no distortion in the 3D migrated model. Third, even though the images are only interpretable in terms of scattering potential, taking the scattering patterns into account during the migration gives a good first order idea of the relative velocity contrasts between different interfaces in the same migration image. Finally, even though this study is limited to P-RF, it can easily be implemented for S-RF ([Farra and Vinnik, 2000](#)).

Drawbacks of 3D Kirchhoff are as follows. First, it is still longer to run than 2D methods such as the GRT if the same grid density is to be achieved during the migration. Second, the fact that the data are not projected on the migration line beforehand means that holes in station coverage show up as holes in the images. Third, [Millet et al. \(2019\)](#) showed that a mix of linear and dense 2D station distribution is not ideal for imaging as the difference in stacking power can create variations in the intensity of reflectors in the final migrated images. To avoid this, one can remove stations that are away from the planned imaging lines, but this also removes some of the 3D imaging capabilities of the method.

### 3.3 Multi-mode stacking

Both methods offer the possibility to interpret the data for the first order forward and backscattering modes. This includes the PS as well as the free surface multiples PpP, PpS, PsSv and PsSh (see section 2.1). In the GRT migration, the algorithm inverts all the modes jointly to obtain combined estimates of the variations in  $V_p$ , estimated from the PpP multiple, and  $V_s$ , estimated from the S modes (Bostock and Rondenay, 1999). In the 3D Kirchhoff migration, all the modes are migrated together to retrieve the coherent scattering structure from both  $V_p$  and  $V_s$  variations (Millet et al., 2019). It is important to note that all scattering modes are present in all individual images. For example, the multiple modes are migrated under their origin points in the PS migration, i.e. they are undermigrated. Conversely, the PS mode is migrated higher than where it originates in the multiples migrations, i.e. it is overmigrated. Only the coherence between the different modes discriminates between overmigrated, undermigrated and correctly migrated signals.

One of the properties of the free surface reflections is that they have a higher vertical resolution (Rondenay et al., 2005). This can be accounted for in the GRT migration by retrieving the  $V_s$  perturbation independently from the forward scattered and backscattered S modes independently, even if the same waveforms are used for all the modes. Our implementation of the Kirchhoff migration allows to filter the waveforms independently on every mode to match their respective vertical resolutions and enhance the coherence of the stacked migrated image.

### 3.4 Additional data and velocity models

Seismicity from the AEIC is plotted on top of the Kirchhoff image. These were obtained using permanent and temporary deployments across the whole state of Alaska. Only events that have reported location uncertainties of under 2 km are selected. They clearly outline the geometry of the subduction front (see figure 2).

Our observation are compared to previous results for the slab contour. The Slab2 model, which shows the top of the subducting slab in different regions, including Alaska, is plotted on top of the Kirchhoff images (Hayes et al., 2018). It has been obtained through compilation of several independent datasets, such as earthquake catalogs, active seismic studies, bathymetry information and more. Slab2 for the Aleutian-Alaska region is plotted along the Kirchhoff images in section 4.2.

The velocity models used for the seismicity location and in the migration schemes are described in table 1. The same 1D model is used for the GRT and the Kirchhoff migrations. It corresponds to the same model as Kim et al. (2014). It is a reasonable

**Table 1** – 1D models used in this study and in the earthquake location by AEIC. The " $\infty$ " corresponds to the half-space at the bottom of the model.

Model	Layer	Depth	$V_P(km \cdot s^{-1})$	$V_S(km \cdot s^{-1})$	$\rho(g \cdot cm^{-3})$
GRT and Kirchhoff	1	0 – 36.2	6.2	3.7	2.9
	2	36.2 – 200	7.81	4.36	3.4
AIEC	1	0 – 4	5.3	3.01	2.52
	2	4 – 9	5.6	3.18	2.61
	3	9 – 14	6.2	3.52	2.78
	4	14 – 19	6.9	3.92	2.97
	5	19 – 24	7.4	4.20	3.12
	6	24 – 33	7.7	4.37	3.20
	7	33 – 49	7.9	4.49	3.26
	8	49 – 66	8.1	4.60	3.32
	9	66 – $\infty$	8.3	4.72	3.37

average for the region, even if large variations from the Yakutat subduction in the East to the Aleutian subduction in the west can be expected. For comparison, the velocity model for the location of the earthquakes within the AEIC catalog is also specified in table 1. In future studies, we plan on including a 3D velocity model in both migrations, especially as it does not bear any additional computational cost for the 3D Kirchhoff.

## 4 Results

### 4.1 GRT images

First, the multimode images for the two GRT migration are presented in figure 5. As shown in figure 2, the data are migrated on two separate lines for those migrations. Both images are presented without interpretation in the top row and interpreted in the bottom row. The first image, from points 1 to 2, is computed using the data from the SALMON array and the southern half of the MOOS array together (figure 5a). The second image, from points 3 to 4, is computed using the data from the NS trending station line of the MOOS array along with all the data from the BEAAR array (figure 5b). The data are filtered up to 0.3 Hz for all modes – individual modes are available in the supplements.

Figure 5a shows a roughly NW-SE transect across the eastern end of the aleutian subduction system. A 15 km thick subducting low velocity anomaly dipping towards the

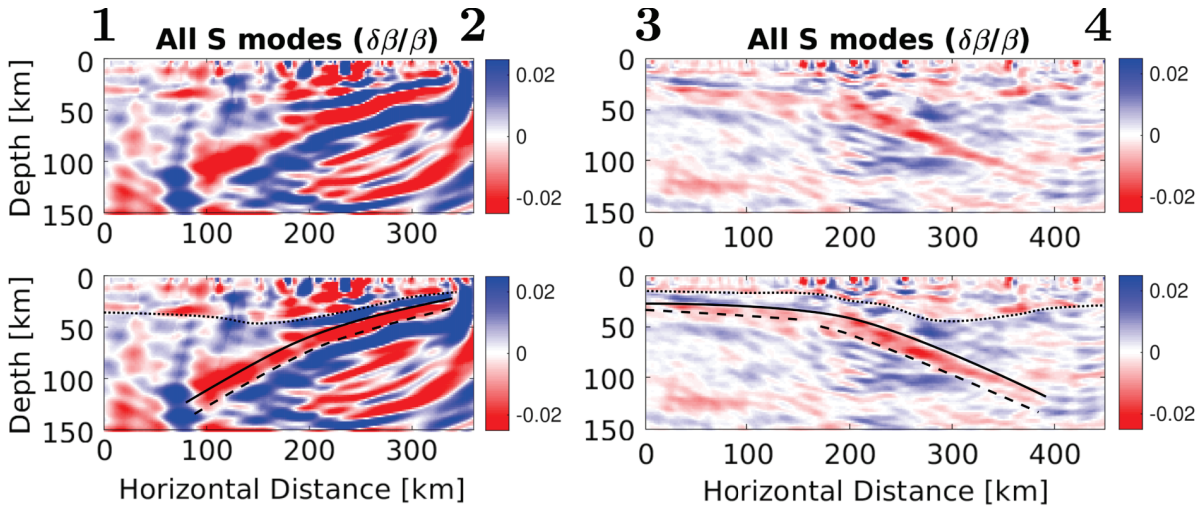


**Figure 5** – GRT images along lines 1-2 and 3-4. (a,b) Final multi-mode profiles. (c,d) Interpretation. Dotted lines represent the continental Moho, solid lines represent the slab top and dashed lines represent the oceanic Moho. Individual modes are available in the supplements.

NE is observed, which is interpreted as part of the Pacific crust. Analysis of the individual modes show that the thickness of this anomaly is constant at least down to 100 km depth (see supplement). There is a gradual increase in dip from  $15^\circ$  towards the eastern end of the Kenai peninsula to  $30^\circ$  under the Alaska mountain range. The continental Moho is clearly visible throughout this transect as well. Crustal thickness is  $\sim 20$  km at its thinnest near end of the Kenai peninsula, then dips to  $\sim 40$  km in the Cook inlet and is  $\sim 35$  km towards the NW end of the line. There is less energy on the left hand side of the image, where most of the data comes from SALMON. Analysis of the individual modes show that this is mostly due to the PsSv mode (see supplement).

Figure 5b shows a roughly NS transect, similar to Kim et al. (2014). Two clear portions of dipping low velocity layer are interpreted as the upper part of the subducting composite Pacific/Yakutat crust. The first one is a 5-10 km thick anomaly in the more or less flat part, where dip is less than  $8^\circ$ . The second one is a 15-25 km thick anomaly in the steeply dipping part, where dip is about  $29^\circ$ . There is a hole in between the two parts at about 190 km of horizontal distance that separates the two domains. A positive discontinuity, which is interpreted as the continental Moho, can be observed all along the profile. The continental crust in the southern part of the transect is 20 km thick. There is a transitional domain between 200 and 300 km of horizontal distance where the thickness of the crust reaches up to 45 km. In the northern part of the transect, the crustal thickness is 35 km.

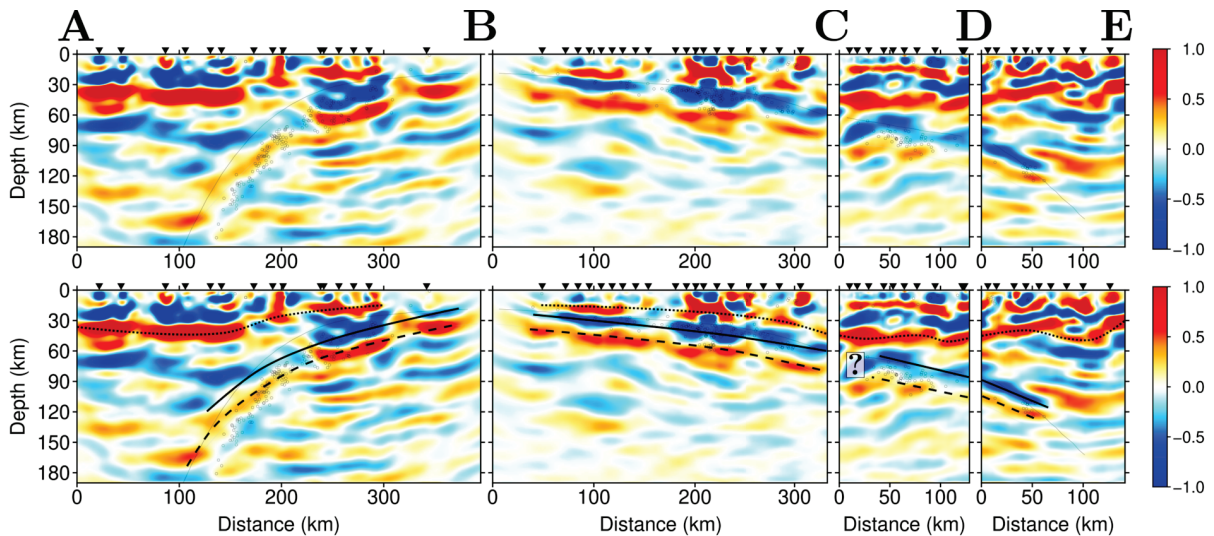


**Figure 6** – Kirchhoff images along lines A-B, B-C, C-D and D-E. (a) Final linear multi-mode profiles. Thin black line represents the slab contour based on slab2. (b) Interpretations. Thick dotted lines represent the continental Moho, thick solid lines represent the slab top and thick dashed lines represent the oceanic Moho. Individual modes are available in the supplements.

## 4.2 Kirchhoff images

The results for the 3D Kirchhoff multimode migration are shown in figure 6. Uninterpreted images are presented in the top row with seismicity and the Slab2 slab top interface model, and interpreted images are shown in the bottom row. For this migration, the placement of the stations is not altered, so the coverage is not perfect along the profile lines. This effect is clearly seen in line A-B (SALMON data), where the continental Moho as well as in the dipping slab are not entirely continuous under the sparser portions of the seismic array. The four slices through the 3D migrated model share common end points, which makes it easier to follow the interfaces from section to section. For the 3D Kirchhoff migration, the data for the PS mode are filtered up to 0.3 Hz, the PpP and PpS modes up to 0.25 Hz and the PsS mode up to 0.2 Hz. Individual mode images are presented in the supplements.

We shall now describe the migrated images individually. Line A-B is traced along the linear part of the SALMON array. It has the same strike as line 1-2 from the GRT. The dipping slab is slowly arching as it steepens from the coast to the NW. The low velocity anomaly, which is interpreted as the subducting crust, has a thickness of  $\sim 15$  km. Its signature can be followed down to almost 170 km depth. The continental Moho is visible as well, but it is only clearly defined below the continental part of the line, where it sits at about 40 km depth. Under the Cook inlet, the crustal thickness appears to be  $\sim 30$  km, and the signal from the continental crustal is completely lost above 300 km of horizontal



distance.

Next we discuss the results for line B-C, which follows the NS trend of the MOOS stations. It is similar to the southern part of [Kim et al. \(2014\)](#) and our GRT migration up to 250 km of horizontal distance. It stops at the transition with the BEAAR array that has a different strike angle. Here, the slab top and oceanic Moho are seen dipping under the Kenai Peninsula and towards the Denali region, starting at a  $8^\circ$  dip angle and going up to  $16^\circ$ . The continental Moho appears discontinuously at the resolution limit (20 km depth) in the left and central part of the image. It slowly dips landwards at a  $5^\circ$  angle up to 280 km of horizontal distance where the dip increases to  $18^\circ$ .

The following transect, from points C to D, shows an along-strike migration profile computed using data mainly from the stations in the BEAAR array. The slab seems to have a 5 km jump in depth towards the SW end (point C) of the transect, where the migration line joins line B-C. The apparent dip of the slab from that viewing angle is  $17^\circ$ , and the thickness of the subducted crust is  $\sim 25$  km. The continental Moho is also visible at a relatively constant depth of 40 km.

The last transect, from points D to E, extends over the deepest part of the subducting slab in central Alaska. It is similar to [Rondenay et al. \(2010\)](#), as well as the northern part of [Kim et al. \(2014\)](#) and our GRT image at horizontal distances  $>320$  km, although the strike is slightly different. Starting from the left side of the profile, the dipping slab top and oceanic Moho are identified between 90-120 km and 115-135 km depth, respectively. This gives a subducted crustal thickness of 15 km, which is lower than what is interpreted in the previous section. The depth of the continental Moho is inferred to vary between 35 and 50 km depth, with the deepest parts towards the northern edge of the Denali mountain range.

## 5 Discussion

### 5.1 Resolution, penetration and observation limits

The shallowest depths depicting coherent structures are about 15 km for the GRT and 20 km for the 3D Kirchhoff. The deepest coherent structure is the Pacific subducted Moho at  $\sim 170$  km depth in the Kirchhoff migration under the SALMON array. The GRT does not show any coherent structure deeper than 140 km in both images. The depths and shapes for the continental Moho are similar in both images to about 5 km variation. The continental Moho below BEAAR is as deep as 50 km on both images and follows the trend of the subduction towards the trench under MOOS. The main difference between

the two methods is in the Cook inlet region, where the results from the GRT show a 40 km thick crust while the 3D Kirchhoff a 30 km thick crust.

A change in thickness and dip angle of the subducting slab can be observed across some sections. In the western part of the study area (SALMON data), the change in dip angle seems to be gradual. In the eastern part of the study area, the changes are more abrupt. In the GRT, there is a transition from a  $\sim 10$  km thick crust with an  $8^\circ$  dip angle to a  $\sim 20$  km thick crust with a  $29^\circ$  dip angle when the subducting Moho is at 60 km depth (figure 5b & 5d). In the 3D Kirchhoff, there is a jump in the subducting Moho near point C, when the subducting Moho is at 80 km depth (figure 6). However, the change in dip angle seems to be more gradual in the 3D Kirchhoff migration compared to the GRT.

Another important issue in subduction zones is the role of water in the system. One observation that can be made when looking for hydrated mantle material is overlying Moho absence or inversion. There are no clear signs for it in the GRT and in the Kirchhoff. The only place where a hole can be seen it in the Kirchhoff also shows a hole in the slab top, so this hole is more likely due to the 2D nature of the array above this region.

## 5.2 Western limit of the Yakutat Terrane

Rondenay et al. (2010) showed that there is probably a thick and buoyant subducting crust under the Denali Volcanic Gap. The absence of volcanism could be linked to the nature of the crust, which subducts at a very shallow angle close to the trench due to its buoyancy. This shallow subduction alters the thermal state of the source region for magmas by cooling the mantle wedge, which is then too cool to reach partial melting conditions when the subduction fluids reach it. To better assess the importance of this process, one needs to know the extent at depth of the Yakutat terrane, which is, at present, poorly constrained. We discuss our results for the mapping of the subducting and overriding crusts' properties in the volcanic gap region to help define the potential lateral extent of the Yakutat lower crust.

Our GRT image through line 3-4 and our Kirchhoff image around point C show abrupt changes in the LVL dip angle and thickness. Previously, those changes have been attributed to the blueschist-to-eclogite metamorphism in the Yakutat crust (Kim et al., 2014). The whole imaged LVL was interpreted as lower crust from the Yakutat terrane, and the depth at which those changes are observed is coherent with the onset of eclogitization in subduction zones (Van Keken et al., 2012). However, this mineralogic reaction alone cannot explain the magnitude of the change in thickness associated with the change in dip angles.

This inflexion and thickening highlights the transition between a more or less flat subduction of the thin unperturbed Pacific lithosphere and the steeper part where the Yakutat terrane is being underthrust and subducted. Moreover, our images do not show signals associated with the Yakutat terrane in the region covered by the SALMON array, which is compatible with previous observations (Eberhart-Phillips et al., 2006). This disagrees with results from Kim et al. (2014). In this paper, the authors showed that there is seismic signal in the EW aligned stations of the MOOS array, which they associated with the western border of the Yakutat Terrane. However, this low velocity signal is located below the moho from the Pacific slab, as inferred in our images in the region where MOOS and SALMON overlap. This interpretation is therefore not compatible with an oceanic plateau origin for the subducted part of the Yakutat. The change in crustal thickness observed both in the GRT and Kirchhoff images happens between stations KASH (61.86N, -150.08E) from the MOOS array to the south and WOLF (62.56N, -150.20E) from the BEAAR array to the north. Therefore we interpret the western limit of the Yakutat terrane to be between those stations. This implies that the Yakutat would be almost absent at depth below the Kenai Peninsula.

### 5.3 Intra-slab seismicity

The seismicity envelope has a steeper dip than the slab in the western part of the study area (Pacific slab, SALMON data). This phenomenon has been observed previously in other subduction regions (see e.g., Van Keken et al. (2012); Abers et al. (2013)). In our case, the seismicity envelope follows the trend of the imaged slab nicely down to 90 km. Below that depth, the two features start diverging, with the dip angle of the seismicity envelope becoming 5° steeper than the slab. These observations along the Pacific subduction confirm results obtained previously for subduction zones globally (Abers et al., 2013).

In the north eastern part of the study area, the seismicity extends slightly above the interpreted slab top in the shallower parts (figure 6b, line B-C), and is constrained to the subducting slab below 60 km. This is also the depth at which the slab is thicker, which is interpreted as the Yakutat lower crust in both migrations. However, there is no clear evidence of the seismicity envelope dipping significantly steeper than the slab in this region.

The departure between the seismicity and the slab as imaged our RF study can have two origins. Geologically, it has been linked to metastable eclogitization, in which case the seismicity envelope highlights the dehydration front along the subducting slab (Van Keken et al., 2012). However, here it could also be partially explained by the discrepancy in the

models used for the location of the earthquakes and the migration of the teleseismic data (see table 1). We plan on exploring this issue in a further study.

Finally, there is a discrepancy with Slab2 in the SALMON data, mostly visible on the Kirchhoff migration. This might be due to overmigration of the interface and the influence of the faster velocity in this region compared to the real 3D velocities. We plan on testing this in the future along with robust relocation of seismicity to confirm the results obtained here.

## 6 Conclusion

In this study, temporary data from 3 arrays deployed in Alaska over the past 20 years has been used to image the southern Alaska subduction system. The results that use data from the two older experiments (BEAAR and MOOS, see e.g. [Kim et al. \(2014\)](#)) are similar to previously published images. The new images below SALMON provide new constraints on a region that had previously not been imaged with high resolution method, providing important new insights into structures that were not well resolved until now, such as the western limit of the Yakutat terrane.

The combination of 2D GRT and 3D Kirchhoff provides complementary information about the scattering structure in the region ([Bostock and Rondenay, 1999](#); [Millet et al., 2019](#)). While the 2D GRT imaging method allows for fast and high density imaging, the 3D Kirchhoff can image the subduction interfaces at oblique angles along the original station distribution. Our observations led to the conclusion that the transition from the Pacific crust to the Yakutat terrane happens more to the north-east than previously thought ([Kim et al., 2014](#)). This transition is marked by an abrupt change in crustal thickness of both the GRT and Kirchhoff migration at a depth of 60 to 80 km in our transects 3-4 (2D GRT, figure 5) and B-D (3D Kirchhoff, figure 6).

The subducted Pacific plate is observed down to 170 km to the north west of the Cook inlet, which is to our knowledge the deepest trace of a subducted slab in RF imaging. Along this imaging line, under the SALMON array, there is a departure at depth between the imaged subducting interfaces and the seismicity envelope, which is linked to the progressive eclogitization of the crust ([Van Keken et al., 2012](#)). There is no clear evidence for this phenomenon under the Denali Volcanic Gap where the Yakutat terrane subducts under Alaska.

To conclude, we point to some open research questions regarding our imaging method and the study area. First, the influence of a 3D smooth regional velocity model on the migration needs to be further investigated. This is especially important for precise relative

location of the local seismicity compared to the subducting interfaces. Second, adding stations from permanent networks, especially between points A and C, would help to map the slab interface more precisely at the transition between the regular thin Pacific crust and the Yakutat terrane and lower crust along its whole NS extent. The 3D Kirchhoff migration will bring new clues to this issue, which is crucial in understanding how the seismic and volcanic system works around the Denali Volcanic Gap.

# Supporting Information for "A new look at the Southern Alaska Subduction Zone using 2D and 3D Migration of Receiver Functions"

## **Contents of this file**

1. Figures S1 to S2

## **Introduction**

The supplementary information presents the single scattering-mode images for the GRT and the Kirchhoff migration.

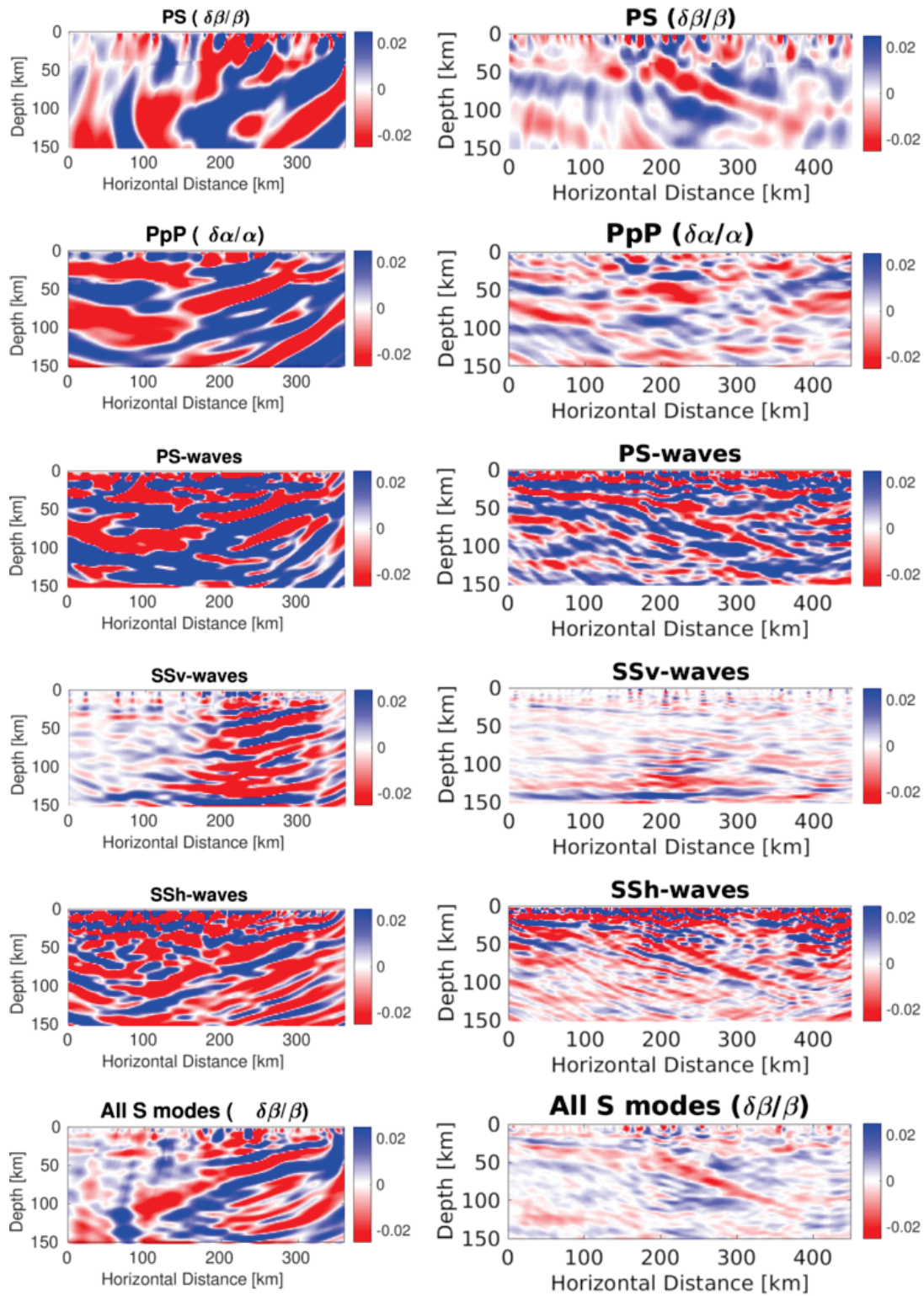


Figure S1 – Single scattering-mode and linear stack images for the GRT migration.

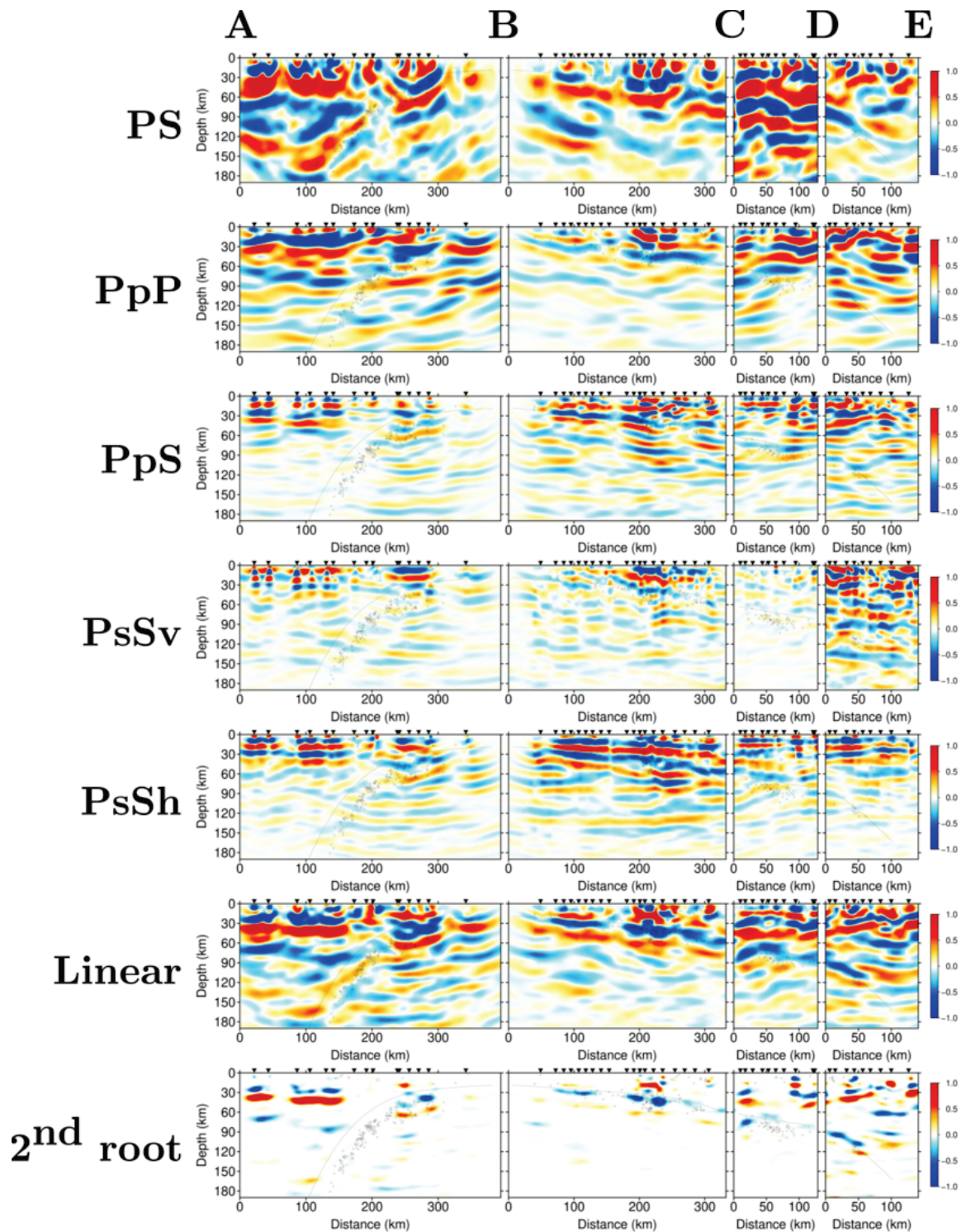


Figure S2 – Single scattering-mode, linear and 2<sup>nd</sup> root stack images for the Kirchhoff migration.





# Bibliography

- Abers, G. and Christensen, D. (2006). Multidisciplinary observations of subduction. *International Federation of Digital Seismograph Networks, Dataset/Seismic Network*.
- Abers, G. A., Nakajima, J., van Keken, P. E., Kita, S., and Hacker, B. R. (2013). Thermal-petrological controls on the location of earthquakes within subducting plates. *Earth and Planetary Science Letters*, 369:178–187.
- Beylkin, G. and Burridge, R. (1990). Linearized inverse scattering problems in acoustics and elasticity. *Wave motion*, 12(1):15–52.
- Bostock, M. and Rondenay, S. (1999). Migration of scattered teleseismic body waves. *Geophysical journal international*, 137(3):732–746.
- Bostock, M., Rondenay, S., and Shragge, J. (2001). Multiparameter two-dimensional inversion of scattered teleseismic body waves 1. Theory for oblique incidence. *Journal of Geophysical Research: Solid Earth*, 106(B12):30771–30782.
- Brocher, T. M., Fuis, G. S., Fisher, M. A., Plafker, G., Moses, M. J., Taber, J. J., and Christensen, N. I. (1994). Mapping the megathrust beneath the northern Gulf of Alaska using wide-angle seismic data. *Journal of Geophysical Research: Solid Earth*, 99(B6):11663–11685.
- Cheng, C., Bodin, T., and Allen, R. M. (2016). Three-dimensional pre-stack depth migration of receiver functions with the fast marching method: a Kirchhoff approach. *Geophysical Journal International*, 205(2):819–829.
- Christensen, D., Hansen, R., and Abers, G. (1999). Broadband experiment across the Alaska range. *International Federation of Digital Seismograph Networks, Dataset/Seismic Network*.
- Chuang, L., Bostock, M., Wech, A., and Plourde, A. (2017). Plateau subduction, intraslab seismicity, and the Denali (Alaska) volcanic gap. *Geology*, 45(7):647–650.
- de Kool, M., Rawlinson, N., and Sambridge, M. (2006). A practical grid-based method for

- tracking multiple refraction and reflection phases in three-dimensional heterogeneous media. *Geophysical Journal International*, 167(1):253–270.
- Eberhart-Phillips, D., Christensen, D. H., Brocher, T. M., Hansen, R., Ruppert, N. A., Haeussler, P. J., and Abers, G. A. (2006). Imaging the transition from Aleutian subduction to Yakutat collision in central Alaska, with local earthquakes and active source data. *Journal of Geophysical Research: Solid Earth*, 111(B11).
- Farra, V. and Vinnik, L. (2000). Upper mantle stratification by P and S receiver functions. *Geophysical Journal International*, 141(3):699–712.
- Ferris, A., Abers, G. A., Christensen, D. H., and Veenstra, E. (2003). High resolution image of the subducted pacific (?) plate beneath central alaska, 50–150 km depth. *Earth and Planetary Science Letters*, 214(3-4):575–588.
- Hagedoorn, J. (1954). A process of seismic reflection interpretation. *Geophysical Prospecting*, 2(2):85–127.
- Hayes, G. P., Moore, G. L., Portner, D. E., Hearne, M., Flamme, H., Furtney, M., and Smoczyk, G. M. (2018). Slab2, a comprehensive subduction zone geometry model. *Science*, 362(6410):58–61.
- Ichinose, G., Somerville, P., Thio, H. K., Graves, R., and O’Connell, D. (2007). Rupture process of the 1964 Prince William Sound, Alaska, earthquake from the combined inversion of seismic, tsunami, and geodetic data. *Journal of Geophysical Research: Solid Earth*, 112(B7).
- Kim, Y., Abers, G. A., Li, J., Christensen, D., Calkins, J., and Rondenay, S. (2014). Alaska megathrust 2: Imaging the megathrust zone and Yakutat/Pacific plate interface in the Alaska subduction zone. *Journal of Geophysical Research: Solid Earth*, 119(3):1924–1941.
- Li, J., Abers, G. A., Kim, Y., and Christensen, D. (2013). Alaska megathrust 1: Seismicity 43 years after the great 1964 Alaska megathrust earthquake. *Journal of Geophysical Research: Solid Earth*, 118(9):4861–4871.
- Li, S., Freymueller, J., and McCaffrey, R. (2016). Slow slip events and time-dependent variations in locking beneath Lower Cook Inlet of the Alaska-Aleutian subduction zone. *Journal of Geophysical Research: Solid Earth*, 121(2):1060–1079.
- Ligorria, J. and Ammon, C. (1999). Iterative deconvolution and receiver-function estimation. *Bulletin of the seismological Society of America*, 89(5):1395–1400.
- Liu, C., Lay, T., Xie, Z., and Xiong, X. (2019). Intraslab deformation in the 30 november 2018 Anchorage, Alaska, Mw 7.1 earthquake. *Geophysical Research Letters*, 46(5):2449–2457.

- Martin-Short, R., Allen, R., Bastow, I., Porritt, R., and Miller, M. (2018). Seismic imaging of the Alaska subduction zone: Implications for slab geometry and volcanism. *Geochemistry, Geophysics, Geosystems*, 19(11):4541–4560.
- Millet, F., Bodin, T., and Rondenay, S. (2019). Multimode 3-D Kirchhoff migration of receiver function at continental scale. *Journal of Geophysical Research*, pages –.
- Nokleberg, W., Parfenov, L., Monger, J., Norton, I., Khanchuk, A., Stone, D., Scotese, C., Scholl, D., and Fujita, K. (2000). Phanerozoic tectonic evolution of the circum-north pacific. *US Geol. Surv. Prof. Paper*, page 122.
- Rondenay, S. (2009). Upper mantle imaging with array recordings of converted and scattered teleseismic waves. *Surveys in geophysics*, 30(4-5):377–405.
- Rondenay, S., Bostock, M., and Fischer, K. (2005). Multichannel inversion of scattered teleseismic body waves: practical considerations and applicability. *Geophysical monograph-american geophysical union*, 157:187.
- Rondenay, S., Montesi, L. G., and Abers, G. A. (2010). New geophysical insight into the origin of the Denali volcanic gap. *Geophysical Journal International*, 182(2):613–630.
- Rondenay, S., Spieker, K., Sawade, L., Halpaap, F., and Farestveit, M. (2016). GLImER: A new global database of teleseismic receiver functions for imaging Earth structure. *Seismological Research Letters*, 88(1):39–48.
- Tape, C., Christensen, D., Moore-Driskell, M. M., Sweet, J., and Smith, K. (2017). Southern Alaska lithosphere and mantle observation network (SALMON): A seismic experiment covering the active arc by road, boat, plane, and helicopter. *Seismological Research Letters*, 88(4):1185–1202.
- Tape, C., Christensen, D. H., and Moore-Driskell, M. M. (2015). Southern alaska lithosphere and mantle observation network. *International Federation of Digital Seismograph Networks, Dataset/Seismic Network*.
- Van Keken, P., Kita, S., and Nakajima, J. (2012). Thermal structure and intermediate-depth seismicity in the Tohoku-Hokkaido subduction zones. *Solid Earth*, 3(2):355–364.
- Wang, Y. and Tape, C. (2014). Seismic velocity structure and anisotropy of the Alaska subduction zone based on surface wave tomography. *Journal of Geophysical Research: Solid Earth*, 119(12):8845–8865.
- Wu, R. and Aki, K. (1985). Scattering characteristics of elastic waves by an elastic heterogeneity. *Geophysics*, 50(4):582–595.



# Concluding remarks and scientific outlook

## 1 Conclusions

### 1.1 Writing the migration algorithm

During my PhD, my main focus was to develop the migration algorithm. I decided to achieve this using the fortran 90 programming language. This was motivated by a few facts. First, it is the language I was most familiar with prior to my PhD, and therefore the one I felt most confident with to develop the code as fast as possible. Second, it is the same language in which the FMM code is written, so learning more regarding one code would help me understand the other as well (de Kool et al., 2006). Finally, and maybe most importantly, it is very efficient regarding memory allocation, array handling, input/output, and of course raw computing speeds.

I also used bash and GMT extensively for automation and plotting purposes (Wessel and Luis, 2017). During my PhD I also learned about parallel programming, even if it is not yet implemented in the migration algorithm. This is one of the avenues of research that are still open in the development component of this thesis.

### 1.2 Processing the seismic data

In order to apply the code I developed to field data, I learned how to download data from a global database (IRIS, [ds.iris.edu/ds/node/dmc](https://ds.iris.edu/ds/node/dmc)) and process them. To do this, I adapted codes in Matlab and python, mainly originating from the GLImER project, but also from the ObsPy library (Rondenay et al., 2016; Wassermann et al., 2013). The array of methods that I learned here are numerous, including but not limited to working with seismic analysis code (SAC, Helffrich et al. (2013)) files, applying instrument response

removal to the raw waveforms, various types of filterings and polarization analysis and the deconvolution said waveforms to obtain the receiver functions. Regarding the RFs more specifically, I adapted the pre-processing developed by Rondenay for the GRT migration to the needs of the Kirchhoff algorithm. The two methods share the same base, but the 2D vs. 3D difference, as well as the inversion issue, make it so that the processing needed to be retuned.

### 1.3 First geological applications

Geological applications of the novel 3D Kirchhoff imaging principle and comparison with results from a standard 2D GRT migration were performed in Greece and Alaska. The application of Kirchhoff migration to data in Greece was the first geological application of the new migration algorithm (Millet et al., 2019). While exploiting and analyzing the data and images, I was able to talk with numerous people in Bergen and Lyon about both the seismological and geological implications of the results of the study. This application was mainly to showcase the method, but provided a good introduction to data processing and geological discussion of seismological results.

The second application of the new imaging principle is on the data from Southern Alaska. For this project, I followed all the steps from downloading the raw data to providing the first images of scattering potential under the SALMON array, including all the data and image processing. I presented the preliminary results at AGU and met with other people involved in the SALMON project who were very motivated to further discuss the results in terms of geodynamics.

### 1.4 Side projects

In collaboration with the scientific team at UiB, I helped deploy two seismometers for the Bergen Arcs Seismic Experiment (BASE). This experiment aims at better understanding the seismic structure of the deep Bergen basement, as well as the Hardanger shear zone. It is comprised of two parallel station lines, which makes this array ideal for GRT and Kirchhoff imaging. Together with Felix Halpaap, we also deployed two seismometers in the direct vicinity of the Mannen mountain in Møre og Romsdal county, Norway, which has been subject to small rockfalls and large slope shifts in the past decades. This deployment followed a period of high risk on this unstable mountain slope, in the hope to record useful seismic information to help study large mountain rockslide.

During my second PhD year, while studying in Lyon, I helped develop tools for remote sensing with fellow PhD students working on Mars. These tools help characterize light

reflection based observations from Martian orbit to investigate the mineralogy of the first few centimeters of Martian soil.

Using the skills I learned during my PhD, I helped develop a waveform based characterisation method for slab earthquakes in subduction zone (Halpaap et al., 2019). Using precise travel time computation for scattered phases from local earthquakes using FMM, this method aims at determining on which side of a given interface an earthquake occurs (slab top or slab Moho for example). This approach has the potential to reduce hypocenter location uncertainties for intermediate to deep earthquakes by an order of magnitude, down to the order of 100 meters, compared to classical location and relocation techniques. It works by comparing the high frequency data recorded on local monitoring arrays to synthetic synthetic arrival times computed in a 3D model of the region that includes sharp interfaces. Characteristic phases for events on either side of those interfaces have the potential to discriminate the exact location of the recorded earthquakes.

## 1.5 Conferences, abstracts and publications

Finally, I presented my research in local (CDD OSU in Lyon, 2016 and 2017), national (DEEP in Norway, 2017 to 2019) and international conferences (IASPEI in Kobe in 2017 (Millet et al., 2017b), AGU in New-Orleans in 2017 (Millet et al., 2017a) and Washington DC in 2018 (Millet et al., 2018)) through oral or poster presentations, and won an award for best poster at the second General Assembly of the DEEP research school. I published an article in a peer reviewed journal describing the method extensively and application to a first dataset (Greece, chapter 2, Millet et al. (2019)) and wrote a second article focussing on the data processing and an application to a second dataset (Alaska), ready to be published. Finally I am co-author on a paper that focuses on the waveform based slab earthquake location (Halpaap et al., 2019).

## 2 Scientific outlooks

### 2.1 New geological objectives

In this thesis, the main geologic interest was subduction zone imaging. However, there are other regions that would make for interesting applications for the method that we developed. Complex 3D crustal and lithospheric structures would greatly benefit from precise 3D scattering imaging. We believe that the method that we developed here would fit nicely into such studies. Among the most interesting regions to image would be the



complex interactions between the Pacific and Philippine slabs beneath Japan.

Another type of structure that could be tackled with this method is large orogenic complexes, such as the Alps or the Himalayan mountain range. Experiments such as AlpArray would be interesting application cases for the 3D Kirchhoff migration (AASN, 2015).

Finally, fully 3D migration could be used for imaging of deeper structures, such as the mantle transition zone for example. In this region of the globe, the topography is usually relatively flat, which makes CCP imaging useful. Partially 3D GRT has been applied to the transition zone with large volumes of USArray data, and helped resolve topography for the 410 and 660 discontinuities (Wang and Pavlis, 2016). A fully 3D method could confirm these results and shed new light on the topic.

## 2.2 Optimizing the numerical algorithm

Regarding further practical developments for the migration algorithm, we see two main avenues for future research. The first one is parallelizing the numerical code. Parallelizing the algorithm would allow for easy handling of large databases, such as dense continental scale deployments like USArray. Because individual migrations are independent from another, this should not be a problem to implement, but care needs to be taken regarding the non linear stacking methods.

The second avenue of research is to adapt the code for deeper imaging. This would require decoupling the computation box from the surface. This needs to be handled both in the FMM calculations as well as in the migration algorithm. Being able to define a computation box that is not directly linked to the surface of the Earth would allow for fast 3D pre-stack migration in virtually any region inside the Earth.

## 2.3 Adapting the code for new data types

In this thesis, the only type of data used for migration was P receiver functions, but the method can be extended to account for other types of scattering data. One such data type is autocorrelation of continuous wavefield recordings, which can be used to transform the transmission response of a medium into a reflectivity response, from which velocity structure can be inferred (Claerbout, 1985). The geometry of the reflectivity response obtained through autocorrelation of teleseismic waves corresponds to the geometry of the PpP free surface multiple, so it should be readily usable in the current migration algorithm. Autocorrelations have proven to be a useful tool to obtain structural information about

the Earth, and would be a great addition to the PpP signal in the RFs (see, e.g., [Saygin et al., 2017](#)).

As discussed in chapter 2, the migration algorithm and scattering pattern computations could be adapted for S receiver function studies ([Farra and Vinnik, 2000](#)). S receiver functions have been used with many standard imaging procedures, and should provide complementary imaged to the P receiver functions with the 3D Kirchhoff as well. This time, the FMM computations would have to be adapted for the incident S wavefield, but the computations for the scattered P and S wavefields would remain the same.



# Bibliography

- AASN (2015). AlpArray seismic network (AASN) temporary component. *AlpArray Working Group, Other/Seismic Network*, 10.
- Claerbout, J. F. (1985). *Imaging the Earth's Interior*.
- de Kool, M., Rawlinson, N., and Sambridge, M. (2006). A practical grid-based method for tracking multiple refraction and reflection phases in three-dimensional heterogeneous media. *Geophysical Journal International*, 167(1):253–270.
- Farra, V. and Vinnik, L. (2000). Upper mantle stratification by P and S receiver functions. *Geophysical Journal International*, 141(3):699–712.
- Halpaap, F., Rondenay, S., Liu, Q., and Millet, F. (2019). Toward waveform-based characterization of slab earthquakes. *PhD. Thesis*.
- Helffrich, G., Wookey, J., and Bastow, I. (2013). *The seismic analysis code: A primer and user's guide*. Cambridge University Press.
- Millet, F., Bodin, T., and Rondenay, S. (2017a). Multi-mode 3D Kirchhoff migration of receiver functions at continental scale with applications to USArray. In *AGU Fall Meeting Abstracts*.
- Millet, F., Bodin, T., and Rondenay, S. (2017b). Towards 3D Kirchhoff migration of receiver functions at continental scale. In *Joint Scientific Assembly of the IAG and IASPEI*.
- Millet, F., Bodin, T., and Rondenay, S. (2019). Multimode 3-D Kirchhoff migration of receiver function at continental scale. *Journal of Geophysical Research*, pages –.
- Millet, F., Bodin, T., Rondenay, S., and Tape, C. (2018). Multi-mode 3D Kirchhoff migration of receiver functions in Southern Alaska using permanent and temporary array data. In *AGU Fall Meeting Abstracts*.
- Rondenay, S., Spieker, K., Sawade, L., Halpaap, F., and Farestveit, M. (2016). GLImER:

A new global database of teleseismic receiver functions for imaging Earth structure. *Seismological Research Letters*, 88(1):39–48.

Saygin, E., Cummins, P. R., and Lumley, D. (2017). Retrieval of the P wave reflectivity response from autocorrelation of seismic noise: Jakarta Basin, Indonesia. *Geophysical Research Letters*, 44(2):792–799.

Wang, Y. and Pavlis, G. L. (2016). Roughness of the mantle transition zone discontinuities revealed by high-resolution wavefield imaging. *Journal of Geophysical Research*, 121:6757–6778.

Wassermann, J., Krischer, L., Megies, T., Barsch, R., and Beyreuther, M. (2013). Obspy: A python toolbox for seismology. In *AGU Fall Meeting Abstracts*.

Wessel, P. and Luis, J. F. (2017). The GMT/MATLAB toolbox. *Geochemistry, Geophysics, Geosystems*, 18(2):811–823.